Launch Trajectory Control of a Flying Wing with Vertical Takeoff Capability for Airborne Wind Energy Systems

Trajektorienregelung der Startphase eines senkrechtstartfähigen Nurflüglers für Höhenwindenergieanlagen

Von der Fakultät für Maschinenwesen der
Rheinisch-Westfälischen Technischen Hochschule Aachen
zur Erlangung des akademischen Grades eines Doktors
der Ingenieurwissenschaften genehmigte Dissertation

vorgelegt von

Hendrik Fuest

Berichter:
Univ.-Prof. Dr.-Ing. Dieter Moormann
Prof. Dr.-Ing. Roland Schmehl

Tag der mündlichen Prüfung: 24. März 2025

Diese Dissertation ist auf den Internetseiten
der Universitätsbibliothek online verfügbar.

Vorwort

Die vorliegende Arbeit entstand im Rahmen meiner Tätigkeit als wissenschaftlicher Mitarbeiter am Institut für Flugsystemdynamik der RWTH Aachen University. Flugwindkraftwerke sind ein Nischenbereich innerhalb der erneuerbaren Energien und ihr endgültiger Durchbruch muss sich noch abzeichnen. Dies liegt unter anderem an der hohen Komplexität der Flugsteuerung, die insbesondere in der Startphase eine individuelle Flugbahn, Modellierung und Regelung erfordert. Diese Arbeit habe ich daher als besonders anspruchsvoll empfunden und hoffe, sowohl kurzfristig einen Beitrag zur Entwicklung komplexer Flugregelungsverfahren am Institut geleistet zu haben, als auch langfristig die Weiterentwicklung von Flugwindkraftwerken unterstützen zu können.

Mein besonderer Dank gilt Herrn Prof. Dr.-Ing. Dieter Moormann, der mit seiner fachlichen Expertise meine Arbeit enorm bereichert hat und durch seine sympathische Art zu einem angenehmen Klima auch außerhalb der Arbeit beigetragen hat. Zudem möchte ich mich bei Herrn Prof. Dr.-Ing. Roland Schmehl für die Übernahme des Korreferates, sowie bei Herrn Prof. Dr. sc. Dominik Johannes Krug für den Prüfungsvorsitz bedanken.

Mein Dank gilt des Weiteren allen Kollegen und Kolleginnen des Instituts und der Nachbarinstitute, mit denen ich die fachlich kritischen und persönlichen Gespräche sehr geschätzt habe. Dabei möchte ich mich im Speziellen bei Dominik F. Duda bedanken, der mich auf dem gesamten Weg der Promotion mit vielen Höhen und Tiefen begleitet hat. Zudem hat mir die Teamarbeit mit allen aus der IT-Verwaltung, dem Elektrolabor, den Studierenden und dem Sekretariat viel Freude bereitet. Ich danke allen für die gemeinsame Zeit.

Schließlich möchte ich mich bei meiner gesamten Familie und meinen engen Studienfreunden bedanken, die mich auf meinem Lebensweg und der Universitätszeit durchgängig motiviert haben. Insbesondere bei Florian Frantzen, der mir stets mit seiner schnellen Auffassungsgabe und dem emotionalen Beistand eine große Unterstützung bei der Promotion war. Die Arbeit widme ich meinem Neffen Finn, der passend zur Fertigstellung das Licht der Welt erblickt hat.

Aachen, März 2025 Hendrik Fuest

Abstract

Airborne wind energy (AWE) is an emerging technology that harnesses wind power using tethered flight systems. Maximum power output is sought out for operations ranging from low to high wind velocities. A flying wing is a promising airborne wind energy flight system since it is reduced to the wing as the primary lift-generating component to achieve a highly efficient, aerodynamic flight. For takeoff within a limited space, the flying wing is capable of vertical takeoff in a tailsitter configuration.

This thesis presents a trajectory controller that controls the aerodynamic velocity of the flying wing from vertical hover to horizontal forward flight while maintaining a constant height. This flight trajectory marks the beginning of the launching phase of the airborne wind energy system, which places high demands on the flight controller for low power consumption and particularly high wind robustness. The flight controller achieves a thrust-efficient launch trajectory with sufficient control reserves for operations including a dynamic wind field. It incorporates the specific constraints imposed by the tether connection and the limited flight envelope of the flight system. The stabilization of the natural instabilities of the flight system's attitude is a necessary criterion that is inherently integrated into the control architecture.

A straight flight path along the wind vector with a yaw-roll motion is outlined as a solution to keep the flight system within controllable limits. Based on a detailed analysis of trim states, the operating points from vertical takeoff to horizontal forward flight are carefully selected under consideration of control reserves and thrust requirements. The focus is on the velocity controller, which employs LQR control and integrates all flight axes to explicitly control the velocities along this selected flight path of commanded operating points. The launch trajectory controller enables dynamic operation and adapts the orientation of the flight system to a rotating wind vector to maintain flight within the flight envelope. The trajectory controller is thoroughly validated using nonlinear simulation results. Accurate disturbance rejection in response to a rotating wind field is in particular decisive during the initial hover flight phase. Simulation and flight test results demonstrate the effectiveness of the flight trajectory controller during this flight phase under wind conditions, which is complemented by a robustness analysis to verify stable flight.

Kurzfassung

Airborne Wind Energy (AWE) bezeichnet eine Technologie der sogenannten Flugwindkraftwerke, bei der Windenergie durch seilgebundene Flugsysteme nutzbar gemacht wird. Angestrebt wird eine maximale Leistungsausbeute für den Betrieb sowohl bei niedrigen als auch hohen Windgeschwindigkeiten. Ein Nurflügler stellt dabei ein vielversprechendes Flugsystem für einen hocheffizienten Betrieb dar, da er auf den Flügel als primäre Auftriebskomponente reduziert ist. In der sogenannten Tailsitter Konfiguration ist er zudem in der Lage, auch auf begrenztem Raum senkrecht starten zu können.

In dieser Arbeit wird eine Trajektorienregelung entwickelt, die die aerodynamische Geschwindigkeit des Nurflüglers vom vertikalen Schwebeflug bis in den horizontalen Vorwärtsflug unter Beibehaltung einer konstanten Höhe regelt. Diese Flugtrajektorie stellt den Beginn der Startphase des Flugwindkraftwerks dar, in der hohe Anforderungen bezüglich eines geringen Leistungsbedarfs und vor allem an eine hohe Windrobustheit gestellt werden. Der Flugregler realisiert eine Startphase mit geringem Schubbedarf und ausreichenden Steuerreserven für den Betrieb in einem dynamischen Windfeld. Dabei werden zudem die spezifischen Randbedingungen der Seilverbindung und der begrenzte Trimmbereich des Flugsystems berücksichtigt. Die Lagestabilisierung der natürlichen Instabilitäten des Flugsystems stellt ein notwendiges Kriterium dar, welches inhärent in die Regelungsarchitektur integriert ist.

Um das Flugsystem innerhalb seiner steuerbaren Grenzen zu halten, wird eine gerade Flugbahn entlang des Windvektors mittels einer Gier-Roll-Bewegung herausgearbeitet. Basierend auf einer detaillierten Analyse von Trimmzuständen werden die Betriebspunkte vom Senkrechtstart bis zum horizontalen Vorwärtsflug unter Berücksichtigung der Steuerreserven und des Schubbedarfs definiert. Der Fokus der Arbeit liegt auf dem Geschwindigkeitsregler, der mittels einer LQR-Regelung alle Flugachsen integriert, um die Geschwindigkeiten entlang dieser ausgewählten Betriebspunkte umzusetzen. Die Trajektorienregelung ermöglicht einen dynamischen Betrieb und passt die Kursrichtung der Flugbahn an einen rotierenden Windvektor an, um den Flug innerhalb des Trimmbereichs zu gewährleisten. Die Trajektorienregelung wird anhand einer nichtlinearen Simulation validiert. Eine gute Störunterdrückung als Reaktion auf ein rotierendes Windfeld ist insbesondere in der Schwebeflugphase entscheidend. Simulations- und Flugversuchsergebnisse zeigen daher die Wirksamkeit der Trajektorienregelung während dieser Flugphase unter Windbedingungen, ergänzt durch eine Robustheitsanalyse zum Stabilitätsnachweis.

Contents

List of Symbols **xi**

1. Introduction **1**
1.1. Airborne Wind Energy . . . 2
1.1.1. Flight System . . . 5
1.1.2. Launching Phase - State-of-the-Art . . . 7
1.2. Objective and Structure of Work . . . 9

2. Flight Mechanics and Model of the AWE System **11**
2.1. Coordinate Systems and Transformations . . . 11
2.1.1. Euler and Aerodynamic Angles . . . 12
2.1.2. Quaternions . . . 13
2.2. Trim Condition . . . 15
2.3. Attitude Stability . . . 16
2.3.1. Longitudinal Stability . . . 17
2.3.2. Lateral Stability . . . 18
2.3.3. Directional Stability . . . 19
2.4. Model of the AWE System . . . 20
2.4.1. Model Structure . . . 20
2.4.2. Tether Model . . . 21
2.4.3. Aerodynamic Model including high Aerodynamic Angles . . . 24

3. Trajectory Concepts of Tailsitter Flight Systems **33**
3.1. Tailsitter - State-of-the-Art . . . 33
3.2. Longitudinal Motion of the AWE System . . . 35

4. Design of the Launch Trajectory Controller **40**
4.1. Design Objective . . . 40
4.2. Launching Concept . . . 44
4.3. Definition of the Operating Points . . . 48
4.3.1. Methodology of the Trim Calculations . . . 48
4.3.2. Identification of the Trim Path . . . 53

4.3.3. Linearization of the Trim Path 58
4.4. Control Concept 62
4.5. Controller Implementation 64
4.5.1. Implementation of the Velocity Controller 65
4.5.2. Implementation of the Supporting Control Cascades 68

5. Validation and Discussion **74**
5.1. Simulation and Flight Test Results 74
5.1.1. Yaw-Roll Transition 75
5.1.2. Wind Alignment in Prop-borne Flight 79
5.2. Robustness Analysis of the Wind Alignment 86
5.2.1. Simplified Model of the Pitch-Roll Motion 87
5.2.2. Uncertainty Estimation 91
5.2.3. Model Verification 93
5.2.4. Wind Analysis 99
5.3. Discussion 102

6. Conclusion and Outlook **107**

Bibliography **112**

Appendix **128**
A. Quaternion Calculations 128
B. AWE System Data and Verification 130
C. Flight Mechanics 131
D. LQR and Robustness Design 132

List of Symbols

Latin Symbols

A	Area	$[\mathrm{m}^2]$
A_{ss}	System matrix of a state-space system	$[-]$
B_{ss}	Input matrix of a state-space system	$[-]$
C	Constant	$[-]$
C_{ss}	Output matrix of a state-space system	$[-]$
C_D	Drag coefficient	$[-]$
C_L	Lift coefficient	$[-]$
C_m	Pitch moment coefficient	$[-]$
c_P	Power coefficient	$[-]$
D	Drag force	[N]
D_{ss}	Feedthrough matrix of a state-space system	$[-]$
d_{t}	Tether diameter	[m]
F_{t}	Tether force	[N]
f	Uniform thrust	[N]
Δf	Differential thrust to induce a yaw moment	[N]
$\{FM\}$	Forces and moments vector in the body-fixed coordinate system	$[-]$
G	Transfer function	$[-]$
g	Gravity	$[\mathrm{m/s}^2]$
I_x	Inertia in x-direction	$[\mathrm{kg\,m}^2]$
I_y	Inertia in y-direction	$[\mathrm{kg\,m}^2]$
J	Cost function	$[-]$
K^{DC}	Static gain of the transfer function	$[-]$
k_{t}	Tether length ratio	$[-]$
L	Roll moment	[N m]
L_{wing}	Lift force at the wing	[N]
l_μ	Mean aerodynamic chord	[m]
l_{c}	Chord length	[m]
l_p	Length of lever arm of roll damping	[m]
l_{t}	Stretched tether length	[m]

$l_{t,0}$	Unstretched tether length	[m]
M	Pitch moment	[N m]
M^{bg}	Transformation matrix between geodetic and body coordinate system	[−]
M_t	Tether stiffness	[N/m]
m	Mass	[kg]
N	Yaw moment	[N m]
n_t	Load factor of the ratio tether force to weight	[−]
n_f	Load factor of the thrust-to-weight ratio	[−]
P	Power	[W]
$P_{max,loyd}$	Maximum power concerning Loyd	[W]
p	Roll rate	[deg/s]
q	Pitch rate	[deg/s]
$\underline{q}$	Quaternion vector	[−]
q_i	i-component of the vector part of a quaternion	[−]
q_j	j-component of the vector part of a quaternion	[−]
q_k	k-component of the vector part of a quaternion	[−]
q_s	Scalar part of the quaternion	[−]
q_t	Tether line load	[N/m]
$\vec{q}_v$	Vector part of the quaternion	[−]
r	Yaw rate	[deg/s]
$\vec{s}$	Position vector $[x, y, z]^T$	[m]
s	Laplace variable	[−]
S	Wing area	[m^2]
S_s	Swept area of turbine blades	[m^2]
T	Thrust force	[N]
T_e	Time constant of the elevons	[s]
t	Time	[s]
t_q	Sample point for spherical interpolation of quaternions	[−]
$\vec{u}$	Input vector of a state-space system	[−]
u_i	i-component of the rotation axis of the vector part of a quaternion	[−]
u_j	j-component of the rotation axis of the vector part of a quaternion	[−]
u_k	k-component of the rotation axis of the vector part of a quaternion	[−]
$\vec{u}_q$	Rotation axis of the vector part of the quaternion	[−]
$\vec{u}_t$	Trim controls	[−]
u, v, w	x-, y-, z-component of the inertial velocity	[m/s]
$\vec{V}$	Flight velocity vector $[u, v, w]^T$	[m/s]

$\vec{V}_\mathrm{A}$	Aerodynamic velocity	[m/s]
$\vec{V}_\mathrm{G}$	Ground velocity	[m/s]
$\vec{V}_\mathrm{W}$	Wind velocity	[m/s]
$\vec{v}$	Eigenvector of the poles	[−]
W	Weight force	[N]
X	Force in x-direction	[N]
$\vec{x}$	State vector of a state-space system	[−]
$\vec{x}_\mathrm{t}$	Equilibrium trim state	[−]
x	x-Position	[m]
Y	Force in y-direction	[N]
$\vec{y}$	Output vector of a state-space system	[−]
y	y-Position	[m]
Z	Force in z-direction	[N]
z	z-Position	[m]

Greek Symbols

α	Angle of attack	[deg]
α_0	Zero angle of attack	[deg]
β	Slip angle	[deg]
ϵ	Tether angle	[deg]
κ	Uniform elevon deflection	[deg]
$\Delta\kappa$	Differential elevon deflection to induce a roll moment	[deg]
Θ	Pitch angle around the y-axis	[deg]
Θ_q	Rotation angle of the quaternion	[rad]
λ	Relative elevon depth to wing chord	[−]
λ	Eigenvalues of the poles	[rad/s]
λ_s	Eigenvalues of a state-space system	[rad/s]
ρ	Air density	[kg/m^3]
ρ_t	Tether density	[kg/m^3]
$\underline{\Phi}$	Attitude angles $[\Phi, \Theta, \Psi]^T$	[deg]
Φ	Roll angle around the x-axis	[deg]
Ψ	Yaw angle around the z-axis	[deg]
Ψ_e	Element definition angle around the z-axis	[deg]
Ψ_w	Wind direction	[deg]
Ω_q	Rotation angle between two quaternions	[rad]
ω	Angular rates $[p, q, r]^T$	[deg/s]

Indices and Special Characters

$\times$	Cross product
$\otimes$	Kronecker product
$\square^*$	Conjugate
$\|\|\square\|\|$	Norm
$\overline{\square}$	Average
$\dot{\square}$	Time derivative
$\delta\square$	Deviations
$\Delta\square$	Differential
$\partial\square$	Derivative
$\mathrm{d}\square$	Infinitesimal
$\frac{\mathrm{d}}{\mathrm{d}t}\square$	Time derivative
$\boldsymbol{J}$	Jacobi matrix
$\square^{\mathrm{b}}$	Body coordinate system
$\square_{\mathrm{b}}$	Body frame
$\square_{\mathrm{cmd}}$	Command
$\square_{\mathrm{dist}}$	Disturbance
$\square_{\mathrm{eq}}$	Equivalent
$\square^{\mathrm{ff}}$	Feedforward
$\square^{\mathrm{g}}$	Geodetic coordinate system
$\square_{\mathrm{g}}$	Geodetic frame
$\square^{\mathrm{OP}}$	Operating point
$\square_{\mathrm{ref}}$	Reference value
$\square_{\mathrm{slerp}}$	Spherical interpolated value
$\square^{\mathrm{t}}$	Tether coordinate system
$\square_{\mathrm{t}}$	Tether frame
$\square_{\mathrm{tp}}$	Trim value
$\square^{\top}$	Transposed vector
$\square^{\mathrm{w}}$	Wind coordinate system
$\square_{\mathrm{w}}$	Wind frame
$\square_{\mathrm{yzx}}$	Angle in rotation order 'YZX'
$\square_{\mathrm{zxy}}$	Angle in rotation order 'ZXY'
$\square_{\mathrm{zyx}}$	Angle in rotation order 'ZYX'
$\square_0$	Linearization point

Acronyms

AC	Aerodynamic center
act	Actual value
AWE	Airborne wind energy
CAGR	Compound annual growth rate
CBM	Component-based model
CFD	Computational fluid dynamics
cmd	Command
CoG	Center of gravity
Ctrl	Controller
CTT	Collective thrust transitioning
DTT	Differential thrust transitioning
fft	Fast fourier transform
FEM	Finite element method
FS	Flight state
INDI	Incremental nonlinear dynamic inversion
LCOE	Levelized cost of electricity
LERP	Linear interpolation
LQR	Linear-quadratic regulator
MPC	Model predictive control
MTT	Mono thrust transitioning
NDI	Nonlinear dynamic inversion
OP	Operating point
PID	Proportional-integral-derivative
RoA	Region of attraction
SLERP	Spherical linear interpolation
thresh	Threshold
UAV	Unmanned aerial vehicle
VTOL	Vertical takeoff and landing

1. Introduction

Unmanned flying wings are a type of unmanned aerial vehicle (UAV) that are controlled remotely or automatically without a human on board. With the recent developments in hardware and software, automated flights of UAVs have become feasible within a wide range of potential applications such as agriculture [1, 2], logistics [3], infrastructure [4], healthcare [5], and search and rescue [6], with expectations for further expansion expected in the future [7]. To address the diverse requirements across the various fields of application, different types of UAVs have been developed. While rotary wing systems generate lift with electric propulsion propellers for vertical takeoff and landing (VTOL) capability [8], fixed wings aerodynamically generate lift through their wings to increase efficiency for increased endurance and flight velocity, but do not cover VTOL capabilities [9]. To combine these advantages, various hybrid concepts have emerged. Dual systems add additional propulsion units for vertical and horizontal acceleration [10, 11, 12], while tilting concepts such as tilt-rotors [13, 14, 15] or tilt-wings [16, 17, 18, 19] allow the propulsion or aerodynamic devices to be rotated. However, additional propellers and tilt mechanisms contribute to dead weight during cruise and reduce the overall flight performance. Therefore, flying wings are investigated, which can take off vertically on their winglets in a so-called tailsitter configuration and rotate entirely during flight to generate aerodynamic lift through the wing. This configuration represents an additional, promising hybrid concept regarding flight efficiency and reduced structural components [20].

Airborne wind energy (AWE) is a technology to harvest wind energy with its fundamental principles and ideas first introduced by Miles L. Loyd in 1980 [21]. During the following years, research on the subject was largely abandoned due to the lack of suitable airborne devices for automatic operation. However, with the rise of the technology of UAVs, the airborne wind energy sector has experienced a rapid acceleration in the last two decades. Several companies and institutes have been working in this sector, resulting in a large number of prototypes, patents and research articles. At present, the technology is at a low-to-intermediate readiness level and has not yet achieved market-entry requirements in terms of reliability and economics. As such, there is still potential for improvement in various aspects of the system, such as technology, operation, structure, flight control, or power conversion. [22, 23, 24]

This thesis falls in line with the current research on AWE. It focuses on a flying wing in tailsitter configuration, which represents a promising flight system with a high power output for AWE applications, while providing VTOL capability for independent takeoff within a limited space. In this thesis, vertical, hover flight is defined as prop-borne flight, in which thrust is mainly responsible for balancing the weight of the system. As the flight system increases aerodynamic velocity, it eventually exceeds its stall speed and enters a horizontal, so-called wing-borne flight, where aerodynamic lift balances weight, and the thrust demand is reduced. Wing-borne and prop-borne are no discrete states but describe the limits of a continuous set of these flight states. The flight phase from zero to high velocities in wing-borne flight is defined as the transition, see Fig. 1.1. The flight envelope describes in this thesis the set of flight velocities as a function of the flight attitude and controls for which the flight system is trimmed.

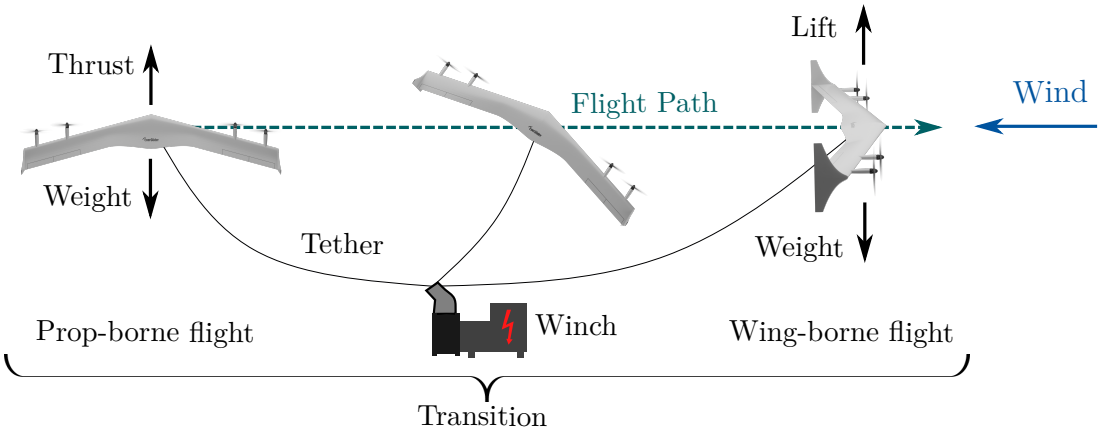


Figure 1.1.: Definition of the transition.

In particular, the transition of a flying wing with VTOL capability is highly complex and it requires an individual launch trajectory control for robust operation, which is designed in this thesis. In the following, AWE is explained in detail with a presentation of the specific flight system and details of the state-of-the-art launching phase, which encompasses the transition. This chapter concludes with the objectives and the structure of this thesis.

1.1. Airborne Wind Energy

With growing concerns about climate change and the finite nature of fossil fuel resources, the need for renewable energy sources has become increasingly apparent. At present, the main sources of global renewable electricity generation are solar energy, wind energy, hydropower, and bioenergy. Although only a small fraction of the sun's energy is naturally converted into wind energy through temperature and pressure gradients, this amount of

energy would theoretically be enough to cover today's power consumption worldwide ten times. However, in 2022, only 7.3 % of global electricity was generated by wind, yet trends are going upwards and new opportunities have to be exploited. [25, 26]

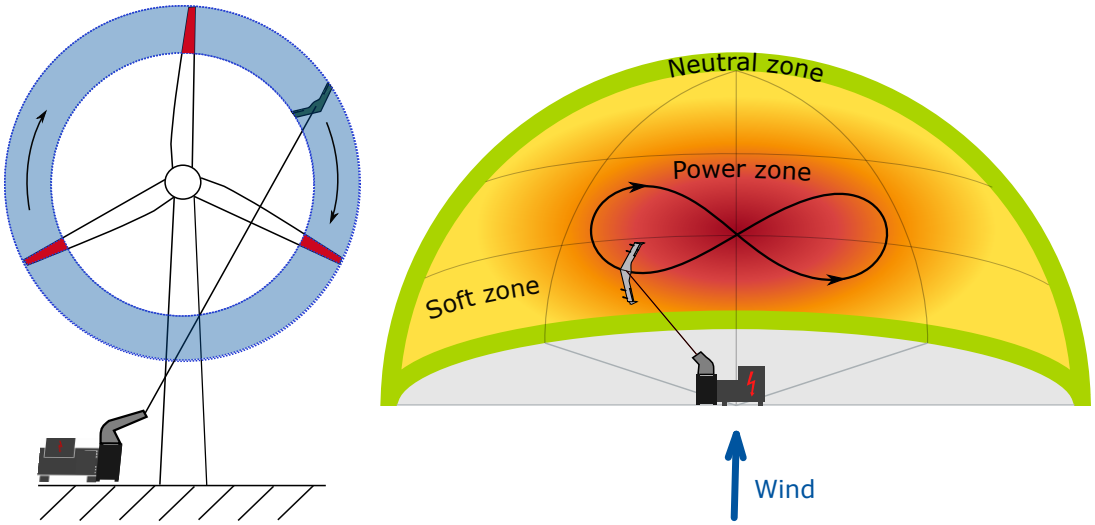
The first ideas of windmills were realized in the 9th century [27] and since then, further developments and improvements have led to modern wind turbines that can reach an average rated power of around 8 MW offshore with a hub height of 120 m in 2023 [28]. In an early study by Betz [29], he investigated the theoretical maximum power output of a wind rotor for an unsteady, incompressible, frictionless and one-dimensional flow and concluded a maximum power coefficient close to $c_P = 0.6$ that can be extracted from the total wind power. Combined with the air density ρ, the wind velocity V_w, and the swept area of the turbine blades S_s, the power P can be calculated, as shown in Eq. 1.1.

$$P = \frac{\rho}{2} \cdot V_\mathrm{w}^3 \cdot S_\mathrm{s} \cdot c_P \tag{1.1}$$

Current wind turbines are already approaching Betz's maximum; the highest actual power coefficient is between 0.45 and 0.5 [30]. For further improvement, the wind velocity with its cubic influence on power has a significant influence. Since the wind is stronger and more consistent at higher altitudes, a high hub height is sought. However, the structure of the wind turbine limits the maximum height, as the nacelle, tower and foundation increase in size with height. These components are already dominant cost factors in current wind turbines. In [31], the levelized cost of electricity (LCOE) for land-based wind power plants is listed with the highest spendings in operation and maintenance (31.4 %), nacelle (23.3 %), rotor (13.7 %), and tower (10.3 %). Combined with limited designated space, low public acceptance due to noise, and environmental issues as well as bureaucracy, the greater expansion of wind energy is limited.

Airborne wind energy is an emerging technology, which represents an expedient addition to wind turbines. The technology uses aerodynamic lift devices to convert wind energy into electricity. An airborne flight system that is connected with a tether to the ground performs circular or lemniscate patterns in the downwind direction in the so-called crosswind flight. During flight, the aerodynamic forces acting on the flight system are converted into power output. The pattern of the flight system solely represents the outer part of the wind turbine blade, which has the highest angular velocity and therefore converts the most power, as shown in Fig. 1.2a. This approach reduces the material expenditure of a classical wind turbine to a tenth, since it only consists of the parts relevant for power generation. Additionally, it allows the AWE system to be deployed in remote areas where the terrain is

unsuitable for wind turbine construction. Most importantly, it is expected to reach greater heights to harvest stronger wind forces and maximize power output. [21, 32, 24, 33]



(a) Comparison of the flight cycle of a wind turbine with an AWE system.

(b) Definition of the different flight zones with respect to the wind vector.

Figure 1.2.: Flight principle of AWE, following the ideas of [32].

The wind vector is the relevant reference of the flight procedure and defines the direction of crosswind flight. Figure 1.2b marks the different zones in the flight sphere related to the wind vector. In the neutral zone ranging from the zenith to the outer border perpendicular to the wind vector, minimum forces act on the flight system due to the wind velocity. On passing the soft zone, the power zone is in the downwind direction, where maximum power is generated. Crosswind flight is operated in the power zone when the ambient wind velocity is above the so-called cut-in speed of the flight system to generate power [24].

The specific operation in crosswind flight can mainly be divided into ground-generation (ground-gen, or lift mode) and fly-generation (fly-gen, or drag mode) systems, based on the generator location [24, 22]. On the one hand, ground-gen systems mechanically transfer the part of the aerodynamic lift force in tether direction to the ground. The flight system performs patterns in two cycles. In the generation phase, the flight system increases its distance to the ground and unwinds the tether from a winch, which drives a generator to convert the wind power into electrical energy. Once the tether is completely extended, the flight system returns during the retraction phase to its initial position and the whole process restarts. In order to achieve a positive net energy output, the flight path and aerodynamic characteristics of the flight system are adjusted so that the power produced during the generation phase outweighs the power consumption during retraction. On the

other hand, fly-gen systems maintain the distance to the ground, while the aerodynamic velocity drives the propellers on the wing, which act as a repeller. Power is generated on board and transmitted electrically downwards via the tether. [32]

Both fly-gen and ground-gen systems have been realized successfully in the past with various flexible or fixed wing flight systems [24, 22, 34], and several studies compare the specific advantages and the power output of each system [35, 36, 22]. In the first and most prominent study of AWE by Loyd [21], the formula for the maximum power output ($P_{\mathrm{max,loyd}}$) is derived under the assumptions of a system without tether drag and ideal flight conditions, among others, as shown in Eq. 1.2. The equation is valid for both fly-gen and ground-gen systems. In addition to the wing area S, it includes the lift-to-drag ratio ${}^{C_L^3}/_{C_D^2}$. A large wing area and a high lift-to-drag ratio are relevant in the design of the flight system to achieve high performance.

$$P_{\mathrm{max,\,loyd}} = \frac{2}{27} \cdot \rho \cdot V_{\mathrm{w}}^3 \cdot S_{\mathrm{w}} \cdot \frac{C_L^3}{C_D^2} \tag{1.2}$$

1.1.1. Flight System

In the context of this thesis, a flying wing in tailsitter configuration is selected as a flight system, also referred to as AWE system. The reasons for this selection listed as follows:

- The flight system is reduced to the wing as the relevant, lift-generating component to reduce drag and lead to high performance in accordance with Eq. 1.2.
- A tailsitter configuration allows for controlled vertical takeoff and landing within a limited area. This increases operational flexibility by eliminating the need for ground support for takeoff, allowing a takeoff from almost any location.
- The flight system can operate completely independent of the tether. This is particularly important during incidents with a loss of control, where a tether release must be performed to remove the external tether forces and to restabilize the flight system. Besides, the flight system can be operated beyond the AWE application, e.g. to maneuver to a maintenance station. As operation and maintenance have been identified as a major cost driver for wind turbines, this can significantly improve the LCOE, especially in offshore applications.
- The configuration of the flight system allows for a versatile application of either a ground-gen or a fly-gen system.

The flight system with its technical data is presented in Fig. 1.3. It has a takeoff mass of 14.5 kg and a wing area of 1.6 m^2. The wing has an increased chord in the center segment to increase the wing area for high performance in crosswind flight. The elevons are extended at the trailing edge for greater control authority. The sweep of 15° is combined with a twist of 4.5° at the wing root decreasing to -1° at the tip for washout, see Section 2.3.1. Two winglets on each side provide directional stability and are reinforced at the rear to act as struts during VTOL.

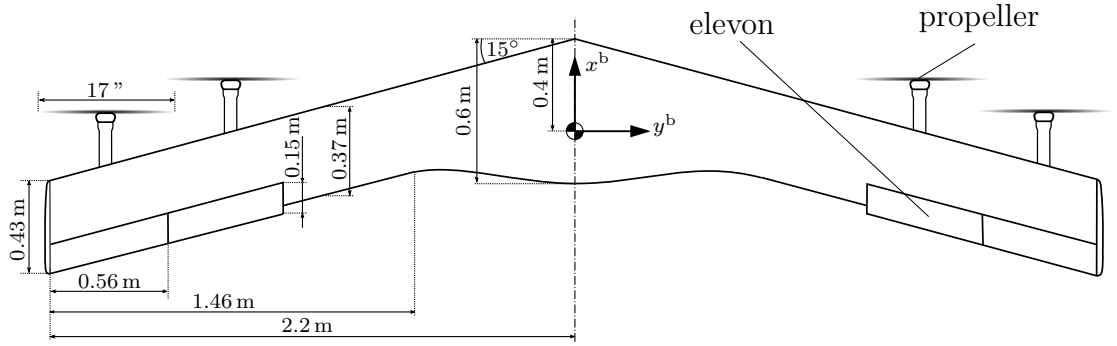
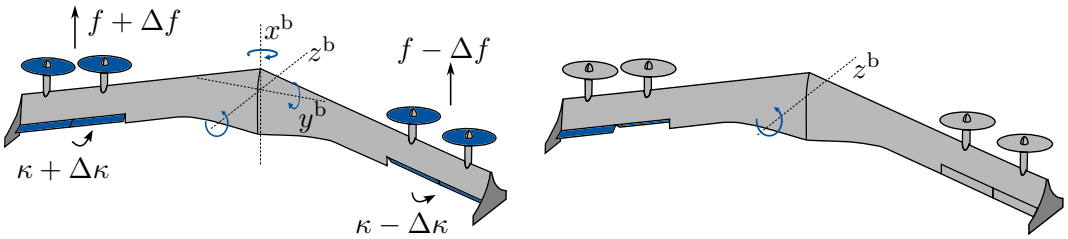


Figure 1.3.: Technical drawing of the flight system.

The airfoil of the flight system is the reflexed airfoil HS 3.4/12.0B and is specifically designed for gliders with a large span over 4 m. It is characterized by its large relative camber of 3.4 % and a relative thickness of 12.0 % of the chord length, resulting in a high lift coefficient in crosswind flight. The airfoil has smooth stall effects and a constant pitch moment coefficient C_m close to zero for low trim resistance. [37]

The propulsion system is designed with four propellers in line with the leading edge of the wing. It is equipped with four elevons that are positioned below the center of the propellers to be in their slipstream. This ensures an airflow over the elevons to guarantee control authority even in a vertical hover flight without aerodynamic velocity. A uniform deflection of all elevons (κ) induces a pitch moment around the body-fixed y^b-axis, while a symmetrical differential deflection ($\Delta\kappa$) on both sides in opposite directions induces a roll moment around the x^b-axis, as shown in Fig. 1.4a. The velocity is controlled by uniform thrust (f), while a symmetric differential thrust (Δf) in opposite directions generates a yaw moment around the z^b-axis. The definition of the controls follows the typical convention that a positive deflection results in a negative generated moment. The propulsion system is designed with sufficient reserve to ensure a safe landing even if one power unit fails. In crosswind flight, the yaw moment is induced by a differential deflection of the elevons, as shown in Fig. 1.4b. In this thesis, the independent control of only one thrust or elevon unit is not considered and the flight control is reduced to the four controls of uniform or symmetric deflection or thrust ($\kappa, \Delta\kappa, f, \Delta f$).



(a) Controls during VTOL [38]. (b) Yaw control during crosswind flight [39].

Figure 1.4.: Controls and generated moments of the flight system.

The main challenge of the specific configuration of the flying wing during VTOL is the longitudinal pitch motion [38]. The flight system has no horizontal stabilizer or elevator, and the lever arm of the elevons in the longitudinal direction is small. As a result, the pitch control is limited and the pitch attitude is naturally unstable. This is particularly challenging in prop-borne flight, when an aerodynamic velocity acting perpendicular to the large wing area induces significant pitching moments. Combined with the limited control authority, this results in a reduced flight envelope in the longitudinal motion, see Section 3.2. A detailed discussion of the flight system's design to improve the flight envelope can be found in [39].

1.1.2. Launching Phase - State-of-the-Art

The launching phase represents the initial flight phase from takeoff and transition to entry into crosswind flight. Although this phase is only a short period in the initialization of the overall flight cycle, it is an important and challenging flight phase. A reliable launch strategy is a necessary criterion for a matured flight within a continuous, automated operation of the AWE system in a wind park. At any time, the flight system can be forced to land and a subsequent re-launch is required. For example, in the event of a malfunction or for maintenance, as well as when the wind velocity falls below the cut-in speed or reaches the maximum limits of the flight system. Thus, the duration of the launching phase may be short, but the number of launches can be quite large. A robust maneuver is crucial since it is performed close to the ground, where an incident is dangerous. Additionally, it should be operable in the maximum range of different wind velocities from low to high, while taking into account the geometric constraints imposed by the tether connection. For self-propelled fixed wings, a fast launch in a limited space is important for low power consumption, as it reduces the overall power output of the AWE system. It also determines the size of the on-board batteries. Larger batteries lead to higher mass and an upscaling of the overall system in terms of the mass-growth factor. [34, 40, 41]

The main and most complex part of the launching phase is the transition of the flight system to achieve wing-borne flight. Since the weight of a flexible wing is low, these flight systems can be lifted with the support of the wind by placing the kite in the downwind direction of the winch. Fixed wings require a minimum flight velocity above the cut-in wind speed for wing-borne flight, and must therefore be accelerated externally or by onboard propellers. Accordingly, the transition has to be tailored to each flight system, and different strategies are highly distinctive in the literature. Despite the extensive scientific literature on flight operation and control in crosswind flight, the literature dealing with the general launching phase of AWE systems is still largely uncovered [42, 34]. However, the main characteristics shall be outlined in the following in order to capture the existing launch strategies of current and former companies.

According to [43], the different launch strategies can be classified in the following categories: launch with the support of a telescopic mast, a rotating arm, a catapult, or an independent, vertical take-off, see Fig. 1.5. A telescopic mast is utilized for flexible wings, e.g. of Skysails Power or Kitepower [44, 45]. The kite is placed on the mast facing downwind and can be launched directly into the power zone. A control pod allows roll and pitch control by steering the length of the kite's bridles. The EnerKite GmbH [46] makes use of a rotating arm to launch a flying wing. With azimuthal rotations, a spinning arm accelerates the kite for a launch with a stretched tether. This avoids the carry-on of additional propulsion systems but increases the complexity of the system as it is highly nonlinear and requires robust control [47]. A catapult has been tested e.g. by Ampyx Power [48], and is being investigated within several studies [49, 42]. For launch, the tethered flight system is accelerated by the winch and then ascends to reach the power zone to initiate crosswind flight. However, the concept requires additional space on the ground for the catapult launch.



(a) Telescopic mast, © *SkySails* [50]. (b) Rotating arm, © *EnerKite* [51]. (c) Catapult, © *Ampyx* [52]. (d) VTOL, © *Makani* [53].

Figure 1.5.: Launching concepts of airborne wind energy systems. (*Note: Cropped images*)

Launch strategies including a vertical takeoff of the flight system require minimal space on

the ground. For example, Kitemill [54] or the TwingTec AG [55] are working on a flight system with additional propellers that provide vertical thrust for VTOL. The thrust is augmented in prop-borne flight by the aerodynamic forces due to the wind velocity at the wing. The former company Makani Technologies LLC has integrated a flight system in tailsitter configuration [56]. In their final technical reports, they have published a detailed overview of the flight concept and controller, including challenges and best practices [57]. A horizontal stabilizer and differential thrust stabilize the longitudinal motion of the flight system. This allows the flight system to take off directly in the power zone with a stretched tether and the support of eight thrust units and the force of the wind. With a down-pitch motion, the flight system transitions and operates into crosswind flight. The exact radial position is not controlled during prop-borne flight, while the horizontal component of the tension is controlled by thrust. The roll motion around the geodetic azimuth axis is controlled passively by a bridled tether, which, however, demonstrates deficiencies in the event of a loss of tether tension. KiteKRAFT for example, is continuing this work and has developed a flight system with a boxplane and an H-empennage for tailsitter launches [58]. The elevons are positioned in the downwash of the propellers to provide active roll control during prop-borne flight to overcome the issues of passive roll control of Makani [59].

The different concepts and advantages are summarized and compared in detail in [47, 34, 22]. Due to the high variability of the flight systems and the launching strategies, flight control is individual for each system. The flying wing in tailsitter configuration of this thesis represents a further specific flight system configuration with unique characteristics regarding its vertical takeoff capability and flight envelope. In combination with the general requirements of the launching phase, this leads to a specific problem definition that must be addressed by the flight control.

1.2. Objective and Structure of Work

The objective of this thesis is to design a launch trajectory controller that controls the aerodynamic velocity for the transition of a flying wing from prop-borne to wing-borne flight and vice versa. The controller must be explicitly designed for operations including low and strong, dynamic wind fields within the application of an airborne wind energy system. The controller has to comply with the specific limitations of the system's flight envelope and the requirements of the launching phase in terms of low power consumption and in particular high robustness to wind disturbances. The operation has to take into account the tether constraints while providing additionally the possibility of tether-independent flight. The stabilization of the natural instabilities of the flight system's attitude is a necessary criterion that must be integrated into the control architecture.

To address this objective, a suitable launching strategy is selected for the flight system that is compatible with the requirements regarding the tether constraints and the limited flight envelope. Based on a thorough investigation of the trim states of the transition, a favorable path of operating points from prop-borne to wing-borne flight is selected under consideration of sufficient control reserves regarding elevon deflection and thrust. The flight trajectory controller integrates all flight axes for holistic control of the transition while adapting the orientation of the flight system to a dynamic rotating wind vector. The focus of this thesis is placed on the velocity controller, which incorporates the selected operating points and controls the aerodynamic velocities during the transition.

The design of the controller requires a detailed model of the flight system and the tether, which is described in Chapter 2. The vertical takeoff capability expands the occurring limits of attitude and aerodynamic angles encountered during flight operations of conventional flight systems and can exceed 90°. The particularities of the stability of the attitude are outlined and a suitable descriptive form of the attitude, the aerodynamic model, and the trim condition forms the basis for evaluating the full flight envelope of the flight system.

The transition of the flying wing with vertical takeoff capability has similar characteristics to the transition of tailsitter flight systems. Given the limited literature on flying wings in the context of AWE, Chapter 3 explores the state-of-the-art of tailsitter flight systems. This includes an examination of various trajectory concepts and control methods. The main differences to the AWE system are presented in the following, focusing on the flight envelope of the longitudinal motion and highlighting its main characteristics.

Chapter 4 presents the design of the launch trajectory controller as the core of this thesis. Following a detailed description of the design objectives, a suitable launch concept is outlined for the flight system. For the corresponding transition, a detailed analysis of the flight envelope is conducted to define a favorable trim path. A suitable control concept is designed for the dynamic transition of the flight system, integrating this trim path as the operating points of the velocity controller. While all control cascades are introduced, a focus is placed on the implementation of this velocity controller.

In Chapter 5, the launch trajectory controller for the transition is discussed and validated using nonlinear simulation results. Accurate disturbance rejection in response to a rotating wind field is particularly decisive during prop-borne flight. Therefore, simulation and flight test results verify the applicability of the flight trajectory controller during this flight phase in strong wind conditions. This validation is complemented by a linear robustness analysis with selective insertion of parameter uncertainties to verify stable flight in various wind conditions. This thesis closes with a detailed conclusion in Chapter 6.

2. Flight Mechanics and Model of the AWE System

The design and evaluation of a trajectory controller for the transition requires a comprehensive understanding of the fundamental principles of flight dynamics specific to flying wings. Aerodynamics and flight dynamics of flying wings in wing-borne flight are already extensively covered in the current literature [60, 61, 62]. However, the application of the flying wing in a tailsitter configuration expands the flight envelope to vertical, prop-borne flight and therefore requires an enhanced model of aerodynamics. The following sections outline the relevant coordinate systems and transformations and present the definition of the trim states. A focus is placed on the specific characteristics of the stability of the flying wing's attitude in prop-borne flight. Finally, the model of the AWE system is presented with particular emphasis on aerodynamics and the tether.

2.1. Coordinate Systems and Transformations

The introduction of suitable frames and coordinate systems facilitates the description of the flight system's motion [63]. Four relevant frames are defined with the following assumptions. The Earth is considered as an inertial frame, and the wind frame is a homogeneous moving system representing the low-frequency wind field with no gusts and a constant height profile within the close region around the body frame of the flight system. The tether is considered as a quasi-static frame whose curvature and length depend on the current flight state and tether load. For each frame, a coordinate system is introduced to describe the particular motion, as shown in Fig. 2.1.

The geodetic coordinate system of the inertial frame is on the ground with the x^{g}-axis and y^{g}-axis pointing to the north and east, respectively, and the z^{g}-axis pointing to the center of the Earth. The body coordinate system is placed at the center of gravity of the flight system, with its x^{b}-axis pointing to the nose, its y^{b}-axis to the right wing tip, and its z^{b}-axis orthogonal to the other base vectors towards the bottom. The tether coordinate system is positioned at the winch on the ground. The size of the winch is neglected in this thesis. The z^{t}-axis points in the direction of the resulting line load of the tether, compare with Sec. 2.4.2. The z^{t}- and y^{t}-axes span a plane with the line load and the position vector of the flight system. Again, x^{t} is orthogonal to the other vectors. The wind frame shall be

defined within this thesis by the wind coordinate system pointing with the y^{w}-axis against the main wind direction, the z^{w}-axis towards the ground and the x^{w}-axis orthogonal to each other.

The relative velocity can be considered between different frames. The body or kite velocity relative to the inertial frame is typically referred to as the ground velocity $\vec{V}_{\mathrm{G}}$, while the ambient wind velocity $\vec{V}_{\mathrm{W}}$ defines the velocity of the wind frame relative to the ground. The apparent, aerodynamic velocity $\vec{V}_{\mathrm{A}}$ is the relative velocity between the body and the wind frame, following the relation $\vec{V}_{\mathrm{A}} = \vec{V}_{\mathrm{G}} - \vec{V}_{\mathrm{W}}$. Thus, the aerodynamic coordinate system is further introduced with the x^{a}-axis in the direction of the aerodynamic velocity, y^{a}-axis in the x^{a}- and y^{b}-plane, while the z^{a}-axis is oriented orthogonally to both. It is positioned at the center of gravity of the flight system. While the coordinate systems are indexed with superscripts, the frames are indexed with subscripts. Unless otherwise indicated, the state vectors of these frames are related to the inertial system, which is not further indexed in this thesis.

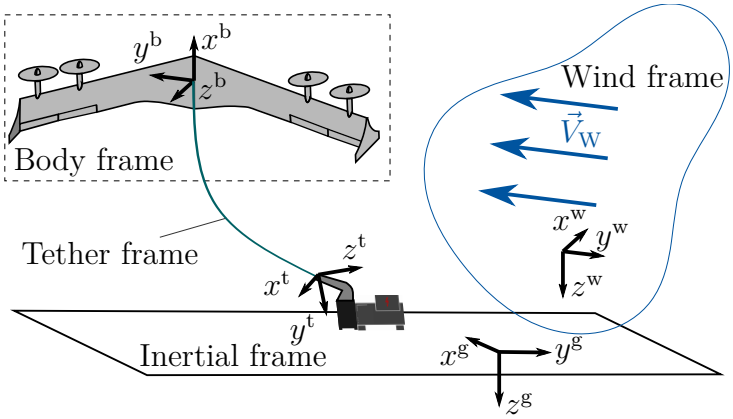


Figure 2.1.: Relevant frames and coordinate systems.

2.1.1. Euler and Aerodynamic Angles

The rotation between two coordinate systems can be described by the Euler and aerodynamic angles. Due to the unique motion of the flight system during the transition, different rotation sequences and angles fasciliate the specific modeling and control tasks and their definitions are defined in the following.

Analogous to [64], a general vector defined by an underline is introduced for the Euler angles from the geodetic to the body coordinate system, see Eq. 2.1. Φ describes the roll rotation around the x-axis, Θ the pitch rotation around the y-axis and Ψ the yaw rotation around the z-axis. These axes do not form a right-angled coordinate system but follow the

definition of the rotation order. In flight dynamics, the most common rotation order is the x-convention, which describes the z-y-x rotation sequence. The coordinate system is first rotated around its z-axis, followed by a y-rotation and a final x-rotation. In addition to the x-convention, the y-z-x and z-x-y rotation orders are utilized in this thesis. For unambiguous identification, the rotation angles are indexed with the corresponding rotation order, e.g. $\underline{\Phi}_{zyx}$. The linearization of the current flight state requires an infinitesimal consideration of modifications of the flight system's attitude from a given linearization point. As such, these deviations of the flight attitude are marked with $\delta\underline{\Phi}$. Note that for example $\delta\Psi$ corresponds to a deviation of the yaw angle which is applied as a small rotation along the z^{b}-axis after the overall rotation of the flight system's attitude of the given linearization point.

$$\underline{\Phi} = [\Phi, \Theta, \Psi]^{\top} \tag{2.1}$$

The aerodynamic angles α and β define the rotation between the aerodynamic and body coordinate systems. According to [64], the rotation order from the aerodynamic coordinate system to the body coordinate system is defined first, by a negative rotation around the z^{a}-axis by the slip angle or sideslip β and second, by a subsequent rotation around the y-axis by the angle of attack α. The rotation between the geodetic and the wind coordinate system requires only a single rotation around the z^{g}-axis with the rotation angle Ψ_{w}. It describes the main wind direction under the assumption of a purely horizontal wind.

2.1.2. Quaternions

Euler angles can be interpreted intuitively, but suffer from discontinuities and an inherent singularity, also known as gimbal lock [65]. The singularity occurs at a pitch angle of 90° and hence, during vertical flight of the flying wing. Therefore, quaternions are presented in the following to allow for a continuous description of all attitudes in 3D space. The focus is placed in the following on the formulations for the coordinate transformations and attitude descriptions that are relevant for the specific flight control task, and it is referred to the common literature for a detailed mathematical description of quaternions [66, 67].

A quaternion is a hypercomplex number that was first introduced by Hamilton [68] as part of the mathematical group of Hamiltonian algebra [69]. The basic idea is that a 3D rotation can be represented by a rotation around a single axis in the hypercomplex plane. This reduces the computational effort compared to the Euler angle rotation and allows for a holistic description of the attitude without singularities. In its vector representation,

a quaternion consists of a scalar part and a vector part $\vec{u}_q$ with components in the three complex axes i, j, k, see Eq. 2.2 [70]. For a unit quaternion, $\vec{u}_q$ defines the axis of rotation and Θ_q the angle of rotation. For consistency with the Euler angles and to avoid conflicts with rate and attitude variables of flight dynamics, the index q is added and the quaternion $\underline{q}$ is underlined. The transformation of vectors and coordinate systems can be found in Appendix A and the general conversion between Euler angles and quaternions is explained in detail in [71]. The differential $\dot{\underline{q}} = \frac{\mathrm{d}}{\mathrm{d}t}\underline{q}$ is defined according to Eq. 2.3. $\vec{\omega}_{\mathrm{b}}^{\,\mathrm{b}} = [p, q, r]^\top$ describes the angular rates of the flight system in the body coordinate system.

$$\underline{q} = \cos\left(\frac{\Theta_q}{2}\right) + \underbrace{\vec{u}_q}_{[u_i, u_j, u_k]^\top} \cdot \sin\left(\frac{\Theta_q}{2}\right) \in \mathbb{H} \tag{2.2}$$

$$\dot{\underline{q}} = \frac{1}{2} \cdot \underline{q} \otimes \begin{bmatrix} 0 \\ \vec{\omega}_{\mathrm{b}}^{\,\mathrm{b}} \end{bmatrix} \in \mathbb{H} \tag{2.3}$$

The deviation of attitude angles between two coordinate systems is of further relevance for flight control to minimize the error between a commanded (cmd) and actual attitude. In [72], the error quaternion $\delta\underline{q}$ is described for the application of attitude control, see Eq. 2.4. $\underline{q}^{-1}$ denotes the quaternion inverse and $\otimes$ the Kronecker product, see Appendix A. The expression is valid for small but for control engineering sufficiently large deviations in attitude. The vector part of the error quaternion can be mapped concerning Eq. 2.2 to an angular deviation $\delta\Theta_q$ in each axis. A negative sign of the scalar part indicates that the attitude difference is greater than 90°, in which case the conjugate of the error quaternion can be utilized for rotation in the shorter, opposite direction [73].

Quaternions can be utilized for spherical interpolation between two attitude angles. Especially in the region of the singularity and the discontinuities of the Euler angles, linear interpolation (lerp) does not result in a constant motion. Slerp (spherical linear interpolation) is therefore utilized [74], which ensures an interpolation between two unit quaternions along the shortest path. It is used for a smooth transition with a constant turning rate between two quaternions. Equation 2.5 presents the calculation for the interpolated quaternion $\underline{q}_{\mathrm{slerp}}$ at the sample point of $t_q \in [0, 1]$ between the two considered quaternions $\underline{q}_{\mathrm{A}}$ and $\underline{q}_{\mathrm{B}}$. Ω_q defines the rotation angle between the two quaternions, see Appendix A.

$$\delta\underline{q} = \underline{q}_{\mathrm{cmd}} \otimes \underline{q}^{-1} \in \mathbb{H} \tag{2.4}$$

$$\underline{q}_{\mathrm{slerp}}(\underline{q}_{\mathrm{A}}, \underline{q}_{\mathrm{B}}, t_q) = \frac{\sin\left[(1 - t_q)\Omega_q\right]}{\sin(\Omega_q)} \cdot \underline{q}_{\mathrm{A}} + \frac{\sin(t_q \cdot \Omega_q)}{\sin(\Omega_q)} \cdot \underline{q}_{\mathrm{B}} \in \mathbb{H} \tag{2.5}$$

2.2. Trim Condition

Flight control design often relies on stationary trim states. It allows the identification of an optimal flight path guided by specific design criteria regarding stability, controllability, or robustness, and their linearized models enable accurate controller design [57, 75, 76]. During the transition of the AWE system, the operating points vary significantly, requiring a detailed analysis of the trim conditions in the entire flight envelope.

A trim condition of a flight system defines the state, in which all forces and moments are balanced so that no change in the state of motion occurs [77]. The stationary trim states for which the flight controller is designed are defined as the operating points. For a given flight state, defined by the aerodynamic flight velocity $\vec{V}_\mathrm{A}$, a specific set of attitude angles $\underline{\Phi}$ and controls regarding thrust demand and elevon deflection is required to maintain the current trim state. These controls are defined in this thesis as trim controls $\vec{u}_\mathrm{t}$, while the sequence of consecutive trim states are defined as the trim path. According to Eq. 2.6, trim states are specified that balance the functions f_i of the forces and moments in each axis $\{FM\} = [X, Y, Z, L, M, N]^\top$, which result from the flight model.

$$\{FM\}_i = f_i(\vec{V}_\mathrm{A}, \underline{\Phi}, \vec{u}_\mathrm{t}) \stackrel{!}{=} 0 \tag{2.6}$$

The trim states are calculated based on Eq. 2.6 for the relevant flight velocities $\vec{V}_A$. A trim condition can be well-defined, underdetermined or overdetermined. This depends on the number and direction of effects of the flight controls and state variables. In a defined trim condition, there are a unique combination of trim controls and attitude angles that satisfy the trim condition. Implicitly, this means that the flight system's attitude is not freely selectable independent of the velocities, but results uniquely to trim the desired flight velocity. In an underdetermined trim condition, there are more control combinations to trim the flight system. Depending on the degree of freedom, the attitude angles can be selected independently based on additional demands for flight performance or robustness requirements. An overdetermined system usually cannot be trimmed because the flight controls are unable to apply the desired forces or moments in all axes. This condition does not apply to the given flight system and is not considered in the following. However, the required flight states of defined and underdetermined systems do not necessarily imply that these states can be trimmed due to the natural limits of the flight controls. In this case, the formulation in Eq. 2.6 also allows the insertion of fixed accelerations instead of the equilibrium condition to analyze the nonstationary flight behavior or to design the controller for nonstationary flight.

2.3. Attitude Stability

The attitude stability of flying wings differs from conventional flight systems mainly due to the missing horizontal and vertical stabilizers. While the stability of wing-borne flight of flying wings has been extensively investigated [60, 61], prop-borne flight of flying wings with VTOL capability is a relatively uncovered area. Yet, it is characterized by significantly changing aerodynamic forces and moments, and therefore modified stability margins. This section defines stability and outlines its main characteristics. Attitude stability can be related to the three flight axes. The subsequent sections briefly describe the stability of a flying wing with VTOL capability for each axis. The general stability of flying wings in wing-borne flight is explained, with a focus on the distinctive characteristics in prop-borne flight, using simplifications to highlight the major differences. It describes typical phenomena that dominate during flight with a vertical attitude leading to instability, without claiming exhaustiveness. For a detailed analysis, the complete flight model must be considered, as it will be conducted in Section 3.2 for the longitudinal stability of the flight system.

Stability can be divided into static and dynamic stability. Static stability describes the tendency of a flight system to return to its equilibrium state after perturbations such as gusts, turbulence, or through the tether. The dynamics of this returning motion are described by dynamic stability and are characterized by damping and the natural frequency of the oscillations. It describes the time course of the motion back to its equilibrium. Static stability does not guarantee dynamic stability; an undamped returning motion may be statically stable but not dynamically. [78]

Static and dynamic stability can be analyzed using the linearized state-space formulation, see Eq. 2.7. A_{ss} represents the system matrix, B_{ss} the input matrix, C_{ss} the output matrix and D_{ss} the feedthrough matrix. $\vec{x}$ describes the state vector, $\vec{u}$ the input vector and $\vec{y}$ the output vector. The symbol δ indicates that only deviations from the operating point OP of the current state are considered. The equilibrium trim state $\delta\vec{x_{\mathrm{t}}} = 0$ is statically stable, if A_{ss} is non-defective and all eigenvalues λ_{s} satisfy the condition $\mathrm{Re}(\lambda_{\mathrm{s}}) \leq 0$. Damping and natural frequencies can be calculated with the eigenvalues to evaluate dynamic stability. [79]

$$\begin{aligned} \dot{\vec{x}} &= A_{\mathrm{ss}}(OP) \cdot \delta\vec{x} + B_{\mathrm{ss}}(OP) \cdot \delta\vec{u} \\ \delta\vec{y} &= C_{\mathrm{ss}}(OP) \cdot \delta\vec{x} + D_{\mathrm{ss}}(OP) \cdot \delta\vec{u} \end{aligned} \tag{2.7}$$

Flight systems are typically designed with sufficient natural stability for a safe operation. However, flying wings are naturally unstable without explicit design adjustments, and automated control is required to account for artificial stability by adjusting the flight controls accordingly to maintain the desired flight state. Unstable flight systems have the advantage of improved controllability since the absence of a resetting force reduces the control effort and allows them to perform rapid maneuvers more effectively. [78, 64]

Flight instability can be characterized by the time to double amplitude [80]. It describes the time it takes for the associated acceleration of a disturbance to double its amplitude. A minimum time is required to allow actuators with their upper control and dynamic limits to compensate for the disturbance. Otherwise, the disturbance may dominate the flight motion, leading to an uncontrollable state. Therefore, a tradeoff between enhanced controllability and instability limits is required.

2.3.1. Longitudinal Stability

The longitudinal stability of the flight system means the stability of the pitch motion around the lateral y^{b}-axis. For stable, wing-borne flight, an increase in the angle of attack due to a perturbation creates a down-pitching moment, such that the angle of attack decreases and the flight system returns to its equilibrium state. The stability margin is defined as the difference between the aerodynamic center (AC) and center of gravity (CoG), related to the mean aerodynamic chord [81]. For stable operation, the AC must be placed behind the center of gravity. Since this creates a general down-pitch moment, an additional pitch-up moment must be induced to allow trimmed flight.

Flying wings typically have an inherent instability in the longitudinal axis [60]. To increase stability, the airfoil is commonly designed with a reflexed camber line such that the rear part is raised. This affects the moment coefficient of the airfoil and can be used to achieve a pitch moment close to zero to minimize the required offset moment. However, it comes at the cost of reduced lift and increased drag [82]. Therefore, a moderate reflexion can be combined with wing sweep to move the AC of the outer wing sections backward to increase their lever arm and take advantage of washout [83]. It describes the phenomenon of the wing design with a combination of twist and sweep. The angle of incidence along the span is reduced, which deliberately reduces lift at the wing tip. In case of a disturbance that increases the angle of attack, stall occurs first in the center segment of the wing, while the outer parts of the wing still generate lift and induce a down-pitching moment to reset the disturbance.

In prop-borne flight, the longitudinal stability can be considered with the following thought model, see Fig. 2.2. The flight system is initially in a trimmed, vertical flight, in which thrust T equalizes weight W. A perturbation occurs in the form of a horizontal inflow Δu. The aerodynamic characteristics in vertical flight differ from those in wing-borne flight and resemble the aerodynamics of a flat plate. The horizontal inflow generates mainly drag D, while lift is neglectable. The center of pressure is located in the centroid of the wing area at 50 % of the mean aerodynamic chord l_μ [84]. For a center of gravity above this center of pressure, the perturbation induces a pitch moment M, which leads to a horizontal acceleration due to the tilted thrust vector (see the dotted, perturbated wing in Fig. 2.2). In return, this further increases the inflow perturbation. There is no resetting moment back to equilibrium and the flight state is naturally unstable.

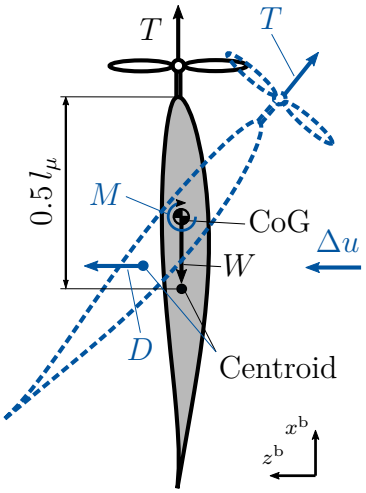


Figure 2.2.: Thought model for longitudinal stability in prop-borne flight.

2.3.2. Lateral Stability

Lateral stability describes the roll stability around the x^b-axis, which results only implicitly due to a slip angle. In wing-borne flight with a roll angle, the lateral component of gravity causes a slip angle, which in return can induce a resetting roll moment. When the flight system is designed with a positive dihedral or a backward sweep of the wing, lift is increased on the side exposed to the flow with sideslip and decrease the roll angle back to equilibrium.

In prop-borne flight, high slip angles up to 90° can occur when the flight system accelerates laterally. The flight system requires only a small yaw angle to achieve high lateral velocities since the lateral surfaces are small and have reduced drag. Figure 2.3 depicts the relevant forces due to a lateral inflow Δv at a slip angle of 90°. In this direction, the wing surface

resembles a flat plate with an aerodynamic center at the quarter chord point [85], which is in this case related to the span width. The CoG is assumed in the lateral center for a symmetrical flight system. From this lateral point of view, the aerodynamic center is accordingly in front of the CoG and the lift of the wing L_{wing} induces a positive roll moment L. This increases the relative angle of attack of the lateral inflow and therefore lift, leading to a natural instability in the lateral axis [86]. Note that the slipstream of the propellers also affects the flow, and for reduced slip angles below 90°, a more detailed aerodynamic approach is necessary, see Sec. 2.4.3.

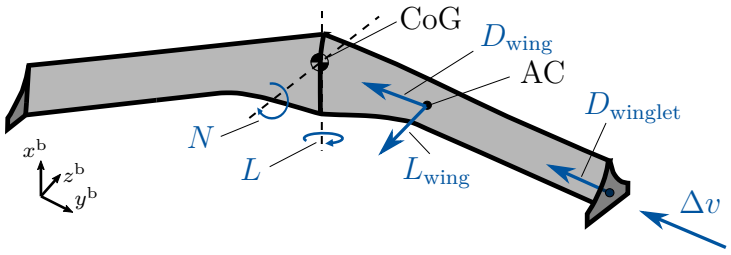


Figure 2.3.: Thought model for lateral and directional stability.

2.3.3. Directional Stability

Directional stability describes the stability around the z^{b}-axis, also called weathercock stability. When an inflow with slip angle occurs, a stable flight system rotates its nose in the direction of the inflow to reduce the slip angle. As such, the stability does not refer to returning to the original flight attitude, but to adapting to a rotated inflow direction. In wing-borne flight, a positive dihedral and a backward sweep of the wing both increase drag on the side exposed to the flow with sideslip, resulting in the desired yaw moment to reduce the sideslip. The stabilizing effects can be enhanced by winglets. On a swept wing, they are positioned behind the CoG, such that the aerodynamic forces at the winglets generate a stabilizing yaw moment. [87, 60, 88]

During prop-borne flight with a lateral disturbance Δv at high slip angles, the winglets of the flying wing act as drag elements since the inflow is perpendicular to their area. This induces a positive yaw moment N in the direction of the inflow, see Fig. 2.3. The drag of the wing also contributes partly to this yaw moment. The yaw moment induces a lateral thrust component, which further accelerates the flight system in the direction of the inflow. In this case, the tendency of the flight system to reduce its slip angle leads to instability. Since the vertical flight attitude corresponds to a theoretical slip angle of 90°, the reduction of the slip angle due to a lateral disturbance corresponds to a motion away from this vertical equilibrium. The flight system tilts in the lateral direction and reinforces the disturbing inflow. Hence, the flight system is directionally unstable.

2.4. Model of the AWE System

Flight controller design and system analysis require a detailed model of the flight system's control plant. This model describes the motion of the flight system with respect to the surrounding atmosphere. It includes high aerodynamic angles that can occur during the transition of the flying wing and the tether forces acting within the AWE application. In the following, an overview is given of the various components of the control plant with a focus on the tether and aerodynamic models.

2.4.1. Model Structure

The structure of the flight model is based on [89] and is depicted in Fig. 2.4. The central element is the block of the equations of motion, which contains the rigid body assumptions. The equations contain the principle of linear and angular momentum and are solved based on all forces and moments acting on the flight system. The differential equations of the attitude of the flight system are formulated using quaternions to avoid singularities, see Eq. 2.3. The equations of motion output the flight state with all relevant state vectors $\vec{x}_{\text{motion}}$, including the position $\vec{s}^{\,\text{g}}_{\text{b}}$, velocity $\vec{V}^{\,\text{b}}_{\text{G}}$, angular rate $\vec{\omega}^{\,\text{b}}_{\text{b}}$ and Euler angle $\underline{\Phi}_{zyx}$ vectors, as shown in Eq. 2.8. The state vector is adjusted in the sensory model to account for the measured inaccuracies in the form of white noise. Since these measurements are typically filtered with a Kalman filter, this block feedbacks the flight states with filtered white noise.

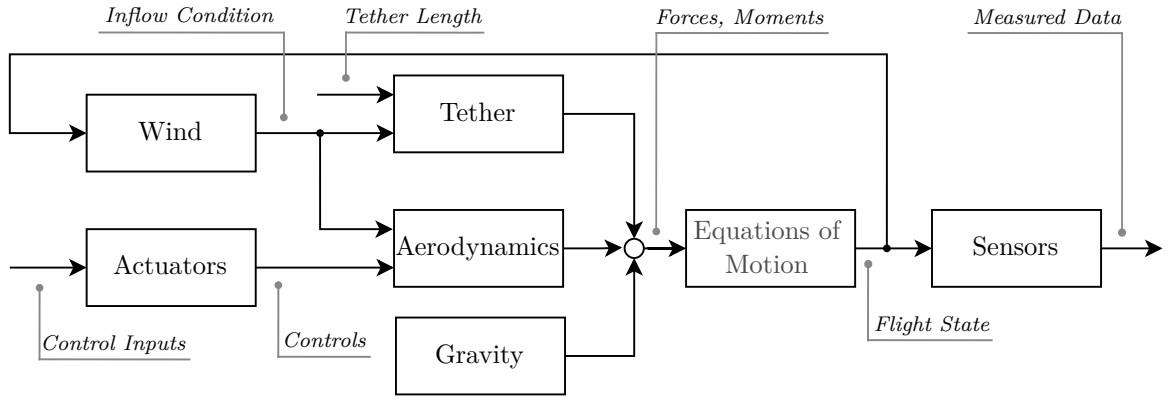


Figure 2.4.: Structure of the flight model, compare with [89].

$$\vec{x}_{\text{motion}} = \left[\vec{s}^{\,\text{g}}_{\text{b}}, \vec{V}^{\,\text{b}}_{\text{G}}, \vec{\omega}^{\,\text{b}}_{\text{b}}, \underline{\Phi}_{zyx}\right]^{\top} \in \mathbb{R}^{12,1} \tag{2.8}$$

The forces and moments arise from a superposition: weight, aerodynamic forces and moments, and the tether force. It is assumed that the winch is positioned at the origin

of the geodetic coordinate system and the tether length as input for the tether model is kept constant. The aerodynamic and tether models both require the current, aerodynamic velocity of the flight system, which results from the flight system's ground velocity of the equations of motion minus the wind velocity. Both models are described in the following sections in detail.

Wind modeling is a relevant quantity within the AWE application. Due to the focus of this thesis on the transition procedure at low heights, a constant wind profile over height is assumed. The horizontal wind profile is defined by the wind velocity $\vec{V}_\mathrm{W}$ and the wind direction Ψ_w. It consists of a superposition of a low-frequency, averaged wind velocity $\overline{V}_\mathrm{W}$ and wind direction $\overline{\Psi}_\mathrm{W}$ with high-frequency turbulence. Expected values and standard deviation for the averaged wind velocity and wind direction from [89, 90] are utilized and combined with white noise for turbulence.

The actuator model describes the transfer function of the control inputs to the actual elevon deflection and propeller thrust. A first-order lag element with delay is implemented, based on the specifications of the manufacturer and test bench results. The control input for the propeller thrust is the throttle, a normalized value between zero and one. A correction value based on the battery voltage is added to account for the reduced performance of a low battery.

2.4.2. Tether Model

The tether model calculates the tether forces acting on the flight system in vectorial form. The tether is assumed to be attached in the CoG, such that no moment is induced by the tether force. Depending on the model accuracy and computational effort, there are a wide range of different tether model concepts: A rod model that calculates exclusively the tensile forces of a stretched tether, a catenary curve model that considers a symmetrical sagging of the tether, models that solve differential equations to model asymmetrical loads, and dynamic models such as finite element methods (FEM). A detailed comparison of these models can be found in [91]. In the scope of this thesis, a catenary curve to model the drag, weight and lift forces of the tether combined with the tensile forces of the rod model is implemented. During the transition, the tether forces, tether length, and flight velocities are relatively small compared to crosswind flight, allowing asymmetrical effects to be neglected. Therefore, a static approach is considered sufficiently accurate and can be solved analytically. Rod and catenary curve models are briefly introduced in the following. An illustration of the curvature, inflow condition, and the tether forces for both models is depicted in Fig. 2.5.

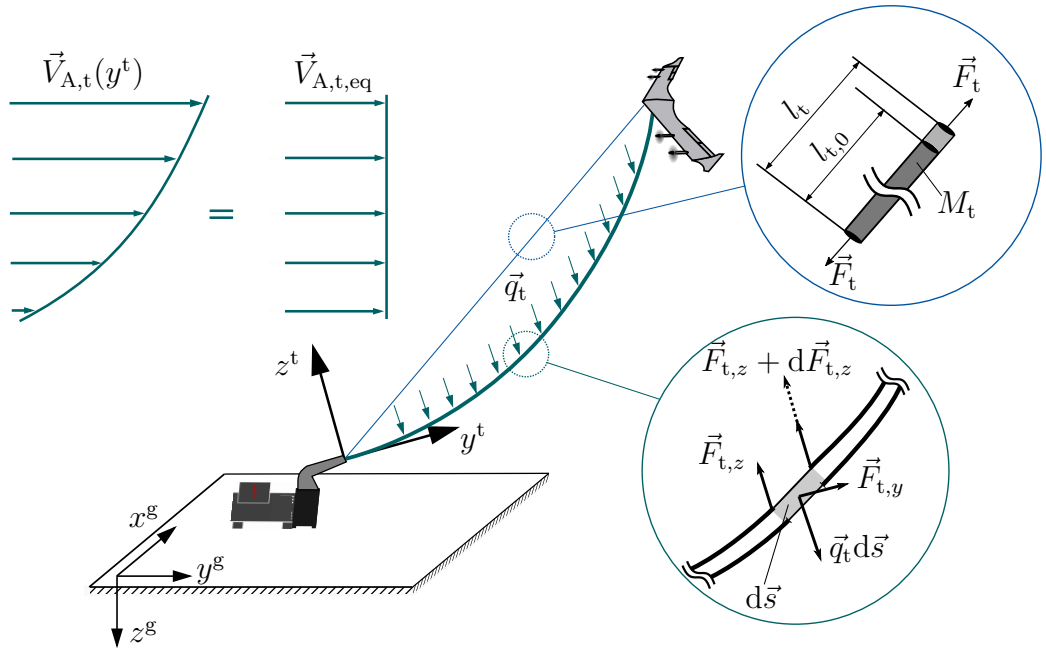


Figure 2.5.: Representation of the tether model as a combination of a rod model and a catenary-based model.

The rod model neglects any sagging of the tether and calculates the tensile forces for a stretched tether under the assumptions of a homogeneous relative stiffness distribution M_{t}, a circular and constant cross-section and a constant normal directed tensile force. The tether force F_{t} is derived from Hooke's law [92] based on the relation between the stretched tether length l_{t} and the unstretched tether length $l_{\mathrm{t,0}}$, according to Eq. 2.9. The stretched tether length is a direct result of the difference in position between the winch and the flight system.

$$F_{\mathrm{t}} = M_{\mathrm{t}} \frac{l_{\mathrm{t}} - l_{\mathrm{t,0}}}{l_{\mathrm{t,0}}} \tag{2.9}$$

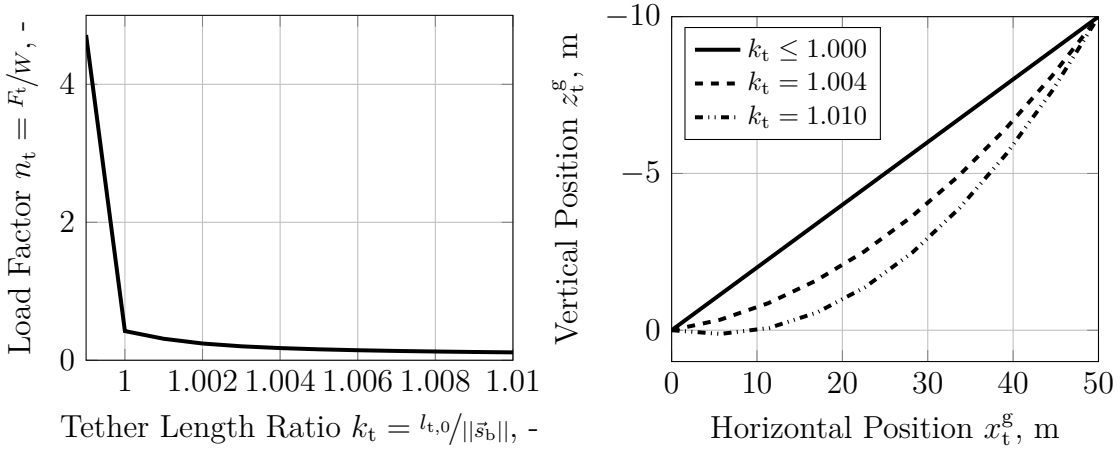
The catenary model is based on the general catenary curve to describe the shape of a hanging chain [93] and has been adapted and applied within AWE for the calculation of tether sag and tether forces [94]. The model assumes a constant line load q_{t} over the tether length with no transverse shear, no bending stiffness and no ground contact of the tether, compare with Fig. 2.5. The acting forces F_{t} resulting from drag, lift and gravity of the tether are reduced to an equivalent line load. The aerodynamic velocity of the tether results from the superposition of the ground velocity of the tether minus the wind velocity. The velocity of the tether on the ground is zero and is equal to the velocity of the flight system at the top. According to [94], an equivalent aerodynamic velocity $V_{\mathrm{A,t,eq}}$ of the

tether is calculated to solve for the resulting line load q_t. Based on the equilibrium of forces at an infinitesimal element $\mathrm{d}\vec{s}$, the differential equation for the catenary function can be derived, see Eq. 2.10. Its derivation and the solution for the tether curvature and the tether forces can be found in [91, 94].

$$q_\mathrm{t}\sqrt{1+\left(\frac{\mathrm{d}z^\mathrm{t}}{\mathrm{d}y^\mathrm{t}}\right)^2} = F_{\mathrm{t},y}\frac{\mathrm{d}^2 z^\mathrm{t}}{\mathrm{d}{y^\mathrm{t}}^2} \tag{2.10}$$

The rod model and the catenary-based model are combined in a hybrid model to account for both the tensile forces and the line load. It is compared in [95] with an FEM simulation showing compliance with tether forces and sagging with reasonable deviations for inflow conditions with asymmetric line loads. The table of the relevant tether data utilized in this thesis is given in Appendix B.

In the following, an exemplary flight state is considered within the transition with a high aerodynamic velocity in order to be able to classify the magnitude of the acting tether forces. For an aerodynamic velocity of the flight system of 20 m/s and a position of the flight system at 10 m height and 50 m distance to the winch, Fig. 2.6 shows the results of the tether forces and the tether sagging. The load factor $n_\mathrm{t} = {}^{F_\mathrm{t}}/_{W}$ is introduced to refer to a normed value of tether force to weight. The tether length is given in the tether length ratio as $k_\mathrm{t} = {}^{l_{\mathrm{t},0}}/_{||\vec{s}_\mathrm{b}||}$, such that a ratio $k_\mathrm{t} < 1$ defines a stretched tether. For this scenario, the tether weight corresponds to a load factor of 0.04.



(a) Course of the load factor.

(b) Tether curvature.

Figure 2.6.: Tether forces and tether sagging for an exemplary flight state, based on [95].

Figure 2.6a shows the ratio of load factor to tether length and Fig. 2.6b the tether curvature for selected tether length ratios. For a high tether length ratio, the tether is bent in the load direction and the tether forces are small with a load factor of $n_\mathrm{t} \approx 0.1$. Since only the near range around k_t is considered, an increase in tether weight for higher tether length ratios is not reflected in the data for this range. Following the curve to smaller tether length ratios, the tether sagging decreases and the tether force increases. The reason is that the tether can only absorb forces in the longitudinal direction. For tethers that are less bent in the direction of the loading, the amount of lateral forces on the tether line increases, which is compensated by an increased total tether force. At $k_\mathrm{t} < 1$, the tether is being stretched and the tensile forces dominate the course of the load factor, leading to a strong increase of the load factor.

2.4.3. Aerodynamic Model including high Aerodynamic Angles

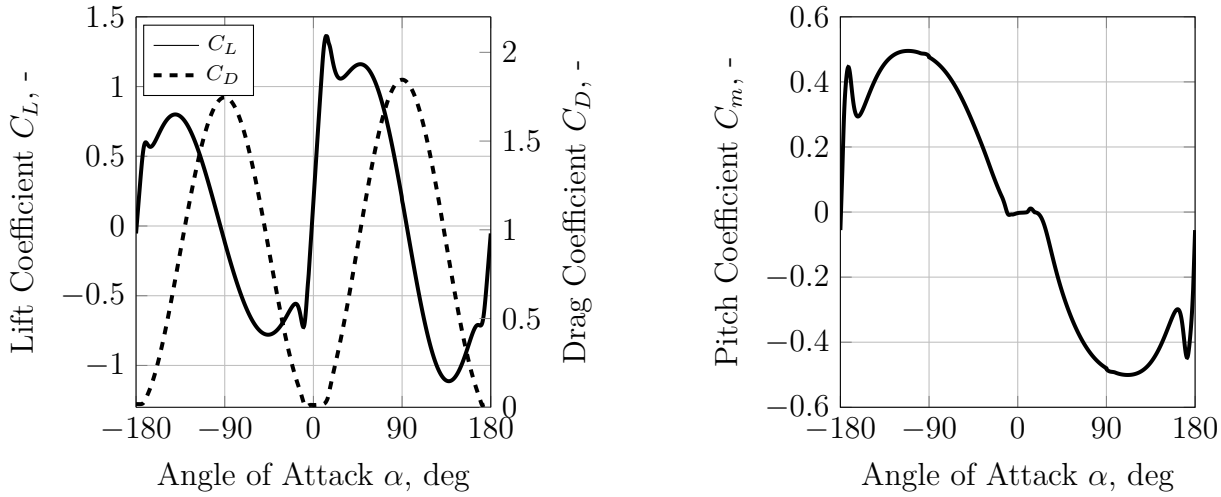
The aerodynamic model computes the forces and moments based on actuator controls and the inflow condition. A sufficiently accurate model is implemented that accounts for aerodynamic forces of the wing including the influence of elevon deflection and propeller, without relying on a high fidelity computational fluid dynamic (CFD) analysis. In the following, the aerodynamic model is explained in detail, with a special emphasis on the characteristics at high angles of attack and slip angles occuring during the transition. Subsequently, the aerodynamic model is verified using a simplified flight system.

Based on [89], a component-based model (CBM) is implemented which divides the wing into a distinct number of elements with similar aerodynamic characteristics. A component can consist of a wing, a propeller and/or an elevon element. The wing element is characterized by the wing area and the mean aerodynamic chord length, as well as the aerodynamic center at which the forces and moments act, based on a stored 2D polar. This polar is further influenced by an elevon deflection, shifting the polar to higher or lower angles of attack. An additional propeller element increases the inflow condition of the wing element in the slipstream. Depending on the inflow condition, control inputs, and element definitions with their 2D polars, the aerodynamic forces and moments are calculated for each element based on analytical and semi-empirical formulas. They are superpositioned in the CoG of the flight system with reduction factors to account for 3D effects due to the limited aspect ratio of the wing.

The main design inputs of the aerodynamic model are the element definitions based on wing geometry and sideslip, and the 2D polars, extrapolated to high angles of attack. The specific characteristics are outlined below.

2.4.3.1. Polar Extrapolation to high Angles of Attack

To calculate the 2D aerodynamics of the wing elements, the polar for lift, drag and moment coefficients are generated utilizing the software tool *xfoil*. The software solves the Laplace equation for an inviscid, irrotational and incompressible 2D flow using the panel method, which represents the airfoil as a superposition of sources and sinks as elementary flow elements. In combination with the 1D boundary layer equations to account for viscous effects, it allows solving for the aerodynamic forces and moments, and shows convergence in the region of low angles of attack including the indication of the region of stall [96]. However, during vertical flight and transition, a horizontal aerodynamic inflow can lead to high angles of attack exceeding 90°. In this region, the polar resembles aerodynamics of a flat plate. Montgomerie [84] therefore proposes an extrapolation method between the polar of the airfoil and the polar of a flat plate to model the full flight envelope with angles of attack ranging from $\alpha \in [-180°, 180°]$. The method does not claim high accuracy for high angles of attack but shows correct tendencies in this range.



(a) Lift and drag coefficient.

(b) Pitch moment coefficient.

Figure 2.7.: Polar of the airfoil, extrapolated to ±180°.

Figure 2.7 shows the resulting polar of the flight system's airfoil at $Re = 300,000$. The lift coefficient has its linear slope at low angles of attack from around -10° to 12.5°. Following the typical decrease in lift due to stall, the lift coefficient then resembles the curve of a flat plate. In the linear range at low angles of attack, the drag coefficient is minimal, but increases above stall. The pitch moment coefficient in Fig. 2.7b remains widely constant and close to zero in the region of low angles of attack. However, at higher negative and

positive angles of attack when stall effects occur, the pitch moment increases significantly. The reason for this is the increased drag and the shift of the AC. Figure 2.8 depicts the characteristic course of the position of the AC relative to the wing chord length, following [84]. Note that the aerodynamic center is typically defined as the point at which the pitch moment coefficient does not vary with changes in lift. Since this is only valid at low angles of attack, Montgomerie introduced a work parameter called "arm" to describe the position of the shifting center of pressure of the flat plate at higher angles of attack. For simplicity, this is still referred to as AC in this thesis. At low angles of attack, the AC remains constant at the prominent 25 % chord-line [85]. Outside of this range, the position of the AC initially increases significantly and approaches the center of the wing at $\alpha = 90°$ with an AC ratio of 50 %. Therefore, the lever arm of the aerodynamic forces is larger compared to small angles of attack. As a result, the pitch moment coefficient, which is defined around the 25 % chord line, increases. Considering negative angles of attack, the course of the AC ratio is symmetrical to the y-axis with a shift of the zero angle of attack (α_0). For a small zero angle of attack of 1.5° of the AWE system, the course of the pitch moment coefficient is therefore widely similar for negative and positive angles of attack.

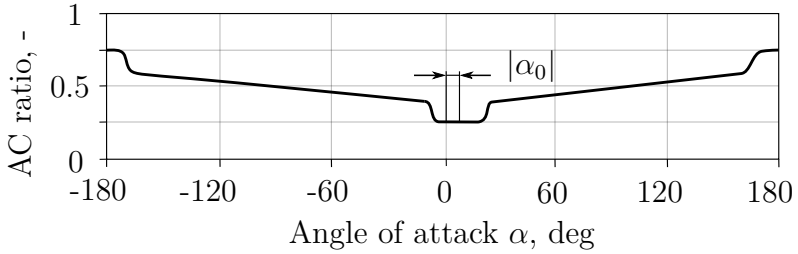


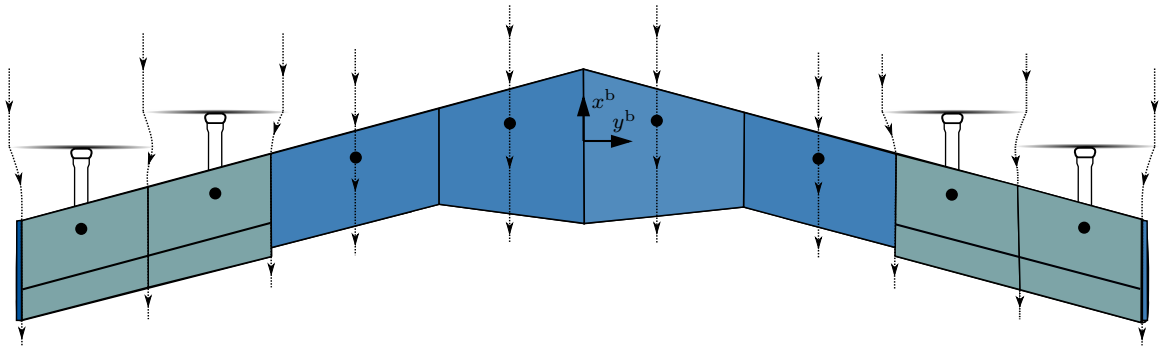
Figure 2.8.: Sketch of the lever arm of the aerodynamic center, following [84].

2.4.3.2. Element Definition with Sideslip

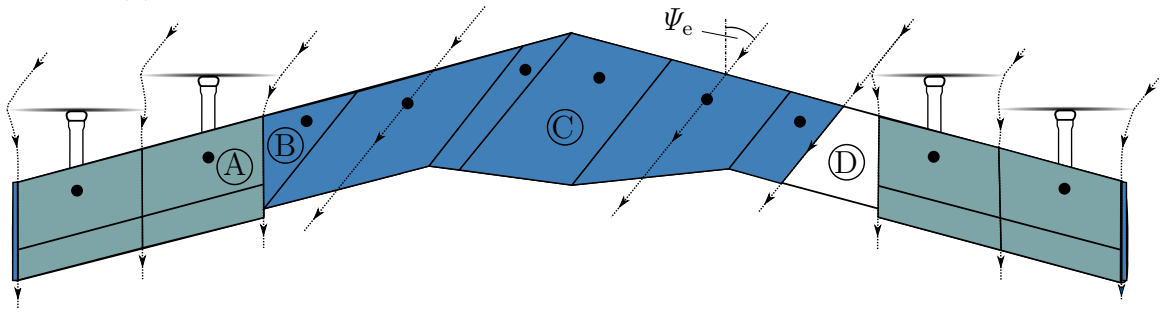
In addition to high angles of attack, the flight range of the flying wing during transition further includes high slip angles ranging from -90° to 90°. An inflow with sideslip modifies the aerodynamic coefficients of the longitudinal direction, and additionally introduces forces and moments in the lateral direction. It therefore influences flight mechanics and stability, compare with Section 2.3. In [97], a detailed description of the methodology to model aerodynamics with sideslip is given, which preserves the component-based notation. The main characteristics of the element definitions are outlined in the following.

Figure 2.9a depicts the elements of the flying wing of the CBM for an aerodynamic inflow with no sideslip ($\beta = 0°$). The flight system is divided into solely trapezoidal elements with no curves as simplification. The center segment consists of four mere wing elements while

the outer part is divided on both sides into two elements consisting of wing, propeller, and elevon components. The contraction of the aerodynamic inflow behind the propellers is indicated in the figure but not depicted in the element definitions for visualization reasons. The winglets are modeled with one mere wing element on each side, rotated by 90° around the x^{b}-axis. The corresponding aerodynamic center, assumed to be at 25 % of the mean aerodynamic chord length of each element, is indicated with a dot.



(a) Element definitions of the CBM of the flight system with no sideslip.



(b) Element definitions of the CBM of the flight system with an element rotation of $\Psi_{\mathrm{e}} = 45°$.

Figure 2.9.: Element definitions of the CBM of the flight system for two exemplary inflow conditions.

For an aerodynamic inflow with sideslip, the elements are rotated around the z^{b}-axis to point in the inflow direction. Due to the rotation order of the aerodynamic angles $(-\beta, \alpha)$, this angle is equal to the slip angle only within the range of small angles of attack. For higher angles of attack, the z-rotation axes of the aerodynamic and body coordinate systems are not collinear, leading to different rotations. Therefore, a post-rotation angle Ψ_{e} around the z^{b}-axis is applied such that the elements are rotated until they are aligned in the direction of the inflow having no sideslip. Note that Ψ_{e} does not correspond to a rotation from the geodetic to the body coordinate system according to the ISO norm [98], but to a rotation only applied for computational purposes. The rotation from the geodetic system to the wing elements therefore consists of a 'ZYXZ'-rotation sequence, with Ψ_{e} as the last rotation angle. This rotation allows the application of 2D polars to each element

as a function of the angle of attack only. To illustrate this relationship, consider a single, mere wing element experiencing an aerodynamic inflow with $\alpha = \beta = 90°$. By rotating the wing element around its z^{b}-axis with an angle of $\Psi_{\mathrm{e}} = 90°$, both aerodynamic angles of the relative aerodynamic inflow become zero ($\alpha = \beta = 0°$). Without a sideslip, the polar of the longitudinal motion can be applied accordingly. In this scenario, the rotation results in an additional aerodynamic bank angle of 90° of the element, which only defines the direction of the aerodynamic forces, but does not affect the polar.

The rotation of the elements due to sideslip requires a dynamic adaption of the element definitions. Based on the current aerodynamic inflow condition, the required rotation angle Ψ_{e} is calculated to define the wing elements. Figure 2.9b depicts a sketch of the elements for an exemplary element rotation angle of $\Psi_{\mathrm{e}} = 45°$. The wing is divided into elements with similar aerodynamic characteristics (see the marked areas A-D) under the following assumptions and simplifications:

(A) The propeller straightens the inflow, leading to unmodified elements at the outer part of the wing. Following [18], the aerodynamic velocity in the slipstream of the propeller is accelerated to around $20\,\mathrm{m/s}$ for the given geometry. Within the transition of the flight system, ranging from $0 - 15\,\mathrm{m/s}$, it is therefore assumed to be the dominant flow direction and a lateral rotation is neglected.

(B) The inflow that first crosses a mere wing element and then an element in the propeller slipstream is straightened when it reaches the slipstream. This results in a triangular shape of the elements.

(C) The mere wing is separated into several trapezoidal elements depending on the intersections of the streamline, leading edge and trailing edge.

(D) The mere wing element that is shadowed by the propeller slipstream does not contribute to aerodynamics.

The calculations for wing area, mean aerodynamic chord and aerodynamic center of the trapezoidal and triangular elements are given in [97]. Next to the element definitions, the 2D-polars must be adjusted based on the rotation angle Ψ_{e} and the chord length of the rotated element. Since the streamline follows a longer path on the wing element with increasing slip angle, the relative airfoil thickness and camber decrease. Figure 2.10 depicts the relative airfoil coordinates for selected Ψ_{e} under the assumption of a wing with a constant chord length l_{c}. Ranging from the original airfoil coordinates at $\Psi_{\mathrm{e}} = 0°$, thickness and camber decrease until the profile resembles a flat plate at $\Psi_{\mathrm{e}} = 90°$. Regarding airfoil

twist, the twist at the leading edge is considered to be fixed for the wing element and does not affect the course of the airfoil coordinates. Similarly, the airfoil coordinates of the streamline that crosses the x^{b}-symmetry line of the flight system are not further modified. For the adjusted airfoils, *xfoil* solves for the 2D polars, and the aerodynamic forces and moments can be calculated based on the element definitions of the CBM.

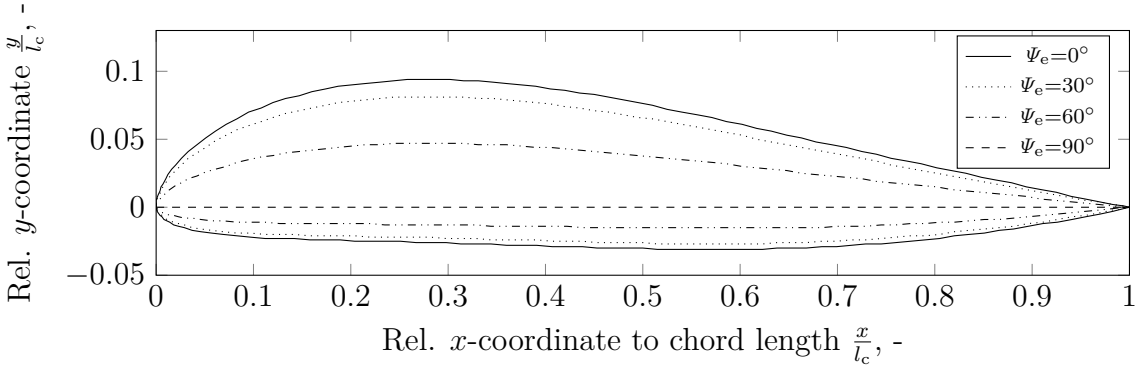


Figure 2.10.: Relative airfoil coordinates for different Ψ_{e} under the assumption of a wing with a constant chord length.

2.4.3.3. Verification of the Aerodynamic Model

In the following, the aerodynamic model is verified for a simplified, swept wing with a constant chord length of 0.2 m, a sweep of 20°, a span of 1 m, and with no elevon or propeller influence. The inflow condition is set to $Re = 300,000$. For this simplified flight system, the software tool *xflr5* allows calculating the 3D aerodynamic forces and moment coefficients for comparison with the results of the CBM. *xflr5* integrates among others the vortex lattice method (VLM) and therefore presents an independent verification tool for the aerodynamic model.

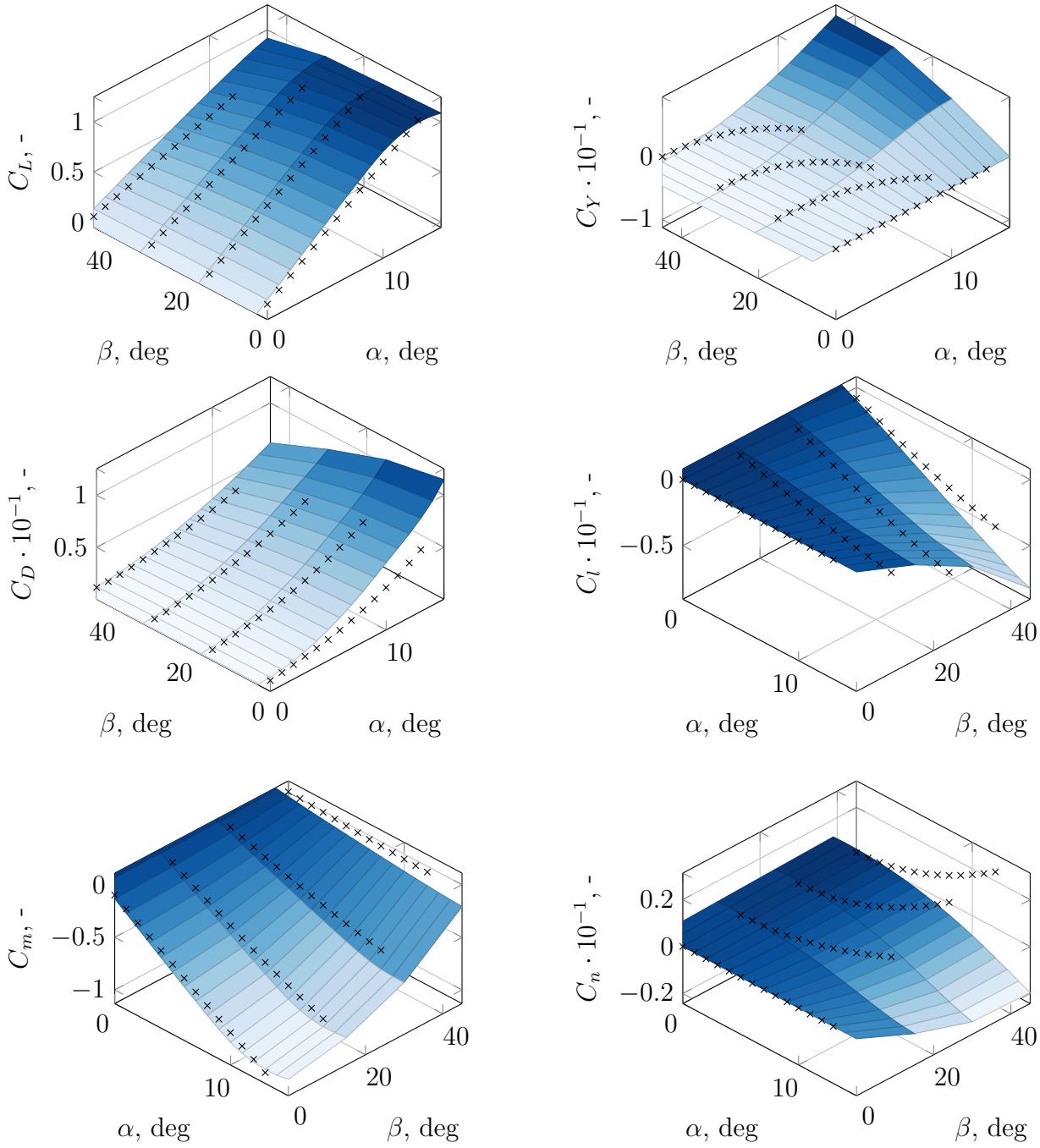
Within the framework of *xflr5*, the wing is discretized by a set of horseshoe vortices. The wing is assumed to be infinitesimally thin and non-viscous, yet induced drag can still be modeled. Thickness and camber of the airfoil are integrated into the boundary conditions. Sideslip is modeled by rotating the body around its z^{b}-axis. The integrated method uses a small angle of attack approximation for the wake definition, so that the horseshoe vortex is aligned with the plane of the x^{b}-y^{b}-axes. This simplifies the calculation but leads to deviations at higher angles of attack. The aerodynamic forces act within the x^{b}-y^{b}-plane rather than along the axes of the aerodynamic coordinate system. The vortex lattice method is verified with a 3D panel method and wind tunnel experiments, showing agreement with the aerodynamic coefficients except for drag, which is underestimated due

to the lack of viscosity. Note that the verification of *xflr5* is conducted with a conventional flight system including a vertical stabilizer, which reduces the representativity of the lateral coefficients for an aerodynamic inflow with sideslip for the mere wing. Nevertheless, the software tool represents a further, independent method to calculate the aerodynamic forces. [99, 100, 101]

Figure 2.11 depicts the aerodynamic coefficients of the simplified wing for varying angles of attack and slip angles. The surface plot shows the coefficients of the CBM verified with selected points of the vortex lattice method. Since VLM does not model viscous effects, stall effects are not visible and the points are limited to the region of angles of attack until stall. The coefficients of the longitudinal motion are given in the aerodynamic coordinate system, with C_L and C_D pointing in the opposite direction of the z^{a}- and x^{a}-axes respectively. The coefficients of the lateral motion (lateral force C_Y, roll moment C_l and yaw moment C_n) are set in the body coordinate system. The reference length for the pitch moment coefficient C_m is the mean aerodynamic chord, while the lateral coefficients are referenced to the span width. Note the alternating axes of the angle of attack and sideslip in the different subfigures for visualization purposes.

For the coefficients of the longitudinal motion, as shown in Fig. 2.11a, the CBM and VLM results generally show good agreement. At zero slip angle, the lift and drag coefficients increase with a rising angle of attack, while the pitch moment coefficient decreases. However, a consistent discrepancy is observed in the drag coefficient, which is lower in the VLM compared to the CBM. This difference arises because the VLM does not account for viscous effects, whereas the CBM incorporates them within the 2D polar. When examining the results for increasing sideslip, both the CBM and VLM show a general reduction in the absolute values of lift, drag, and pitch moment coefficients. This reduction is attributed to the decrease in relative airfoil thickness and camber, leading to smaller pressure gradients and, consequently, reduced forces and moments. The effect is more pronounced in the VLM, resulting in a sharper decrease in the lift coefficient at higher sideslip angles and therefore slight deviations between the models at large slip angles and angles of attack.

The coefficients of the lateral motion can be identified in Fig. 2.11b. At zero slip angle, all lateral coefficients are zero since the forces are aligned with the x^{b}-z^{b}-plane. As the slip angle increases, a negative roll moment coefficient C_l develops due to the sideways shift of the center of pressure in the inflow direction, resulting in a growing negative roll moment driven by the lift force in both CBM and VLM. Since lift increases with the angle of attack, the roll moment coefficient increases accordingly. However, the comparison between the CBM and VLM models reveals that the magnitude of this increase differs. At lower slip



(a) Coefficients of the longitudinal motion.

(b) Coefficients of the lateral motion.

Figure 2.11.: Verification of the aerodynamic coefficients for varying angles of attack and sidelip angles.

angles, the CBM predicts lower absolute values of the roll moment compared to the VLM. At higher slip angles, this relationship reverses, with the VLM showing lower absolute values. As the reduction in lift of the longitudinal motion with increasing sideslip is more

pronounced, this leads to a correspondingly smaller absolute roll moment at higher slip angles in the VLM than in the CBM.

Considering the coefficients of the lateral force C_Y and the yaw moment C_n, the results of CBM and VLM show agreement only at low angles of attack. At low angles of attack, the lateral component of drag due to sideslip is the primary contributor to a negative lateral force C_Y. Because the center of pressure of the swept wing is located behind the center of gravity, this negative lateral force corresponds to a positive yaw moment. As sideslip and the angle of attack increase, drag increases, leading to an increase in the lateral force coefficient and yaw moment in the VLM. However, as the angle of attack and sideslip increase, the results diverge. This discrepancy arises from the simplified calculation of the lift coefficient in the VLM. The wing is rotated only around the z^{b}-axis to model sideslip, causing lift to act along the z^{b}-axis regardless of the angle of attack. Since the lift force actually acts perpendicular to the aerodynamic inflow, it tilts out of the x^{b}-,$z^{\mathrm{b}}-$ plane of the wing surface for increasing angle of attack and contributes to the lateral forces and yaw moments in the opposite direction. As VLM does not account for this effect, the absolute value of the lateral force and yaw moment increases monotonously, while the course of the CBM changes its sign with increasing angle of attack. The lift components dominate the course in this region and induce a positive yaw moment. Due to the simplification of the calculation of the aerodynamic forces within the scope of the VLM, the coefficients C_l and C_n cannot be accurately verified at high angles of attack and slip angles.

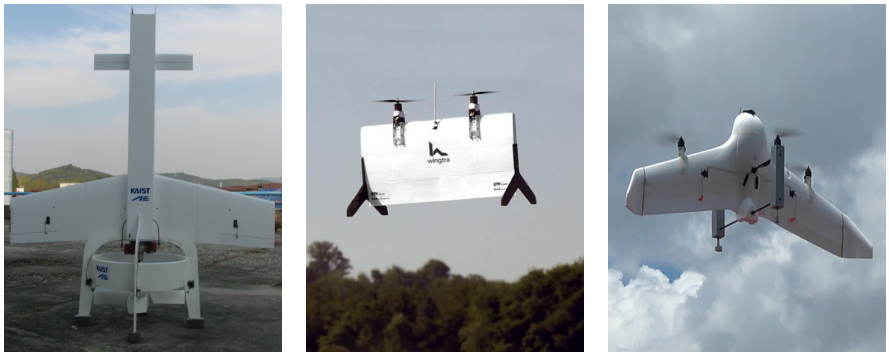
For verification of the correct course of the coefficients C_l and C_n, literature data is used for reference. In [102], wind tunnel tests including sideslip are performed for a blended wing body with a wing span of 1.5 m. The data demonstrate a similar trend to the CBM results and can be found in Appendix B. For an aerodynamic inflow with sideslip, the lateral force is negative at low angles of attack but changes its sign as lift forces become dominant in this direction. At angles of attack above stall, this relation is again reversed, as drag increases significantly and dominates the lateral force. The analogous effect is identified in the yaw moment coefficient. All in all, the CBM is therefore evaluated to be adequate to model the correct effects of an aerodynamic inflow including sideslip. Calculation details and the verification of the 2D polar can be found in [97].

3. Trajectory Concepts of Tailsitter Flight Systems

Tailsitters describe the class of flight systems that take off vertically on their tails and then rotate entirely to achieve wing-borne flight. The trajectory and control concepts implemented for the transition are widely similar across different tailsitter designs. In the following, the state-of-the-art tailsitter flight systems is outlined, focusing on various flight system configurations and the associated transition trajectories and control techniques. This contributes to the limited literature on the transition of flying wings within the context of AWE applications. The AWE system described in Section 1.1.1 belongs to a minimalistic subset of tailsitters, characterized by reduced drag. Given its unique flight characteristics, the particularities of the longitudinal motion are described in detail in the subsequent section.

3.1. Tailsitter - State-of-the-Art

Tailsitter flight systems were first introduced in the 1950s as manned aircraft, before being adopted in the development of tactical UAVs. According to Saeed et al. [20], a classification can be made into flight systems with mono thrust transitioning (MTT), collective thrust transitioning (CTT) or differential thrust transitioning (DTT) concepts, as shown in Fig. 3.1. For each transition concept, a characteristic flight system is utilized, which differs mainly in the propeller positioning.



(a) MTT [103]. (b) CTT [104]. (c) DTT [105].

Figure 3.1.: Tailsitter concepts with different transition strategies. (*Note: Cropped images*)

MTT tailsitter use a single rotor positioned either at the rear or front of the flight system. The roll moment of the rotor is counteracted by stators behind the propellers [106] or small rotors at the wing tips [107]. Handling is accomplished by vectored thrust or blade pitch control combined with aerodynamic control surfaces such as ailerons or canards. The transition can be accomplished by a stall-and-tumble maneuver, as proposed in Stone et al. [108]. The flight system accelerates to a certain height in an upright position, followed by a rapid downward pitch motion leading to a tumble. The flight system descends until it reaches wing-borne flight. Due to the highly nonlinear flight dynamics and height loss, research has focused on optimizing the control and transition paths to achieve a continuous transition with minimal height variation and transition time [109, 110].

CTT tailsitter typically include additional propellers aligned with the leading edge of the wing. The roll moment generated by the rotating propellers is balanced by a counter-rotating arrangement of the propellers. During prop-borne flight, the yaw moment around the z^{b}-axis is induced by differential thrust, while the pitch and roll moments are induced by the elevons in the propeller downwash. However, pitch authority is limited, since the lever arm of the elevons in the x^{b}-direction is small and the aerodynamic inflow is reduced compared to wing-borne flight [111, 39]. As a result, some applications integrate classical elevators or canards [112, 113, 114], extend the elevons over the entire width of the wing [115, 116] or extend them in length [117]. The transition is typically performed by a longitudinal pitch motion, either via upward acceleration [118, 112] or at constant height [119]. Significant challenges arise during the transition at a constant height, as the angle of attack changes from high values in prop-borne flight to low angles in wing-borne flight. The occurring stall effects lead to oscillations and attitude loss, as observed in [104, 113, 120]. The transition from wing-borne back to prop-borne flight is performed slowly to decrease the horizontal velocity. Otherwise, the flight system still has a significant residual horizontal velocity when reaching its vertical attitude, leading to down-pitch moments and oscillations [121, 104, 120].

To manage the changes in aerodynamic characteristics during the transition, different control strategies are utilized. A switching logic between prop-borne and wing-borne flight is implemented for maneuvering between the operating points [120, 122], or LQR gain scheduling methods are used to track a defined reference trajectory [123, 121]. In Kubo et al. [124], a trim analysis is conducted to optimize for the minimum flight path angle to avoid stall effects. In [125], an incremental nonlinear dynamic inversion (INDI) approach is proposed and compared with a nonlinear dynamic inversion controller, showing reduced loss of height during the transition. Longitudinal and lateral motion control are largely separated during these pitch transition maneuvers. Tal et al. [126] implemented

an approach based on differential flatness and INDI with coupled longitudinal and lateral motion. Various indoor aerobatic maneuvers are successfully performed for an agile CTT tailsitter, including uncoordinated flight with sideslip, lemniscates, and knife-edge flights.

DTT tailsitter feature propellers located above and below the horizontal plane of the flight system, allowing the control of all axes through differential thrust. Oosedo et al. [127] proposed a tailsitter design with no aerodynamic control surfaces at all. Compared to CTT tailsitter configurations, the DTT configuration significantly improves pitch authority during hover. However, this comes at the expense of a reduced roll moment around the x^{b}-axis, as the effectiveness of the reactional torque from differential thrust is limited. An emerging concern is the increased susceptibility to wind gusts during hover. To address this, inclined propellers are implemented in [128, 129] that sacrifice a certain amount of thrust to increase roll effectiveness. In Li et al. [105], one set of propellers is positioned in line with the wing, while another set is placed above and below the center to benefit from both roll and pitch authority of CTT and DTT designs. They implemented a model predictive control (MPC) approach for robust hovering with wind disturbance rejection. In general, the transition to wing-borne flight is controlled similarly to the CTT tailsitter and is accompanied by similar stall effects. However, due to the increased pitch authority, its impact is relatively diminished. In Hochstenbach et al. [128], the control system gradually decreases the pitch angle for the transition. Lyu et al. [129] control the height error during the transition with a proportional-integral-derivative controller (PID), while Oosedo et al. [130] perform an optimization for minimum transition time and minimum time at a constant height.

3.2. Longitudinal Motion of the AWE System

The flying wing of this thesis is in a CTT tailsitter configuration with propellers aligned with the wing, compare with Section 1.1.1. It provides sufficient roll control in prop-borne flight to account for a dynamic wind field. Both roll and pitch motions are aerodynamically controlled by the elevons and do not come at the expense of additional differential thrust. However, the main challenge of the flight system in the CTT configuration is the pitch control in prop-borne flight. Compared to the flight systems in the literature in Section 3.1, the AWE system has a significantly enlarged wing area to increase lift and achieve a high power output according to Eq. 1.2. This leads to a higher susceptibility to an aerodynamic inflow perpendicular to the wing area, which induces strong pitch moments. In addition, the AWE operation includes specifically strong wind velocities and the tether connection that must be considered in the design of the transition. Therefore, the flight envelope of the flight system and the boundary conditions differ. In the following, the main characteristics

of the flight envelope and the flight dynamics of the longitudinal motion of the AWE system are outlined and discussed. A detailed discussion including the derivation of the trim states of the longitudinal motion is given in [39, 38].

The longitudinal motion describes the motion in the x^{b}-z^{b}-plane. The flight system is assumed to be aligned with its wing to a quasi-static wind direction, such that the motion corresponds to the x^{w}-z^{w}-plane, compare with Fig. 2.1. The solution space is reduced to the relevant flight states, controls, and forces and moments of the stationary, longitudinal motion, see Tab. 3.1 and compare with Eq. 2.6. The controls of uniform thrust f and uniform elevon deflection κ allow the independent definition of the two longitudinal velocities, while the pitch angle is the result of the trim conditions to equalize the forces and moments. Since flight mechanics are influenced by aerodynamic velocities, the trim states are determined based on these velocities. Note that due to the pure longitudinal consideration, the lateral wind vector defines in this case only the orientation of the fixed, wind coordinate system, while a lateral aerodynamic velocity of the flight system is not considered. The tether is not considered to capture the mere flight mechanics of the flight system.

states	controls	trim conditions
$\begin{pmatrix} u_{\mathrm{a}}^{\mathrm{w}} \\ w_{\mathrm{a}}^{\mathrm{w}} \\ \Theta \end{pmatrix}$	$\begin{pmatrix} f \\ \kappa \end{pmatrix}$	$\begin{pmatrix} X \\ Z \\ M \end{pmatrix} = \vec{0}$

Table 3.1.: Variables and trim condition for the longitudinal pitch motion.

The flight envelope of trimmed states of the longitudinal motion is depicted in Fig. 3.2. For a set of longitudinal velocities $u_{\mathrm{a}}^{\mathrm{w}}$ and $w_{\mathrm{a}}^{\mathrm{w}}$, sampled in increments of $0.5\,\mathrm{m/s}$, the resulting pitch angle is calculated to trim the flight system's motion. Plotted are the trim states as a function of the pitch angle and the upward velocity $w_{\mathrm{a}}^{\mathrm{w}}$. The trim states that correspond to a fixed horizontal velocity $u_{\mathrm{a}}^{\mathrm{w}}$ are connected, such that isolines are obtained for each horizontal velocity, ranging from prop-borne flight ($u_{\mathrm{a}}^{\mathrm{w}} = 0\,\mathrm{m/s}$) to wing-borne flight ($u_{\mathrm{a}}^{\mathrm{w}} = 15\,\mathrm{m/s}$). The corresponding pitch angle varies from $\Theta \approx 90° - 0°$. For each trim state, the colored legend marks the corresponding absolute value of the elevon deflection angle. For each set of velocities that cannot be trimmed independently of the pitch angle, a cross of varying size shows the location of the flight state corresponding to the minimum pitch acceleration $\dot{q}$. This is the dominant acceleration in these flight states. For illustration purposes, the flight system's pitch attitude is pictured at three selected points during the transition (a-c).

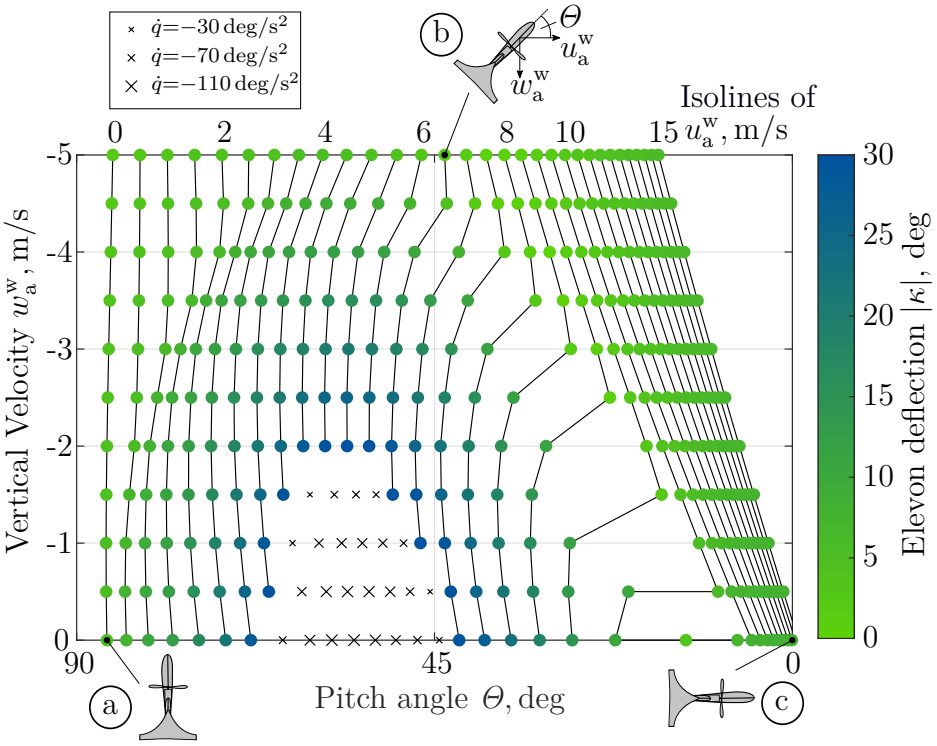


Figure 3.2.: Flight envelope of the longitudinal motion.

At velocities $u_a^w = w_a^w = 0\,\mathrm{m/s}$, the flight system hovers in prop-borne flight and maintains an upward attitude of around 90°, (a). As the horizontal velocity increases, the pitch angle gradually decreases accordingly and the flight system transitions from the vertical to a horizontal attitude at $\Theta = 0°$ in wing-borne flight (b-c). Considering the trim states at high horizontal velocities in wing-borne flight, small adjustments of the pitch angle result in proportionally large changes in velocity. As the horizontal velocity decreases, the stall speed is reached at a velocity of about $10\,\mathrm{m/s}$. The trim states are spread out, and in the range of low upward velocities, a single pair of velocities can be trimmed by different pitch angles. This is the range, where stall effects occur. A further increase in pitch results in less lift, and conversely, the same trim velocity can be achieved by increased thrust at that higher pitch angle.

In the range of the horizontal velocity $u_a^w = 3 - 7\,\mathrm{m/s}$ and the vertical upward velocity $|w_a^w| = 0 - 2\,\mathrm{m/s}$, stationary, trimmed flight is not possible and a strong down-pitch acceleration occurs up to $-110\,°/s^2$. As the boundary of the flight envelope is approached from either wing-borne or prop-borne flight, the elevon deflection increases to counteract the pitch moment from the aerodynamic velocity and reaches its maximum at the boundary of the untrimmed range. In this untrimmed flight range, the flight system is in an upward attitude above 45°, such that the aerodynamic forces are acting at a high angle of attack.

Due to the aerodynamic center close to the centroid of the wing and a correspondingly high pitch coefficient at high angles of attack (compare with Section. 2.4.3), the aerodynamic velocity leads to significantly high pitch moments. At the same time, the pitch authority of the elevons is reduced, since their lever arm to the center of gravity is small, while the aerodynamic inflow of the elevons in prop-borne flight is reduced compared to wing-borne flight. As a result, the flight states cannot be trimmed and the flight envelope of the longitudinal motion is limited in this region.

Achieving robust flight operations in the region of untrimmed flight states is challenging due to the strong down-pitch acceleration. While an unsteady, accelerating down-pitch motion can facilitate rapid transition to wing-borne flight, returning from wing-borne to prop-borne flight requires a high forward velocity and upward pitch acceleration to traverse the untrimmed flight range. Height and thrust demand increase significantly during this maneuver, and stall effects occur. Once in prop-borne flight, reducing the high aerodynamic velocity depends solely on the system's drag. However, in the upright attitude with its limited flight envelope, this drag induces strong down-pitching moments, potentially leading again to unsteady flight conditions. This makes it difficult to maintain the desired pitch attitude and poses significant challenges for practical flight testing.

Untrimmed flight states can be avoided by following a trim path with an upward velocity around $w_{\mathrm{a}}^{\mathrm{w}} = -5\,\mathrm{m/s}$. By gradually increasing or decreasing the horizontal velocity, the aerodynamic inflow perpendicular to the wing area and the elevon deflection remain low during both down-pitch and up-pitch maneuvers. However, this approach results in longer flight time, higher thrust demand, and increased height. A subsequent landing maneuver must be operated with low downward velocities, as the reversed aerodynamic inflow further reduces elevon effectiveness. Consequently, as height increases, the overall flight time and power consumption during the launching and landing phases increase significantly.

The aerodynamic velocity of the trim states generally results from the superposition of ground and wind velocity. If the flight system's wing is positioned perpendicular to the wind direction during takeoff, a strong wind velocity directly causes untrimmed flight conditions. When the wing is aligned with the wind direction, the wind velocity is oriented perpendicular to the ground velocity for stationary, longitudinal transition. However, the wind contributes minimal to aerodynamic velocity for wing-borne flight and does not support a rapid transition.

Flight dynamics vary strongly from prop-borne to wing-borne flight. Figure 3.3 depicts the pole-zero plot of the longitudinal motion for the linearization of two exemplary, trimmed flight states in prop-borne flight at $V_A = 0\,\mathrm{m/s}$ and wing-borne flight at $V_A = 10\,\mathrm{m/s}$, with

no vertical velocity $w_{\mathrm{a}}^{\mathrm{w}}$. It is linearized in the body-coordinate system with the state vector $\vec{x} = \left[u_{\mathrm{a}}^{\mathrm{b}}, w_{\mathrm{a}}^{\mathrm{b}}, q, \Theta\right]^{\top}$. The zeros are given for the transfer function from the elevon deflection κ to the vertical body-velocity $w_{\mathrm{a}}^{\mathrm{b}}$, and are plotted in the range of $\Re(z) \in [-8, 8]\,\mathrm{s}^{-1}$.

In wing-borne flight, the basic flight dynamic modes of the low-frequency phugoid and the high-frequency short-period oscillation can be identified. In comparison, the frequency of the short-period in prop-borne flight is decreased, while the poles of the phugoid become purely real to non-oscillatory flight states. The pitch axis is naturally unstable in prop-borne flight, as explained in detail in Section 2.3.1, with a time to double amplitude of 0.23 s.

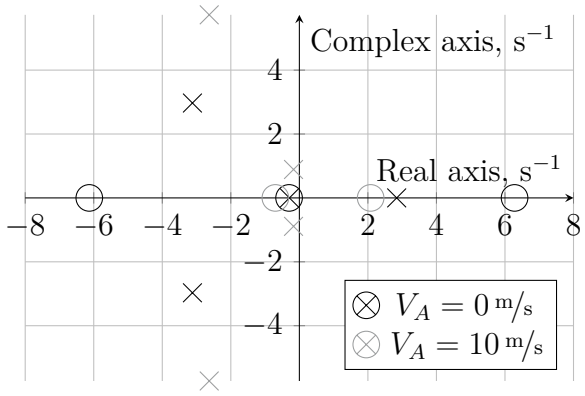


Figure 3.3.: Pole-zero plot of the longitudinal motion for two exemplary flight states.

A key characteristic of the system's zeros is the presence of a zero with a positive real part. This indicates that the transfer function of the elevon deflection to the aerodynamic velocity $w_{\mathrm{a}}^{\mathrm{b}}$ exhibits non-minimum phase behavior, which is most prominent in prop-borne flight. This aerodynamic velocity corresponds to the horizontal velocity $u_{\mathrm{a}}^{\mathrm{w}}$ in vertical flight. When a positive elevon deflection is initiated to induce a negative velocity $u_{\mathrm{a}}^{\mathrm{w}}$, the deflection modifies the flight system's lift. However, this initially generates an acceleration in the opposite direction. With a delay, the pitch angle increases and the corresponding thrust component eventually leads to the desired negative velocity. This non-minimum phase behavior makes sensitive control of the aerodynamic velocity $u_{\mathrm{a}}^{\mathrm{w}}$ in prop-borne flight challenging, supporting the difficulty of flight control of the longitudinal motion.

In the specific application of AWE, a robust transition maneuver is required with low power consumption, while considering the boundary condition of the wind and an additional disturbance by the tether. Given the outlined challenges regarding the limited flight envelope, instability, and non-minimum phase behavior, a transition relying solely on longitudinal motion is considered unsuitable for the AWE system. In [38], a lateral transition is outlined, which is discussed in detail in the following chapter.

4. Design of the Launch Trajectory Controller

This chapter outlines the design of the trajectory controller for the transition of the flying wing from vertical prop-borne to horizontal wing-borne flight. At first, the design objectives of the trajectory controller are explained in detail. Based on these requirements, a suitable launching concept for the AWE system is developed with respect to the tether connection and the wind direction. In addition to the longitudinal transition achieved by reducing the pitch angle, a flying wing allows for a lateral transition along the wind vector, primarily consisting of a coupled yaw-roll motion. To determine suitable operating points for this transition, the flight envelope of the lateral motion is examined regarding its trim states. A trim path is selected that satisfies the formulated design criteria. Subsequently, a control concept is proposed to enable precise control of the flight system along this designated trim path. The velocity controller is the core of the trajectory controller, which integrates the designed operating points. Its implementation is presented in detail.

4.1. Design Objective

The design objectives for the launch trajectory controller encompass the demands derived from the specific AWE system with its vertical takeoff capability regarding flight envelope, stationary flight, and the need for stability and robustness. Additionally, the AWE application imposes general requirements concerning power consumption and the boundary conditions of wind and tether. These objectives partially conflict and require a carefully balanced compromise in controller design.

Flight Envelope

The launch trajectory controller must handle a flight envelope which encompasses a wide range of flight velocities starting at low velocities in vertical flight to high velocities in wing-borne flight. The flight characteristics of these flight states are widely different. During prop-borne flight, thrust is the dominant force, while the lift forces are insignificant. The flight system is controlled by adjusting its attitude to induce a thrust component in the direction of the desired acceleration. In wing-borne flight, lift compensates for weight and thrust is reduced to balance drag. By adjusting the direction and magnitude of the lift force, the flight system can initiate accelerations in the related directions. During the

transition from prop-borne to wing-borne flight, a shift in these controls takes place and a corresponding control allocation is required to account for the varying control effectiveness regarding the different flight axes. Depending on the flight velocity and aerodynamic angles, the lift force increases. As the point of pressure shifts from prop-borne to wing-borne flight (compare with Section 2.4.3), this results in varying moments and stability margins during the transition.

The desired design shall incorporate an optimized flight trajectory specifically for the transition. The primary objective of this transition is to achieve sufficient aerodynamic velocity in wing-borne flight. This implies that for each wind velocity, there is a single, fixed trajectory optimized with respect to the design objectives of the flight system. This approach distinguishes it from conventional flight control designs, which must accommodate a wide range of velocities, flight directions, climb rates, or turning rates to perform various flight operations. As a result, this design task is well-suited for offline precalculation, enabling the determination of an optimal flight path and the implementation of a controller that accurately follows the predefined trajectory.

Wind Velocity

AWE systems generate maximum power in high wind conditions. Since this is the primary goal, one of the main objectives is to enable operation at the highest feasible wind velocity. Wind fields include gusts, which are amplified in high wind conditions. Since the effect of disturbances increase quadratically with wind velocity, it requires an effective disturbance rejection for flight control in a strong and dynamic wind field.

Typical power production curves define power output against wind velocity and specify next to the cut-out wind velocity, which is limited by structural loads due to overspeeding, the lower cut-in wind velocity required to generate sufficient lift for system operation [131]. The transition of the flight system should encompass the entire range of operable wind velocities along the power curve, including low velocities even below cut-in. This ensure that safe return and landing are possible under changing conditions and in the absence of wind.

Stability and Robustness

Attitude stability is an integral and necessary part of the flight controller to perform its task of controlling the transition of the flight system. As described in Section 2.3, prop-borne flight of a flying wing is characterized by increased natural instability. The flight controller must maintain sufficient stability margin for safe operation under conditions that deviate from the intended trajectory.

Achieving high robustness of the flight controller to model inaccuracies and external disturbances is a key design objective. As explained in detail in Section 1.1.2, a reliable transition strategy is crucial given the number of launches and the need for the system to land safely even in the case of a mulfunction. A general robustness to model uncertainties is required due to the simplifications inherent in the flight model, compare with Section 2.4. However, a primary focus is ensuring sufficient robustness to external disturbances, for example the tether forces or in particular the wind forces. The demand to operate in high wind conditions is directly linked to the need for robustness against strong gusts and a rotation of the main wind direction. This especially is of relevance in prop-borne flight, where the flight envelope for trimmed states of the longitudinal motion is narrow, and disturbances can generate significant pitch moments. It is crucial to ensure an operation within the trimmed flight envelope in prop-borne flight, even in the case of a rotation of the wind direction and gusts. For robustness in wing-borne flight, stall effects should be avoided. The highly nonlinear behavior of the system makes robust control challenging once the lift coefficient exceeds its linear range.

This thesis defines that the launch trajectory controller must be sufficiently robust to mitigate and stabilize disturbances of $\Delta u_a^{\mathrm{w}} = 3\,{}^{\mathrm{m}}/_{\mathrm{s}}$. This value corresponds to the upper limit of the stationary flight envelope with no upward velocity in the longitudinal motion and should therefore not be exceeded, compare with Fig. 3.2. Effective disturbance rejection keeps the disturbance within this threshold and maintains system stability up to this limit. Such aerodynamic inflow is for example caused by a sudden rotation of the main wind vector by 30° at a wind velocity of $V_W = 6\,{}^{\mathrm{m}}/_{\mathrm{s}}$.

Stationary Flight

The launch trajectory controller shall be capable of stationary flight. For precise takeoff and landing under wind conditions, stationary flight is a necessary prerequisite. Given that wind velocities can even exceed the flight system's stall speed, achieving trimmed flight states in the entire velocity range until wing-borne flight is a desired design goal. Besides, the demand for transition from prop-borne to wing-borne flight and vice versa requires the flight path to be feasible in both directions, such that trimmed flight states are a preferred criterion for the operating points. This does not preclude the possibility of unsteady transitions for faster operation. However, the design of the controller focuses on a stationary derivation of the controller's operating points in the scope of this thesis. This approach allows to derive linear stability and robustness characteristics of the designed trajectory controller in different wind conditions. This is beneficial for example with a focus on the certification process of the system. Besides, it simplifies flight testing, since

the velocity and acceleration during the transition can be gradually increased to verify the controlled system in each operating point. For a highly sensitive and unstable flight system, this is a decisive advantage.

Tether Connection

The tether connection represents a geometric constraint for flight operation. The transition should be conducted within a small operation radius to reduce tether length and weight. Besides, the tether forces have to be taken into account, which are sensitive to the tether length ratio or the flight position relative to the winch, respectively. Tether forces remain low when the tether is unstretched. However, when getting stretched, there is a discontinuity in the function of the tether force, resulting in a significant increase of the tether forces, compare with Section 2.4.2. A suitable launching concept must be selected that defines an adequate flight phase for tether stretching.

The flight controller must allow for both tethered and untethered transition, which provides essential safety and operational benefits. From a safety perspective, the tether can be detached in critical flight states to facilitate recovery. Since the stretched tether forces are highly sensitive to minor positional deviations, a loss of control e.g. during crosswind operations can rapidly lead to significant deviations from the designed trajectory, potentially resulting in system loss due to excessive tether forces. By removing the geometric constraint of the tether, a safety mode can facilitate system recovery. Yet, this requirs a subsequent transition and landing without tether connection. Concerning the operational benefits, a general flight capability without a tether connection enhances the utility of the flight system. This capability allows system operation independently of supporting ground devices, for example, to reach a maintenance station. In offshore wind parks or remote regions that are difficult to reach, this offers significant improvements in cost-efficiency and usability. Therefore, the control concept must be designed to function effectively without relying on a stretched tether connection.

Power Consumption and Space Requirements

Low power consumption is desired for the transition of the AWE system, as it aims to enter crosswind flight as efficiently as possible. Power consumption is part of the loss account and reduces the overall performance. Additionally, it defines the sizing of the flight system's propulsion and battery system, which is dead weight in crosswind flight, except when used to recharge onboard electronics. The propulsion system's size also iteratively affects the design of the wing and the overall weight of the flight system.

The power consumption, however, is a secondary design goal. The transition is short compared to the entire crosswind flight cycle, and thus, its power demands contribute only marginally to the system's overall energy balance. Similarly, an increase in weight is less critical, since aerodynamic and tether forces dominate crosswind flight in high wind conditions, while gravitational forces become negligible. In ground-generation systems, the retraction phase even exploits weight to return to the starting position for another power cycle. As a result, weight only becomes a concern in low wind conditions close to the cut-in wind velocity, and during the brief launching phase. Robustness therefore takes priority over power consumption in the design process.

Power consumption during transition is primarily determined by thrust demand and the duration of the maneuver. Therefore, the controller design focuses on thrust required at each operating point and the time needed to complete the transition. Besides, limiting the maximum thrust is crucial regarding propulsion sizing and weight. By comparing prop-borne and wing-borne flight, prop-borne flight is characterized by a significantly higher thrust demand, as thrust must compensate for the flight system's weight. In contrast, during wing-borne flight, thrust primarily counteracts lower drag forces. Particularly prop-borne flight necessitates rapid transition due to its high thrust requirements.

The transition should be performed within a limited space to increase the applicability of the system. Some areas have strict regulations regarding land and space constraints, e.g. in populated regions, mountainous areas, or islands. For the deployment in a wind park, close spacing between the AWE systems is required to increase economic efficiency. Given that the transition occurs near the ground, where most surrounding obstacles are located, minimizing the transition space is crucial.

4.2. Launching Concept

The design of the transition requires at first the classification of a suitable launching concept. This specifies the initial and final boundary conditions for the flight trajectory of the transition in relation to the wind vector and the tether connection. Figure 4.1 depicts the launching concept for the AWE system, which provides a well-suited compromise between the design objectives. The flight system takes off in the neutral zone with the wing aligned to the wind vector. A lateral transition is performed on a straight line along the wind vector in the upwind direction. The lateral motion in this context refers to the y^{b}-axis of the initial, vertical position of the flight system during takeoff, equivalent to the y^{w}-axis. Accordingly, the longitudinal motion describes the x^{w}-, z^{w}-axes. Throughout the transition, the tether remains unstretched. The transition is followed by a curved flight

to adjust the flight radius to stretch the tether and reach crosswind flight. These flight phases are explained in detail in the following.

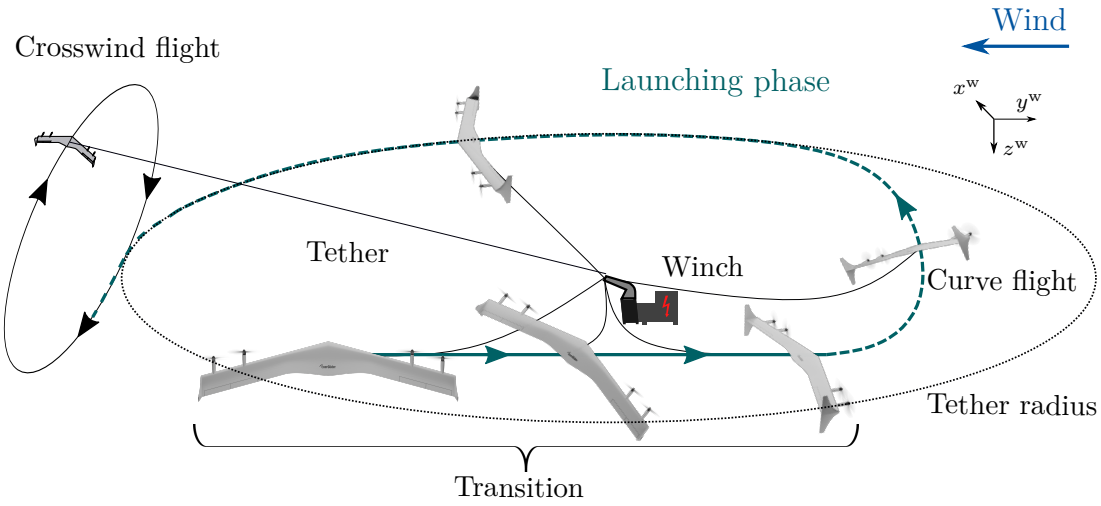


Figure 4.1.: Launching concept, consisting of the yaw-roll transition and curve flight to reach crosswind flight.

Takeoff is performed with the wing aligned to the wind vector in the neutral zone, compare with Fig. 1.2b. This ensures that the flight system can operate within its flight envelope across a wide range of wind velocities. A trimmed takeoff is possible even at high wind velocities, as the aerodynamic inflow perpendicular to the wing area is minimized. The wind vector is orientated in the lateral direction of the flight system, where drag and the generated yaw moments are minimal. Consequently, the required yaw angle to trim the flight system remains small. This arrangement enables the flight system to maintain an almost vertical attitude, ensuring precise and controlled tailsitter takeoff and landing safely on the winglets within a limited area.

In prop-borne flight, the tether remains unstretched to keep the tether forces low. In this phase, the tether forces primarily act in the longitudinal direction of the flight system. While the vertical component has to be compensated at the expense of higher thrust, the horizontal component represents an additional disturbance in the pitch axis. Since pitch is highly sensitive due to the increased longitudinal instability, the limited flight envelope, and the non-minimum phase behavior, accurate control of the stretched tether forces is not possible in prop-borne flight.

The transition is performed in the lateral direction, dominated by a yaw-roll motion. Figure 4.2 illustrates this transition maneuver in detail. The flight system initially performs a yaw-dominated motion by differential thrust in prop-borne flight, which allows for an efficient and rapid acceleration or deceleration in the lateral direction (d-e). The

aerodynamic velocity in the longitudinal direction and therefore the angle of attack can be kept low to avoid the strong pitch moments regarding the longitudinal motion, compare with Section 3.2. Once the aerodynamic velocity is sufficiently high, the flight system initiates a roll-dominated motion in wing-borne flight (f-g). By carefully increasing the angle of attack, the lift force increases and the flight system completes the transition to horizontal flight without causing stall. Note that although the name suggests a mere rotation of the yaw and roll axes, these are solely the dominant angles from an outside perspective. The complete lateral transition includes all three Euler angles denoted in the 'YZX'-sequence to trim the forces of the flight system. The corresponding definitions of the Euler angles and the relevant forces are explained in detail in Section 4.3.1.

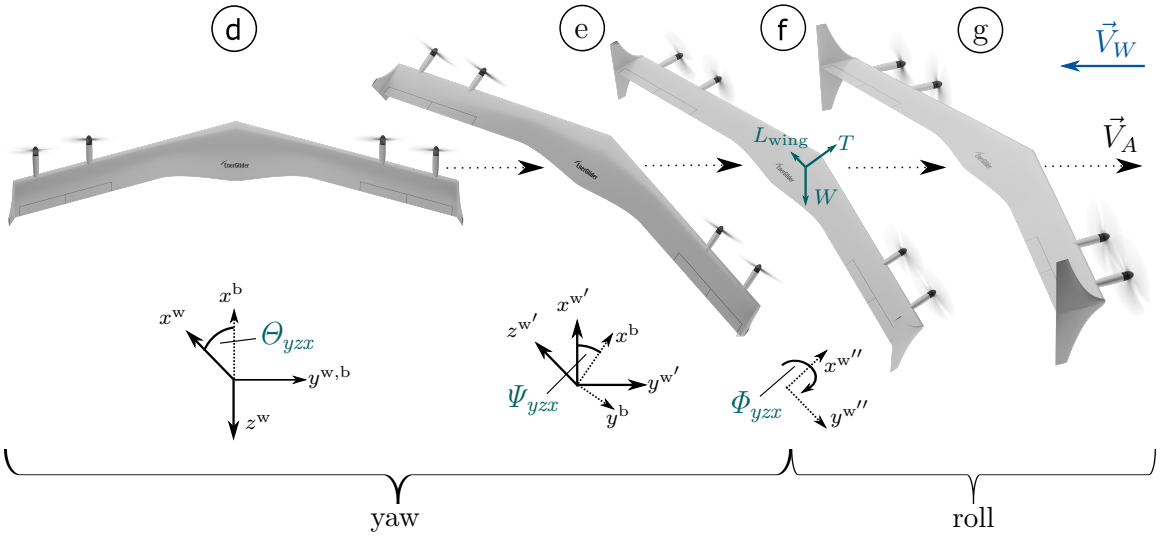


Figure 4.2.: Illustration of the lateral yaw-roll motion with the attitude angles of the 'YZX'-rotation sequence and the relevant forces during the roll motion.

The flight path of the transition is on a straight line along the main wind vector in the upwind direction. On a straight flight path, aerodynamic and wind velocities are aligned and there is no aerodynamic inflow perpendicular to the wing area during the critical prop-borne flight phase. Due to the operation in upwind direction, the wind velocity supports the transition. Following stationary takeoff at zero horizontal ground velocity, an aerodynamic velocity is already present in this direction due to the superposition with the wind velocity. As such, only the remaining velocity to reach wing-borne flight has to be generated during the transition, leading to a significantly shorter flight path with less power consumption. The longest transition path corresponds to a flight operation with no wind. The takeoff is positioned with sufficient distance to the tether radius to perform the transition without stretching the tether even in no wind conditions.

The specific yaw-roll transition allows for stationary, trimmed flight in all operating points.

The angle of attack remains within the linear range of the lift coefficient to avoid stall effects when reaching wing-borne flight. High slip angles arise instead, which however do not critically affect the moment balance of the flight system. Therefore, the yaw-roll transition can be performed at a constant height within the tether radius and can be accurately controlled in both low and high wind conditions. The stationary operation allows for transition in both directions from prop-borne to wing-borne flight and vice versa.

Having reached wing-borne flight, a curved flight is initiated to stretch the tether and operate to crosswind flight. A rotation into the wind during prop-borne flight would lead to additional centrifugal forces and a high aerodynamic inflow due to the wind in the critical, longitudinal direction. This negates the desired advantages of the yaw-roll transition. In wing-borne flight, the angle of attack is less sensitive and a curved flight can be initiated into the wind direction. Due to the transition in the upwind direction, a detour along the windward side is required before reaching crosswind flight. However, the turning radius in upwind direction and the ground velocity are small, and the thrust demand in wing-borne flight is significantly lower compared to prop-borne flight. The crossover allows for sufficient time for a smooth increase of the tether forces to a stretched tether. The tether forces can be controlled by increasing the flight radius by roll control. This avoids the non-minimum phase behavior of pitch control, enabling accurate management of the steep rise in tether force. Crosswind flight can be initiated by tilting the horizontal, circular flight path around the z^{w}-axis into the plane perpendicular to the wind vector. This approach allows simplified flight testing of both the launching and crosswind flight phases within a limited space.

The launching concept allows for a transition independently of the tether. There is no need for a bridled tether or an adjustable attachment point of the tether to control or trim the flight system during the transition. This reduces system complexity and enables a transition back to prop-borne flight and landing after a possible detachment of the tether connection during flight operation. Since the unstretched tether forces are low, it is possible to detach the tether during the transition in case of an incident during this particularly challenging flight phase.

The flight trajectory controller for the outlined yaw-roll transition of the launch is designed in the following. Takeoff and the subsequent curve flight including the operation to stretch the tether are not part of this thesis and discussed in detail in [132]. Besides, system recovery and tether detachment are not covered in this thesis.

4.3. Definition of the Operating Points

The design of the trajectory controller is based on stationary trim states as the operating points. A detailed analysis of the trim states allows the examination of performance characteristics of the flight system during the transition, such as elevon deflection and thrust demand. It shows the limitations of the flight envelope and enables the evaluation of an efficient trim path based on the design objectives. For each operating point on this trim path, a linearized flight model can be derived to assess the varying control effectiveness and precisely design the controller during the transition. The design allows stationary flight up to a specific acceleration limit for which the stationary considerations remain valid.

While the formulation of the trim condition of Eq. 2.6 is straightforward, the complexity arises from the challenge of the definition of the degree of freedom, the sampling method to identify all potential solutions that satisfy the trim condition, and the selection of the desired trim path out of the full flight envelope. The following section presents the specific methodology to derive the trim states. Subsequently, an individual selection of advantageous trim points out of the lateral flight envelope is made to find a well-suited compromise between the different design criteria. Finally, the selected trim path is linearized to derive the control effectiveness in each operating point, which is utilized for the design of the velocity controller.

4.3.1. Methodology of the Trim Calculations

To define the operating points of the yaw-roll transition, the stationary trim states of the lateral motion are analyzed, compare with Section 2.2. The yaw-roll transition couples all flight states of the longitudinal and lateral motion and therefore requires a holistic approach regarding all flight axes. The specific methodology to capture all relevant trim states is outlined in the following.

The calculation of the trim states assumes a straight flight path along the wind direction, with an unstretched tether and no curves or associated centrifugal forces, as described in Section 4.2. Table 4.1 presents the relevant flight states, controls, and trim conditions of this lateral motion. The turning rates are set to zero for the stationary trim calculations of the straight-lined transition. For a sagging tether, the tether forces are below 10 % of weight and are neglected in the trim calculations (compare with Section 2.4.2). Therefore, the trim calculations are applicable regardless of the current position of the flight system or the tether connection. The subsequent controller design is sufficiently robust to handle the deviations resulting from the tether forces and the accelerations, as shown in the model-in-the-loop simulations and the robustness analysis in Section 5.

states	controls	trim conditions
$\begin{pmatrix} u_{\mathrm{a}}^{\mathrm{w}} = 0\,\mathrm{m/s} \\ v_{\mathrm{a}}^{\mathrm{w}} = V_A \\ w_{\mathrm{a}}^{\mathrm{w}} = 0\,\mathrm{m/s} \\ \Phi_{yzx} \\ \Theta_{yzx} \\ \Psi_{yzx} \end{pmatrix}$	$\begin{pmatrix} f \\ \Delta f \\ \kappa \\ \Delta\kappa \end{pmatrix}$	$\begin{pmatrix} X \\ Y \\ Z \\ L \\ M \\ N \end{pmatrix} = \vec{0}$

Table 4.1.: Variables and trim conditions of the lateral motion.

The aerodynamic velocities are the relevant quantities for the definition of flight mechanics and are therefore considered within the trim calculations, compare with Section 2.4. Due to the rotation of the flight system in all axes, a fixed coordinate system is required as a reference system. For the stationary trim calculations, a quasi-static wind direction is assumed. The velocities are defined in this wind coordinate system, with a flight system taking off in the neutral zone on the left-hand side of the wind vector, compare with Fig. 4.1. For a lateral motion on a straight line along the wind vector, the aerodynamic velocities in the longitudinal direction of $u_{\mathrm{a}}^{\mathrm{w}}$ and $w_{\mathrm{a}}^{\mathrm{w}}$ are set to zero. The lateral velocity $v_{\mathrm{a}}^{\mathrm{w}}$ then equals the overall aerodynamic velocity V_A. It is varied from zero in prop-borne flight to $15\,\mathrm{m/s}$ in wing-borne flight, sampled in $0.5\,\mathrm{m/s}$-steps. As the velocity vector has only a single component in the lateral direction, the aerodynamic velocity results as a direct superposition of the absolute values of the ground and wind velocities. The trim calculations are therefore valid for all wind velocities for which Eq. 4.1 holds.

$$V_A = V_G - V_W \in [0 - 15]\,\mathrm{m/s} \tag{4.1}$$

The forces and moments in all three directions must be equalized for trimmed flight in each set of velocities with the support of the four flight controls: symmetrical thrust f for the X-force, differential thrust Δf for a yaw moment N, symmetrical elevon deflection κ as elevator equivalent for a pitch moment M, and differential elevon deflection $\Delta\kappa$ as aileron equivalent for a roll moment L. The forces in the Y- and Z-direction can only be applied indirectly by a rotation of the flight system to modify the directions of the aerodynamic and thrust forces.

A complex interplay of all three attitude angles is required to rotate the flight system such that the components of the forces and moments are balanced in all directions to trim the flight system in each flight state. Flight mechanics typically does not consider heading (Ψ_{zyx}), since the direction of the flight path has no effect on the flight characteristics [133].

However, the restriction of the flight path in the specific direction of the wind vector requires a specific definition of this angle. This heading is not fixed in the direction of the wind vector, and all three attitude angles vary during the transition.

The following example shall demonstrate the interaction of the attitude angles. When the velocity and angle of attack increase during the transition, lift forces increase accordingly. Simplified for illustration reasons, Fig. 4.2 depicts the dominant forces of weight, lift, and thrust for an exemplary operating point at position (f) during the transition. While the direction of the weight force is independent of attitude, the lift and thrust vectors must be precisely rotated to trim the flight system. The pitch and yaw angles define the pointing direction of the x^{b}-axis and therefore the direction of thrust. The roll and pitch angles mainly orientate the wing area with respect to the aerodynamic inflow to define absolute value and direction of the lift force. During the transition, lift has a component in the negative x^{w}-direction. As such, this component requires to be counteracted by a corresponding thrust component, which is performed by a downpitch motion to point the flight system's nose in the positive x^{w}-direction. Since the angle between the horizontal component of the x^{b}-direction and the inertial x-direction defines heading, this angle varies discontinuously during the lateral transition from zero to 90°. It therefore requires all three attitude angles as variables in the trim analysis.

The definition of a suitable rotation order of the Euler angles facilitates the description of the yaw-roll transition. Since the Euler angles define the rotation between the body and geodetic coordinate systems, the geodetic coordinate system is first rotated into the wind coordinate system for simplification. The following Euler angles are related to this wind coordinate system, in which the vertical takeoff attitude then corresponds to a mere pitch angle of 90°, regardless of the wind direction. The 'YZX'-rotation sequence is selected, with the resulting angles as depicted in Fig. 4.2. The following reasons describe the characteristics of this rotation sequence:

- The first rotation, defined by the pitch angle Θ_{yzx}, is around the y^{w}-axis. In this case, this angle still represents the pitch motion to define the velocities of the longitudinal direction, compare with Section 3.2.
- The second rotation, defined by the angle Ψ_{yzx}, is around the $z^{w'}$-axis, which corresponds to the rotated z^{w}-axis after the first rotation. In this case, this angle represents the yaw angle of the lateral yaw-roll transition, which is initiated by differential thrust. It is a direct measure of the reversed slip angle in no wind conditions and increases linearly from 0° in prop-borne flight to 90° in wing-borne flight. Ψ_{yzx} and β are therefore an appropriate representative of the progress of the transition.

- The third rotation, defined by the angle Φ_{yzx}, is around the $x^{w''}$-axis, which corresponds to the rotated x^{w}-axis after the first two rotations. In this case, this angle represents the roll angle of the lateral yaw-roll transition, which is initiated by differential elevon deflection. It is a measure of the angle of attack during the lateral motion. At $\Phi_{yzx} = 0°$, a transition is performed at a constant angle of attack of $\alpha = 0°$. There is no roll rotation of the wing area in the direction of the aerodynamic vector and hence no angle of attack. The relation between Φ_{yzx} and α is nonlinear depending on the progress of the transition.

- Note the singularity at $\Psi_{yzx} = 90°$ of this rotation sequence. Due to the applied method for the trim calculation and the usage of quaternions in the controller, this is not an issue of further interest, as explained in the following. Yet, it must be kept in mind when interpreting the Euler angles with the 'YZX'-rotation sequence.

The size of the solution space of the trim states of the lateral motion depends on the considered flight states and controls. Regarding flight controls, there is a clear allocation to the forward and rotational accelerations, resulting in a unique solution of the controls at each trim point within their respective limits. However, with four flight controls available to induce the three moments L, M, N and the X-force, four flight states can be independently controlled as desired. Next to the three aerodynamic velocities, an additional rotation angle can be defined according to the design criteria.

The pitch angle is essential for setting the longitudinal velocities to zero in order to satisfy the trim conditions of the longitudinal motion, compare with Section 3.2. Within the range of small velocities, the pitch angle emerges as a unique solution to trim the flight system in the longitudinal direction. Consequently, one of the lateral yaw or roll angles can be independently selected in each trim point, allowing the definition of one of the desired aerodynamic angles for the operating points. However, which of these lateral angles is independently selectable depends on the specific velocity during the transition. Besides, the remaining lateral angle must not be uniquely assigned to each set of velocities. During the transition, a set of flight velocities can be trimmed utilizing lower thrust and higher lift, or vice versa. Furthermore, various combinations of aerodynamic angles can generate the same amount of lift. Since the aerodynamic angles are determined by the lateral Euler angles Φ_{yzx} and Ψ_{yzx}, the solution space is ambiguous concerning these lateral angles. For a given set of three velocities and one lateral Euler angle, the pitch angle is uniquely defined in each trim point, while there can be multiple solutions regarding the remaining lateral angle.

The ambiguity of the solution space requires a specific scanning algorithm to identify all lateral Euler angles that satisfy the trim condition, see Fig. 4.3. For each velocity, the entire range of the lateral Euler angles from 0° to 90° is divided into small segments of 5°, resulting in a grid of $n \times n$ precisely sampled segments of the attitude sphere. Each segment is defined by its minimum and maximum angles. For each set of velocities in each segment, all six functions of the forces and moments are minimized to solve for the corresponding flight controls $\vec{u}_\mathrm{t}$ and Euler angles $\underline{\Phi}_{yzx}$ under consideration of the attitude limits of the segment, see Eq. 4.2. If all forces and moments in this local minimum are equal to zero, the trim condition is satisfied, and the corresponding flight controls and attitude angles trim the specified aerodynamic velocity $V_{A,k}$. This method therefore identifies all trim solutions with an accuracy determined by the selected grid size of 5°.

$$\min_{\substack{\Phi\in[\Phi_{j-1},\Phi_j],\\ \Psi\in[\Psi_{m-1},\Psi_m],\\ \Theta,\vec{u}_\mathrm{t}}} \{FM\}_i \left(\vec{V}_\mathrm{A} = [0, V_{A,k}, 0]^\top, \underline{\Phi}, \vec{u}_\mathrm{tp}\right) \stackrel{!}{=} 0 \tag{4.2}$$

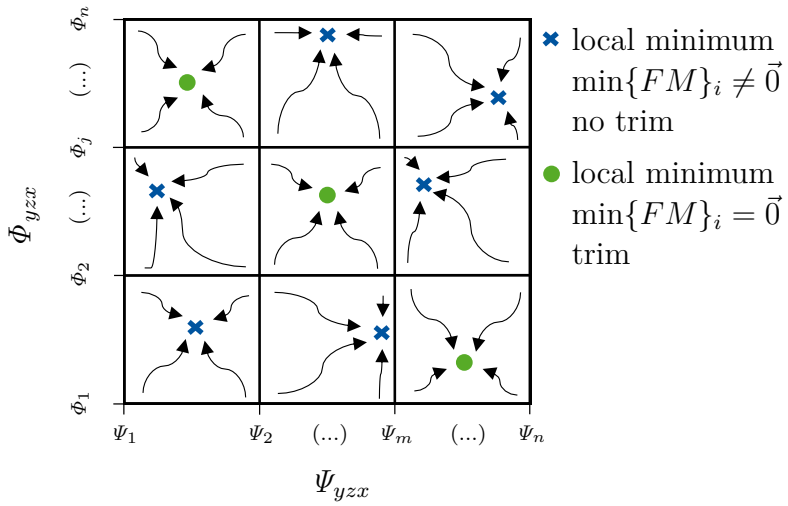


Figure 4.3.: Scanning method of the lateral Euler angles to screen the trim states.

Combining all calculated trim states for a given aerodynamic velocity leads to isolines, which can be analyzed to derive the desired operating points of the yaw-roll transition. The advantage of selecting the 'YZX'-rotation sequence of the Euler angles is that the scanning method is only required for the lateral angles of this sequence, while the longitudinal angle is uniquely defined in each trim state. This reduces the dimension of the scanning method and allows the selection of the operating points based on a representation of these lateral angles. Due to the fine sampling of the angles, the gimbal lock of the Euler angles is not an issue and solely leads to a sampling of the same attitude in several grids.

4.3.2. Identification of the Trim Path

In the following, the trim states of the lateral motion are calculated based on Section 4.3.1 and analyzed with respect to elevon deflection and thrust demand. Out of the full range of possible trim states for all velocities, the desired operating points for the yaw-roll transition can be derived based on the design objectives. The solution space of the trim states has a degree of freedom concerning the lateral angles, which can be utilized to select a beneficial trim path from prop-borne to wing-borne flight. This process is explained in the following.

The analysis is reduced to the representation of the aerodynamic angles as the relevant angles for the aerodynamic forces. The slip angle is thereby representative of the yaw angle Ψ_{yzx}, while the angle of attack corresponds to the roll angle Φ_{yzx}. Both aerodynamic angles are undefined in the region of zero velocities. Since their functions do not have a singularity but strive towards a final value of 90°, the aerodynamic angles are approximated for an infinitesimally small aerodynamic velocity in the case of no inflow. Following this method of representation, it has to be noted that for each trim state, a third angle is required to close the trim condition. It corresponds to the air-path bank angle that defines the rotation of the lift force around the axis of the velocity vector. As for the pitch angle, this angle is uniquely defined in the trim state. To evaluate and select suitable trim states for the flight path, this angle is therefore of no further relevance and is not shown in the trim plots. For a detailed analysis including all three Euler angles, it is referred to [38]. Besides, a depiction of the trim states as a function of the yaw and roll angle is given in Appendix C.

Figure 4.4 depicts the resulting isolines of the trim states of a fixed aerodynamic velocity V_A, as a function of the slip angle β and the angle of attack α. For each trim state, the colored legend marks the corresponding absolute value of the maximum elevon deflection angle $\kappa_{\max} = |\kappa + \Delta\kappa|$. At selected points (a-g), the flight system's attitude is depicted, referring to Fig. 3.2 and Fig. 4.2. Besides, the selected trim path of the yaw-roll transition from $V_\mathrm{A} = 0 - 13\,{}^\mathrm{m}/_\mathrm{s}$ and the maximum angle of attack before stall of the AWE system are indicated.

The flight system hovers in prop-borne flight at point (d). Following the isoline at zero velocity to point (a) corresponds to a roll rotation of $\Phi_{yzx} = -90°$ around the x^b-axis, compare with Appendix C. From this point, the lateral velocity can be increased by a pure longitudinal pitch motion with a decreasing angle of attack from 90° to 0° (a-c). This process therefore consists of the identical trim states of Fig. 3.2 of the horizontal pitch transition with no upward velocity. This includes the range of untrimmed flight states

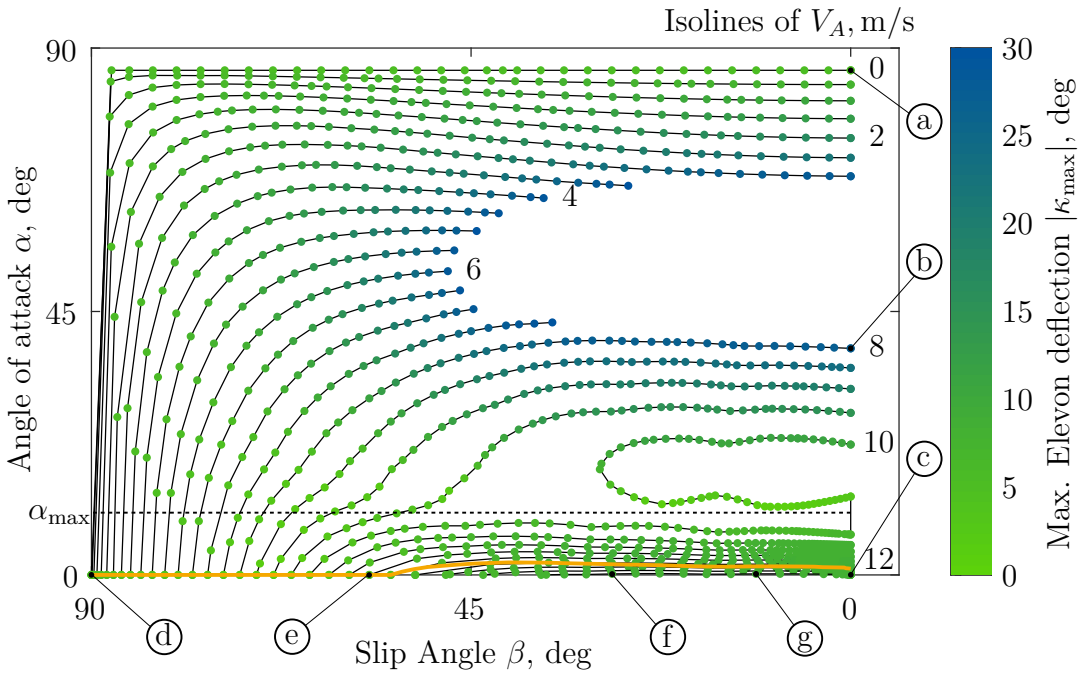


Figure 4.4.: Flight envelope of the lateral motion.

and stall effects at high aerodynamic velocities and angle of attack, with a corresponding large elevon deflection. However, the lateral motion allows for additional transition paths, for example along the trim path (d-g) and finally (c) in horizontal, wing-borne flight. Following these trim states aligned on the x-axis corresponds to a motion with an angle of attack or roll angle of zero, while the slip angle continuously decreases on this trim path. The aerodynamic forces generate low moments across all trim states, resulting in minimal elevon deflections and maintaining a significant margin from the untrimmed range. At point (c), the singularity of the 'YZX'-rotation sequence arises, leading to a highly dense sampling of the trim states.

To evaluate the thrust demand in each trim state, Fig. 4.5 presents the identical trim analysis of the lateral motion, incorporating an additional axis for the load factor $n_{f,i,\max} = {}^{f+\Delta f}/_{W}$, which represents the maximum thrust-to-weight ratio of one propulsion unit. This ratio ranges from $n_{f,i,\max} = 0.25$ in hover flight at zero velocity (adding up to one with four propulsion units) to $n_{f,i,\max} = 0.3$ at a slip angle of approximately $\beta = 50°$ and $\alpha = 0°$. In these flight states, where lift forces remain low, thrust must compensate for weight. As the aerodynamic velocity increases, the slip angle decreases due to the initialization of the yaw motion. Consequently, the vertical component of the thrust vector is reduced and thrust must increase to equalize weight. However, by increasing the angle of attack, lift forces increase accordingly and lead to reduced thrust demand when reaching wing-borne flight. When exceeding the maximum angle of attack at which stall effects occur, the

thrust demand increases again. Note that the aerodynamic angles are highly sensitive at low velocities. Slight modifications of the roll angle lead to high angles of attack and increased thrust demand. Besides, the velocity is not high enough to generate sufficient lift to completely equalize weight. As such, the effect of decreased thrust with increasing angle of attack is only noticeable above a certain flight velocity around 10 m/s.

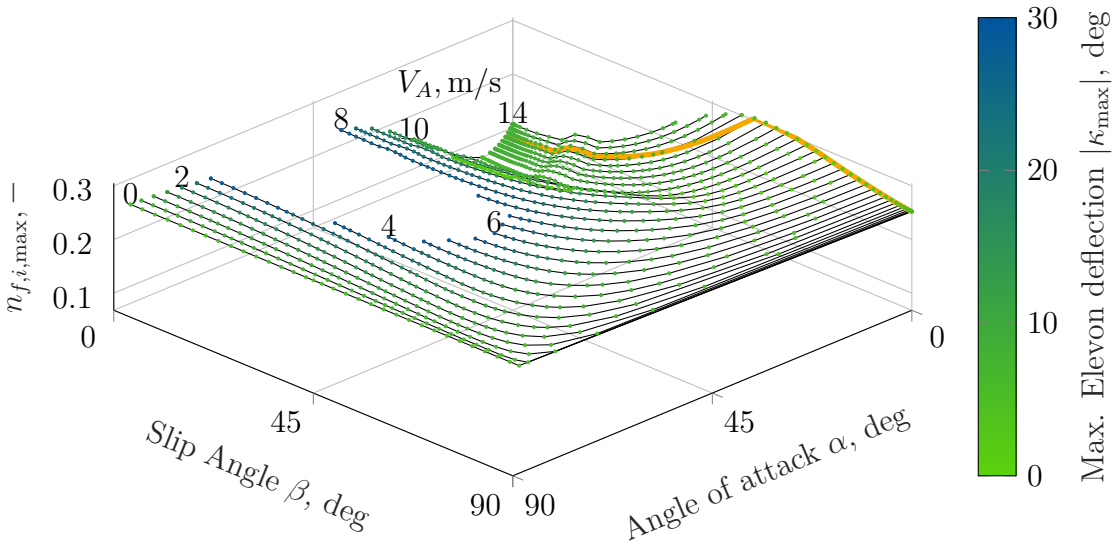


Figure 4.5.: Flight envelope of the lateral motion with maximum thrust-to-weight ratio.

The selected trim path of the lateral yaw-roll transition from prop-borne to wing-borne flight is indicated in the flight envelope of Fig. 4.4 and Fig. 4.5. Additionally, Fig. 4.6 depicts the detailed course of the flight states and controls of the trim path as a function of the reversed slip angle, which is uniquely defined and linearly decreasing during the transition. The absolute values of the Euler angles are presented with the corresponding pitch angle of the trim states. The lift factor $n_{l,z}$ denotes the vertical component of the lift force in relation to weight, allowing to classify the flight phases of prop-borne and wing-borne flight during the transition. These phases define vague expressions depending on the proportion of the current lift forces, which begin to increase even at an angle of attack of zero due to the aerodynamic inflow with sideslip. However, the yaw and roll motions are clearly separated at the point where the roll angle is increased to increase the angle of attack.

The selected trim path fulfills the desired design objectives regarding low thrust demand with sufficient reserves of the elevon deflection for robustness against external disturbances. There is adequate distance to the maximum angle of attack to avoid stall effects. The

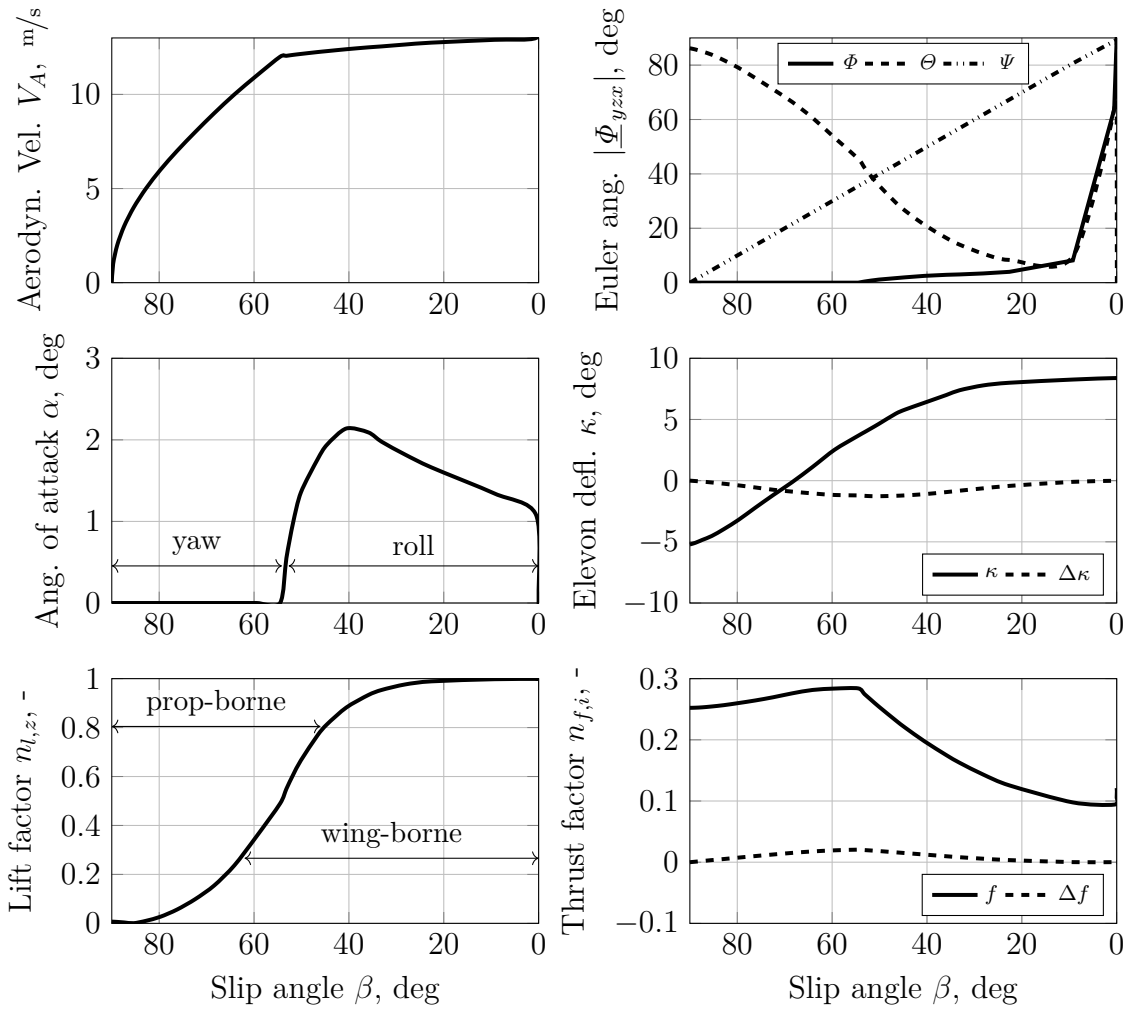


Figure 4.6.: Course of the relevant flight states and controls of the selected trim path of the yaw-roll transition.

detailed course of the flight states and the selection of the trim path is explained in the following.

During the initial yaw motion, the aerodynamic velocity increases with decreasing slip angle. Lift gradually increases, accompanied by a corresponding decrease in pitch angle to balance the horizontal component of lift. A low elevon deflection is the highest priority to maintain sufficient distance to the untrimmed flight range for robustness to wind disturbances. The operating points are selected such that the angle of attack is kept zero during the yaw motion. The moment coefficient of the 2D polar is largely symmetric for both positive and negative angles of attack, compare with Fig. 2.7. The coefficient increases significantly when the maximum or minimum lift coefficient is exceeded and stall effects emerge with a backward shift of the aerodynamic center, compare with Fig. 2.8. The absolute minimum of the pitch moment occurs at the angle of attack α_0 for zero lift, representing the maximum

distance from the angle of attack at which the pitch moment starts to increase. The zero angle of attack of the AWE system is $-1.5°$ and hence, close to zero. The pitch moment of the flight system is therefore close to its minimum in the range of low angles of attack and the distance to the untrimmed range is large. It is not expedient to optimize for the absolute minimum of the elevon deflection during the yaw motion. The angle of attack is highly sensitive in this flight phase, as small disturbances, e.g. caused by gusts, can lead to strong varying angles of attack. Besides, there is no guarantee that the identified optimum is truly optimal due to model inaccuracies. The orientation of the wing area is therefore continuously kept aligned to the aerodynamic velocity vector. This prevents a perpendicular aerodynamic inflow of the wing area which would otherwise induce stronger pitch moments. The trim path allows for rapid yaw acceleration by differential thrust in prop-borne flight without roll interference. As less lift is generated compared to flight at higher angles of attack, increased thrust demand is accepted in exchange for enhanced robustness. The elevon deflection remains within small boundaries of $5°$ during the yaw motion. This guarantees sufficient robustness concerning the untrimmed flight range and provides sufficient control reserves for the flight controller to adjust the flight orientation along a dynamic rotating wind vector.

At the beginning of the roll motion, the angle of attack increases, with a corresponding increase in lift and a reduction of thrust. Due to the aerodynamic velocity at high slip angles, a moderate differential elevon deflection and differential thrust are required to balance the aerodynamic forces in the lateral direction of the flight system. The roll motion should be initiated as early as possible to reach thrust-efficient, wing-borne flight. However, performing this rotation at low velocities and high slip angles is critical, as the flight system is still in an upright attitude (compare with position (e) in Fig. 4.2), where wind disturbances can cause rapid turnovers to the stall region, leading to undesired or untrimmed flight states. Therefore, a trade-off between robustness and thrust is required. Due to the prioritization of robustness, the aerodynamic velocity is increased until $V_A = 12\,\mathrm{m/s}$, where a horizontal aerodynamic inflow disturbance of $\Delta u_a^{\mathrm{w}} = 3\,\mathrm{m/s}$ cannot lead to stall effects. A slight roll motion is initiated with a corresponding rise of the angle of attack close to $3°$. This angle is intentionally kept significantly below the limits for maximum lift due to the high sensitivity of the angle of attack. At the selected velocity for roll initialization, the flight system can safely remain within its flight envelope and ensures the defined robustness range of $\Delta u_a^{\mathrm{w}} = 3\,\mathrm{m/s}$.

In the final flight phase of the transition to horizontal wing-borne flight, the slip angle continues to decrease until it reaches zero. During this phase, the flight system rotates with its nose in the direction of the aerodynamic inflow, leading to an increased component

along the x^{b}-axis. This alignment results in greater lift and hence reduced thrust demand. When the yaw angle reaches 90°, the singularity occurs, causing the absolute values of the roll and pitch angles to increase sharply, even though the actual attitude of the flight system remains unchanged.

For minimal thrust demand regarding the stationary trim states, the roll motion should be performed at a constant aerodynamic velocity. However, the velocity during the roll motion is slightly increased such that a constant velocity gradient corresponds to a constant angular distance of the trim states. First, this guarantees a bijective correspondence between the operating point and aerodynamic velocity, allowing the flight controller to set the operating point based on the commanded velocity. This enables a uniform interface to control tasks of the subsequent flight phases. Second, the flight limits for maximum angular acceleration during the roll phase can be mapped to a limitation on the linear acceleration of the transition. This allows the integration of rotational limits of the roll motion into the control cascades corresponding to the bandwidth of the linear acceleration. Third, the increase in velocity during the roll motion prevents the need for abrupt deceleration of the flight system before roll initialization. Since the transition is intended to be operated at high accelerations, a roll motion at constant velocity would require a complete deceleration of the flight system, therefore increasing the time for transition or power consumption. An increase in velocity during roll motion leads to a smoother transition between yaw and roll motions. Yet, the increase in velocity is limited since it results in a higher, absolute thrust demand of the trim states. To optimize for minimal power consumption, an unsteady analysis of the transition with maximum acceleration is required, extending beyond the range of the stationary trim calculations. This aspect is not considered within this thesis. Instead, a slight increase in aerodynamic velocity of $V_A = 1\,\mathrm{m/s}$ during the roll motion is selected such that the transition is completed at a velocity of $13\,\mathrm{m/s}$ in wing-borne flight, with a slip angle of zero and a lift factor of one.

4.3.3. Linearization of the Trim Path

The design of the launch trajectory controller requires a linearization of each selected operating point along the trim path of Section 4.3.2. The linearization allows the identification of control effectiveness and dynamic characteristics in each trim state. The linearized model is utilized as the basis for the design of the velocity controller in the next section.

The nonlinear control plant of Section 2.4 is transformed for each selected trim state into a linear state-space representation of Eq. 2.7. The linearization is performed in analogy to [89]. The Jacobian matrix $\boldsymbol{J}$ of the partial derivatives of the state variables

$\vec{x} = \left[\vec{\omega}^{\mathrm{b}}, \vec{V_A}^{\mathrm{b}}, \underline{\Phi}\right]^{\top}$ and control variables $\vec{u} = [f, \Delta f, \kappa, \Delta\kappa]^{\top}$ is determined to describe the linear correlation to the effective accelerations on the flight system, see Eq. 4.3.

$$\delta\dot{\vec{x}}^{\mathrm{b}} = \boldsymbol{J}_{\vec{x}}(OP) \cdot \delta\vec{x} + \boldsymbol{J}_{\vec{u}}(OP) \cdot \delta\vec{u} \tag{4.3}$$

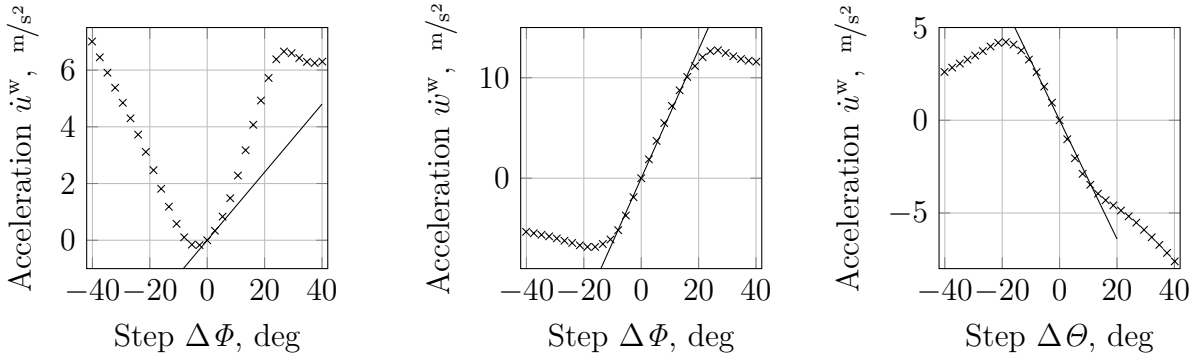
The linearization is utilized for the design of the velocity controller, as explained in detail in Section 4.4 and 4.5. It requires the aerodynamic velocities in the wind coordinate system as the state variables $\vec{x} = \vec{V}_A^{\mathrm{w}}$, while the Euler angles and thrust serve as the control variables $\vec{u} = [\underline{\Phi}, f]^{\top}$. As such, Eq. 4.3 is transformed and rearranged in accordance with [134].

The challenge in linearization is selecting appropriate step sizes to ensure that the linear approximation accurately represents the nonlinear function. For each state and control variable, the nonlinear function of the accelerations in all directions is evaluated at several discrete steps around the operating points to identify their functional values. The linear approximation is then calculated for a suitable step size.

The yaw motion and the end of the roll motion are characterized by widely strict monotonic functions of the accelerations, for which the linearization is an accurate representation of the nonlinear function. However, the beginning of the roll motion when the angle of attack reaches its maximum at $\beta \approx 40°$ is in particular critical (compare with Fig. 4.6). The angle of attack is still highly sensitive and close to the nonlinear region of stall. The Euler angles significantly influence the angle of attack in this flight phase. Therefore, this thesis limits the analysis of the linearization to the accelerations resulting from variations in the Euler angles, with a focus on the dominant effects on the accelerations $\dot{w}^{\mathrm{w}}$ and $\dot{u}^{\mathrm{w}}$.

Figure 4.7 depicts the resulting accelerations of the control plant due to deviations of the dominant roll and pitch angles from the operating point at $\beta = 40°$. In the exact location of the operating points at $\Delta\underline{\Phi} = 0°$, the resulting acceleration is zero due to the stationary trim consideration, while angle deviations lead to certain accelerations. Besides, the calculated linear approximation of the sampling points is depicted. In general, stall effects should be avoided by the flight controller. Therefore, the linearization considers only the sampling points that are within the linear range of the lift coefficient. This prevents the linear approximation from being affected by sampling points that are intentionally not part of the flight operation.

The suitability of the control plant's linearization varies depending on the direction of acceleration and the associated control variable. Considering the acceleration $\dot{u}^{\mathrm{w}}$ by a deviation of the roll angle, it can be identified that the operating point is close to a



(a) Roll angle to $\dot{u}^{\mathrm{w}}$ (b) Roll angle to $\dot{w}^{\mathrm{w}}$ (c) Pitch angle to $\dot{u}^{\mathrm{w}}$

Figure 4.7.: Samplings of the resulting accelerations of the control plant with the linear approximation line.

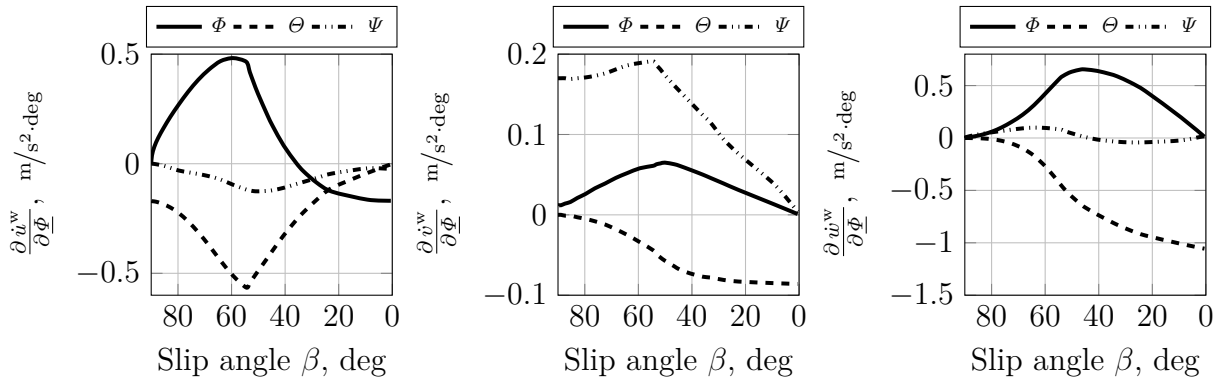
minimum, see Fig. 4.7a. The roll angle has a dominant influence on the direction and absolute value of the lift force. A negative increase of the roll angle initially leads to an increase in the angle of attack and the lift force. Since the horizontal component of the lift force points in the close range of the operating point in the negative direction of x^{w}, this leads to a negative acceleration, compare with Fig. 4.2 point (e,f). However, when the roll angle further increases and stall effects occur, lift forces decrease rapidly. At the same time, the negative roll angle rotates the lift force in the positive direction of x^{w}. In combination, this eventually leads to a positive acceleration and a reversal of the effect. The linearization is therefore only valid in a restricted range around the operating point.

The effect of the reversal of the acceleration is less distinctive considering the vertical acceleration $\dot{w}^{\mathrm{w}}$, see Fig. 4.7b. The initial increase of lift due to a negative roll angle leads to an upward acceleration $\dot{w}^{\mathrm{w}}$ in the negative direction. Although a further increase of the roll angle also causes stall and therefore a reduction of lift, the effect of acceleration reversal is weakened since lift simultaneously rotates upwards. While the absolute value of lift is reduced, its vertical component increases. Consequently, the minimum of the function occurs at significantly larger deviations from the operating point and the linearization is valid in a much larger range compared to the $\dot{u}^{\mathrm{w}}$ acceleration.

The horizontal acceleration $\dot{u}^{\mathrm{w}}$ can be induced in comparison to roll adjustments more effectively and robustly by a pitch deviation, see Fig 4.7c. Since the pitch angle predominantly affects the direction of thrust, the acceleration is widely linear around the operating point. A decrease in pitch points the flight system's nose in positive x^{w}-direction, leading to a positive acceleration due to the larger thrust component in this direction. The linearization is valid for significantly larger deviations in pitch compared to the roll angle.

For the finalized linearization across all directions and operating points, the control effectiveness can be assessed throughout the transition. The linearized values regarding a specific acceleration in one direction are combined for all operating points and a given control input. This allows for evaluation of how the control effectiveness varies along the trim path of the transition to recognize the dominant controls in each direction.

Figure 4.8 depicts the linear derivatives of the acceleration related to a change in Euler angles, plotted over the slip angle. Vertical prop-borne flight at $\beta \approx 90°$ and horizontal wing-borne flight at $\beta \approx 0°$ are characterized by a clear allocation of the Euler angles. In vertical flight, the $\dot{u}^{\mathrm{w}}$-acceleration is induced by pitch, while the yaw angle mainly induces a $\dot{v}^{\mathrm{w}}$-acceleration, both due to the change of the thrust direction. The roll angle has no effect, since it only changes the orientation of the flight system. In horizontal wing-borne flight, the roll angle initiates curve flight and therefore a $\dot{u}^{\mathrm{w}}$-acceleration. The $\dot{w}^{\mathrm{w}}$-acceleration is induced by an increase of the angle of attack by pitch, which also affects the $\dot{v}^{\mathrm{w}}$-acceleration. In between, the effects change according to the rotation of the flight system and the changes of the aerodynamic angles. In particular, the influence of roll and pitch on the $\dot{u}^{\mathrm{w}}$-acceleration during roll initialization at $\beta \approx 60°$ shall be highlighted. Although the validity range of the linearization due to a roll angle is strictly limited regarding this acceleration, its effectiveness is as dominant as the effectiveness of pitch. A suitable control allocation in the controller design is therefore required that respects both the effectiveness and the validity range of the linearization of the Euler angles for robust control. The effectiveness of thrust and the damping effects of the velocities are given in Appendix C. Damping effects are especially of relevance in the z^{b}-direction due to the large wing area.



(a) $\dot{u}^{\mathrm{w}}$-acceleration (b) $\dot{v}^{\mathrm{w}}$-acceleration (c) $\dot{w}^{\mathrm{w}}$-acceleration

Figure 4.8.: Control effectiveness of the Euler angles during the transition.

4.4. Control Concept

The launch trajectory controller allows precise control of the aerodynamic velocity of the selected lateral yaw-roll transition along a straight flight path along the wind vector. To accomplish this, the controller must perform multiple tasks simultaneously. In addition to stabilizing the attitude, it must accurately control the trim path along the selected operating points while maintaining the boundary conditions regarding position and wind alignment. Therefore, the trajectory controller is designed in a cascaded control structure, see Fig. 4.9. Each control loop is assigned a delimited task, leading to clear interfaces between the individual controller (ctrl) cascades. The structure is based on the requirements of the control tasks, each individual control loop is arranged based on controller bandwidth. This allows individual design of the cascades according to accuracy and robustness requirements [135].

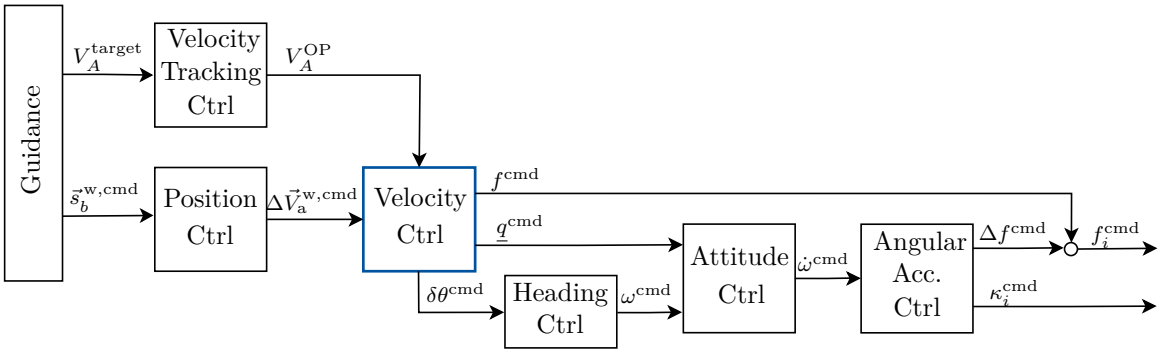


Figure 4.9.: Control structure. The measured states are not depicted.

At the highest level of the cascade, the guidance initiates the transition after takeoff by setting the target velocity V_A^{target} to the desired aerodynamic velocity in wing-borne flight. The position command from the guidance maintains a constant position in the longitudinal direction. On the lower cascade, the position controller commands corresponding deviations of the velocity to maintain the specified position. Besides, the velocity tracking controller integrates the maximum acceleration limits and defines a dynamic course of the aerodynamic velocity command V_A^{OP} that gradually reaches the target velocity. This velocity command uniquely defines the current operating point. These operating points are integrated into the velocity controller as the highlighted core of the trajectory controller. The velocity controller commands the corresponding attitude angles and thrust of the associated trim states, with deviations added to maintain the velocities at each trim point. A linear interpolation between the operating points based on gain-scheduling is performed for smooth control. The heading controller adapts the orientation of the flight system to align the aerodynamic velocity with a rotating wind vector. At the lowest level of the cascade,

the angular acceleration and attitude controllers stabilize the system in all axes and ensure that the desired attitude is achieved. A detailed description of each control loop is given in Section 4.5.

The velocity controller is designed based on the stationary trim calculations to maintain the current operating point, and it requires suitable coordination with the velocity tracking controller to achieve the dynamic motion necessary for the transition to wing-borne flight. This functionality can be explained by the phase space diagram, as shown in Fig. 4.10. The transition is initiated after takeoff at $V_G = 0\,\mathrm{m/s}$ in prop-borne flight, with the aerodynamic velocity matching the wind velocity for the wind-aligned flight system. The transition is finished at the target velocity $V_A^{\mathrm{target}} = 13\,\mathrm{m/s}$ in horizontal, wing-borne flight. The phase space diagram depicts two exemplary operating points and flight states during the yaw and roll motions. The operating point (OP) represents the commanded trim state for which the velocity controller is designed, while the flight state (FS) indicates the current state of the flight system. The y-axis shows the velocities of the longitudinal motion, serving as representatives for all relevant flight states of the attitude angles and turning rates of the transition.

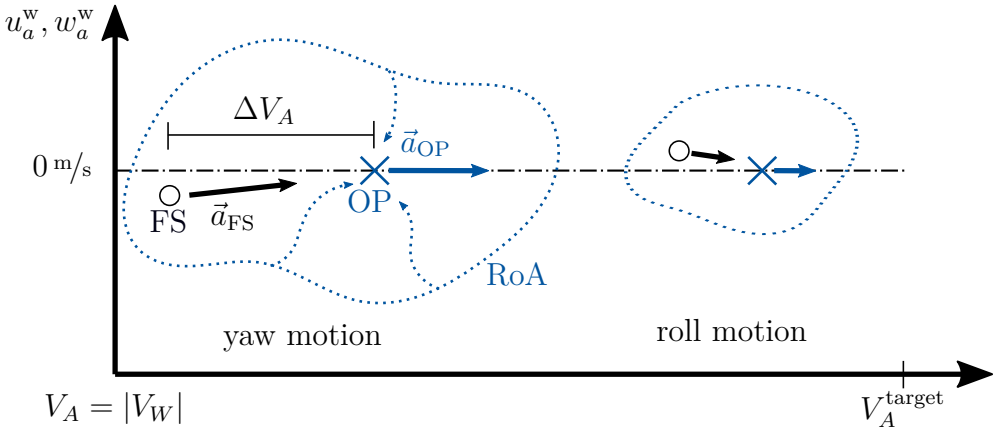


Figure 4.10.: Functionality of the control concept illustrated in the phase space diagram.

The velocity tracking controller defines the dynamic time course of the commanded velocity of the OP with the selected acceleration $\vec{a}_{\mathrm{OP}}$ until target velocity. Meanwhile, the velocity controller generates the acceleration $\vec{a}_{\mathrm{FS}}$ of the FS toward the designated OP to ensure that the FS follows the commanded OP. At initialization of the transition, the velocity tracking controller commands an increase of the velocity of the OP according to the maximum acceleration of the current flight phase. The strength of the attraction (or acceleration) of the FS towards the OP is determined first, by the difference of the flight states between FS and OP (mainly given by the difference in aerodynamic velocity, marked with ΔV_A) and second, by the transient behavior of the designed velocity controller. A higher dynamic

closed-loop system of the velocity controller results in a faster acceleration towards the OP. A balance is established when the attraction strength is sufficient for the FS to follow the OP with synchronized acceleration.

Each OP of the linear velocity controller is associated with a defined region of attraction (RoA), which mainly differs between the yaw and roll motions. The RoA defines the set of initial conditions from which the FS will eventually converge to the desired equilibrium point. The RoA is a function of n dimensions, where n is the number of flight states corresponding to the OP [136]. Due to the linear behavior of the designed velocity controller, nonlinear dynamics of the flight system can lead to the FS being beyond the RoA and it has to be ensured that the FS is within the domain of the RoA for stable operation. In comparison to the yaw motion, the roll motion exhibits a reduced RoA. First, the flight system is in wing-borne flight where lift forces are significant; yet the angle of attack is particularly sensitive during the initial roll motion, making small deviations likely to reach the nonlinear stall region, compare with Section 4.3.3. Second, the gradients of the FS are steep since the operating points are selected based on small differences in aerodynamic velocity, compare with Section 4.3.2. However, since the difference in velocity of the selected operating points during the roll motion corresponds to a constant angular rate, the limits of the maximum angular acceleration can be mapped to a maximum linear acceleration of the OP.

The velocity tracking controller ensures that the FS remains within the RoA of the OP by considering dynamic acceleration limits during the transition. The maximum acceleration limits of the flight system are defined by the flight controls. While the maximum acceleration of the yaw motion is predominantly limited by differential thrust, the roll motion is mainly restricted by elevon deflection. However, for robust control, the RoA further restricts the maximum acceleration. Higher commanded accelerations for a rapid transition increase the distance between the OP and FS and reduces the robustness of the controller to disturbances with respect to the RoA. During the roll motion, the RoA is significantly smaller, necessitating a reduction in the commanded acceleration to maintain stability. Additionally, the velocity tracking controller dynamically reduces the commanded acceleration in case of disturbances, when the aerodynamic velocity between OP and FS exceeds its limits to ensure flight within the RoA.

4.5. Controller Implementation

The focus in this thesis is placed on the velocity controller, as highlighted in Fig. 4.9. It is the core of the trajectory controller which incorporates the selected operating points of

the transition. The velocity controller commands thrust and attitude angles based on the input of the commanded aerodynamic velocity of the OP and the required deviations of the velocity to maintain the longitudinal position as defined by the position controller. Its implementation is explained in detail in the following. In interaction with the surrounding control cascades, the desired transition can be performed accurately. These different cascades of the trajectory controller are outlined subsequently.

4.5.1. Implementation of the Velocity Controller

The velocity controller allows precise control of the velocity in all three axes at the defined operating point. The controls of the Euler angles and thrust are allocated according to their control effectiveness to provide the necessary accelerations to reach the desired operating point. The controller respects damping effects of the system, the delays of the underlying controller cascades, and the individual range of validity of the linearization. At each operating point, linear dynamics are assumed according to the state-space representation in Section 4.3.3, and the controller is designed in the region around this operating point. The design is based on a gain-scheduling method [137]. The control parameters between subsequent operating points are linearly interpolated to define a continuous control law. The design is therefore valid within the region of attraction and is limited to a moderate acceleration of the commanded operating points.

An approach based on a linear-quadratic regulator (LQR) is implemented for the velocity controller. LQR is an effective control strategy for multi-input, multi-output systems, which ensures that the system achieves the desired performance with minimal actuator usage and guaranteed gain and phase margins. It has been successfully applied in several applications which include the task of trajectory tracking, nonlinear system behavior, and robust stabilization in uncertain environments [89, 138, 139, 140].

LQR is part of the optimal control theory which calculates the linear feedback gain of the controller based on a cost function of a performance index. The performance index includes the error of the states to the reference value and the expense of the control signal to reach the reference. The cost function J is minimized to calculate the control law of the optimal feedback K_{LQR} of the system, see Eq. 4.4 and Eq 4.5. [141]

$$\min_{K_{\mathrm{LQR}}} J = \min_{K_{\mathrm{LQR}}} \int_0^\infty \left[x^{\mathrm{T}}(t) Q x(t) + u^{\mathrm{T}}(t) R u(t) + 2x(t)^{\mathrm{T}} N u(t) \right] dt \tag{4.4}$$

$$u = -K_{\mathrm{LQR}} \cdot x \tag{4.5}$$

The control plant is defined by the linear state-space representation of Eq. 2.7. The optimal feedback gain is calculated by solving the Riccati equation, see Appendix D. The matrices Q and R represent the weighting matrices to penalize the corresponding error of the states and the control signals. The additional weighting matrix N serves as the cross-term matrix, which penalizes the combination of state and control signal. Note that the robustness properties of LQR control are not guaranteed when inserting the cross-term matrix [142].

The control structure of the velocity controller is presented in Fig. 4.11. The selected operating points of Section 4.3.2 are stored within the feedforward control (superscript ff). Each operating point defined by the aerodynamic velocity V_A^{OP} corresponds to a set of thrust f^{ff} and attitude angles in the representation of a quaternion $\underline{q}^{\mathrm{ff}}$. To reduce computational effort, these operating points are narrowed down to only the most relevant ones, such that operating points with nearly identical flight states are extracted [76]. Thrust is interpolated between the commanded operating points, while slerp is applied to interpolate quaternions, compare with Eq. 2.5. The application of the operating points within the bandwidth of the velocity controller reduces model dependencies and allows accurate verification in flight tests to assess the underlying flight model.

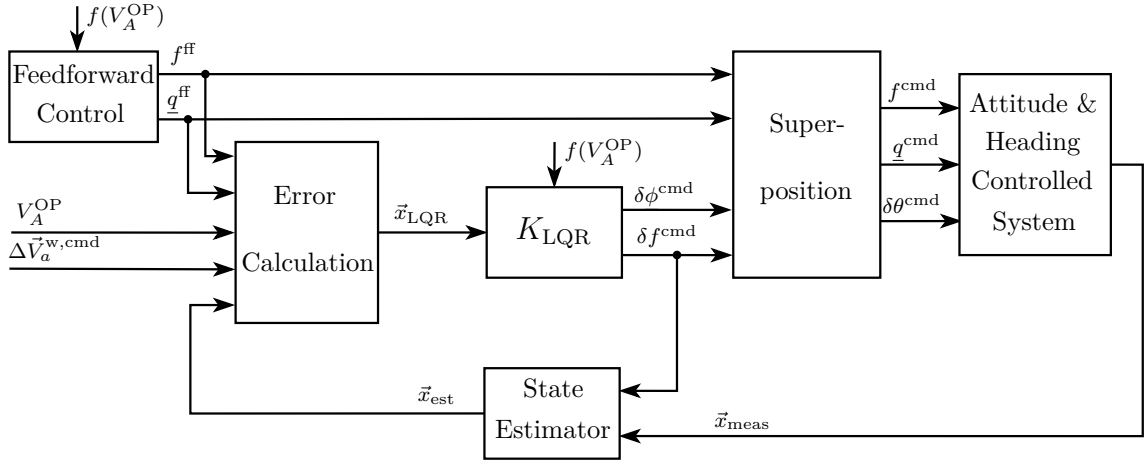


Figure 4.11.: Control structure of the velocity controller.

The state vector of the LQR is given by $\vec{x}_{\mathrm{LQR}} = \left[\int \delta\vec{V}_A^{\mathrm{w}}, \delta\vec{V}_A^{\mathrm{w}}, \delta\underline{\Phi}, \delta\omega, \delta\dot{\omega}, \delta f, \delta\dot{f}\right]^\top \in \mathbb{R}^{17x1}$. The velocity components in all axes are included as part of the LQR flight states and are defined in the wind coordinate system. Since the body coordinate system rotates according to the commands of the attitude controller at a higher bandwidth, it is unsuitable for defining the velocities. Additionally, the integrals between the difference of commanded and current velocities are fed back to allow stationary accuracy. The difference ensures that the velocity is no longer integrated when it matches the commanded velocity. The controller outputs the commands of the attitude angles and thrust $\vec{u} = \left[\delta\underline{\Phi}^{\mathrm{cmd}}, \delta f^{\mathrm{cmd}}\right]^\top$.

However, since the linearization of Section 4.3.3 is based on the actual values of the attitude angles and thrust, the system is extended by the closed-loop system of the attitude control and the actuator dynamics of thrust. Therefore, the relevant states are an additional part of the LQR states, enabling the velocity controller to account for the transient behavior of thrust and attitude when defining its commands.

The state vector of the LQR describes the deviations of the current states from a reference, which are calculated within the error calculation block. The commanded velocity of the operating point and the position controller are combined and subtracted from the current flight velocity. The attitude and thrust references are provided by the operating point of the feedforward control. The difference in attitude is calculated based on the quaternion error, see Eq. 2.4, and mapped to a deviation of the attitude in each axis. The commands of the states without explicit reference are considered with zeros.

The feedback gain K_{LQR} of the LQR is calculated individually for each operating point based on the linearization and the cost function defined in Eq. 4.4. Therefore, the feedback gain depends on the operating point and is linear interpolated using gain-scheduling. With four controls available for the velocity controller to control the three flight velocities, the system is underdetermined by one degree of freedom. The required control allocation is determined by the control effectiveness at each operating point, see Section 4.3.3. An additional, individual prioritization can be made by penalizing certain flight states and controls with the weighting matrices. The selected weighting matrices can be found in Appendix D. Since the flight characteristics vary during the transition, the weighting matrices are modified in the different flight phases.

The definition of the weighting matrix of the cross-terms enables to specifically account for limitations of the region of attraction and specify the desired control actions in each direction of the multi-axial transition. The initial roll motion is a sensitive flight phase, which requires only a small increase in roll to remain within the linear range of the lift coefficient. As identified in Fig. 4.7, the linearization of the control effectiveness of a roll angle to the acceleration $\dot{u}^{\mathrm{w}}$ is valid within a highly restricted region around the operating point. The pitch angle is equally effective, while providing significantly higher robustness in this axis. The linearization of the roll angle concerning the vertical acceleration, however, is characterized by a more accurate representation of the nonlinear function. Therefore, the roll angle is selected as the dominant control for the vertical acceleration, while pitch is better suited for the $\dot{u}^{\mathrm{w}}$ direction. The matrix N is designed accordingly to penalize the undesired flight controls in each velocity axis, therefore increasing the controller's robustness regarding the limited region of attraction in the initial roll phase.

The outputs of feedback and feedforward control are superimposed to generate the commands of the attitude and heading controllers, see Fig. 4.9. The deviations in attitude are transformed into a deviation of a quaternion for a post-rotation applied to the feedforward quaternion command. It is valid within small deviations of the attitude. The discussion of anti-windup strategies for the integral states when reaching the limits of the controls is not part of this thesis.

LQR requires full state feedback and therefore the estimation of the states that cannot be measured directly. The main challenge is the estimation of the aerodynamic velocity. A pitot tube measures the aerodynamic velocity along one axis. Since the transition includes in particular varying slip angles, a dynamically adjustable pitot tube is installed in combination with a wind vane. The wind vane measures the slip angle of the aerodynamic inflow to align the pitot tube with the aerodynamic velocity vector for accurate measurement at small angles of attack during the transition. At low aerodynamic velocities, both the wind vane and pitot tube are less accurate, and the aerodynamic velocity is estimated based on the ground velocity and the measured wind data of an external wind station. The controller is sufficiently robust to handle inaccuracies at these low velocities. Deviations of the aerodynamic velocity in the remaining two directions of the longitudinal motion are quantified by the measured ground velocity by the global positioning system (GPS). A detailed description can be found in [143]. While the attitude angles and turning rates can be measured by the inertial measurement unit (IMU), thrust and the derivatives of the angular rates and thrust are estimated from the linear state-space representation of the operating points.

4.5.2. Implementation of the Supporting Control Cascades

The velocity controller only allows for maintaining the desired velocity in all axes at each operating point and therefore relies on the surrounding control cascades for effective trajectory control of the complete transition. Each cascade is briefly explained, including the implemented control strategy and its advantages, with references to related literature providing more detailed information.

Angular Acceleration Controller

The angular acceleration (acc) controller operates at the lowest level or inner loop of the control cascade. It commands (cmd) differential thrust Δf and elevon deflection κ_i to realize the desired angular accelerations $\dot{\omega}^{\mathrm{cmd}}$. The elevon deflection results as a superposition of uniform and differential deflection κ and $\Delta\kappa$. Since direct measurements of angular accelerations tend to be noisy, they are obtained by differentiating the measured

and filtered angular rates. As the second derivative of the attitude angles, the angular accelerations are characterized by fast dynamics in response to external disturbances or modifications of flight controls. Therefore, the angular acceleration controller is designed for rapid responses with a high controller bandwidth.

An incremental nonlinear dynamic inversion controller (INDI) is implemented for angular acceleration control. INDI is an advanced, nonlinear control strategy used primarily in aerospace to handle high-frequency dynamics and achieve robust control. It builds upon the concept of nonlinear dynamic inversion (NDI) but updates the control input incrementally based on the difference between the current and desired state. For this incremental approach, it is assumed that the system dynamics compared to the control input have a neglectable influence, which is known as the time-scale separation principle. Damping effects are therefore neglected with this approach. However, it is characterized by high robustness concerning model uncertainties. [144, 145, 146, 147]

The inner control loop of the angular acceleration forms the basis of all higher-level control tasks and must fulfill high requirements in terms of robustness. In this high-frequency domain, model inaccuracies are inevitable without a detailed and computationally intensive CFD analysis. For example, the modification of the lift coefficient by an elevon deflection is approximated by nonlinear corrective terms that shift the polar of the wing to a higher or lower angle of attack [89, 18]. It neglects the effect of the current angle of attack and is based on an approximated polar by the software tool *xfoil*. The induced angular acceleration by an elevon deflection can be estimated sufficiently, but not precisely determined. Additionally, an actuator failure can occur at any time and a relocation to the remaining flight controls is necessary. At this controller level, INDI presents a well-suited tradeoff for reduced performance but high robustness, which deals with these nonlinearities and model uncertainties. Its incremental formulation allows for an adaption to real-time changes in the case of actuator saturation or failure [148].

Following the assumptions of INDI, the closed-loop transfer function of the desired angular acceleration to the actual angular acceleration is equivalent to the transfer function of the actuator dynamics [144]. It is simplified as a first-order lag element with delay for the actuators of the AWE system. This simplification is exploited to design the controller of the upper levels.

Attitude Controller

The attitude controller provides full-range attitude control from vertical to horizontal flight, ensuring stability in all flight axes. The angular acceleration command is generated

based on the attitude and rate commands from the velocity and heading controllers. For controller design, the closed-loop transfer function of the angular acceleration controller is expanded by integral states for the turning rates and the attitude angles, forming the model to set up an LQR controller with the state vector $\vec{x}_{\mathrm{LQR}} = [\delta\underline{\Phi}, \delta\omega, \delta\dot{\omega}]^{\top}$. Damping effects associated with turning rates, and coupling effects among the three flight axes are neglected in the attitude controller design. The controller is therefore independent of the current operating point. The INDI of the underlying angular acceleration controller incrementally sums up the flight controls until the desired angular acceleration is achieved. As such, no integral states of the attitude angles are required to guarantee stationary accuracy.

The singularity of the Euler angle in vertical flight requires the use of quaternions. Quaternion error control is extensively explored within tailsitter flight systems to allow for independent control in all attitudes [149, 150, 151, 117, 104]. An approach based on [73] is implemented that regulates the quaternion directly without requiring conversion to Euler angles. The error quaternion between the desired and actual attitude is calculated based on Eq. 2.4. The quaternion error can be mapped directly to a deviation of the attitude $\delta\underline{\Phi}$ in each axis of the flight system, enabling its use as part of the states in the LQR controller. The formulation of the quaternion error is valid within small attitude deviations.

Heading Controller

The design of the yaw-roll transition requires an orientation of the heading of the flight system aligned to the wind direction. In vertical, prop-borne flight, a changing direction of the wind vector leads to an aerodynamic inflow perpendicular to the wing area, which causes significant pitch moments and can result in a flight state beyond the flight envelope. In contrast, during horizontal, wing-borne flight, the wind vector is aligned to the wing area independently of the wind direction, so there are no restrictions in the flight envelope and an alignment is not necessary. The heading controller ensures that the flight path is adapted during prop-borne flight to a dynamic, rotating wind vector, while maintaining its direction in wing-borne flight.

The basic idea of the heading controller is that a rotating wind vector causes additional drag at the wing area in prop-borne flight. To maintain a constant position and zero velocity in the longitudinal axes, the flight controller must adjust the pitch axis from the vertical reference attitude around 90°. This leads to a horizontal component of the thrust vector to counteract the drag induced by the component of the wind velocity perpendicular to the wing area. Therefore, a deviation of the pitch axis from the reference attitude in no wind conditions serves as an indicator of a change in wind direction. This deviation

results as part of the outputs of the velocity controller, which is cascaded with the position controller to maintain a constant position.

The heading controller calculates the integral of the deviation between the commanded and reference pitch attitude and maps it to a heading command using a proportional gain. The deviation of measured and commanded heading is then converted with another proportional gain into a command of the related turning rates, which serves as input for the attitude controller. The implemented integration deliberately reduces the bandwidth of the heading controller to ensure that a rotation is only performed when the main wind direction changes. Response to high-frequency gusts is avoided. The approach results in a smooth, low-frequency rotation until the pitch angle returns to the reference angle when the flight system is adjusted to the new wind direction. Besides, the commanded heading is utilized for the definition of the estimated wind coordinate system.

The heading controller inherits the specific heading angle Ψ_{zxy} for the wind adjustment. The conventional heading angle Ψ_{zyx} encounters a discontinuity when reaching the singularity of the Euler angles in vertical flight, and does not remain constant during the yaw motion of the straight yaw-roll transition. It is therefore unsuited for heading control. In contrast, the 'ZXY'-sequence guarantees that the heading remains constant during prop-borne flight of a straight transition, even when the pitch angle exceeds $\Theta_{zxy} > 90°$ or the roll angle modifies with $\Phi_{zxy} \neq 0°$ due to the yaw motion. Only a deviation from this straight flight path leads to a modification of Ψ_{zxy}.

Position Controller

The position controller controls the position of the flight system in relation to the inertial frame. It receives the desired position $\vec{s}_{\mathrm{b}}^{\,\mathrm{w,cmd}}$ in the wind coordinate system from the guidance and outputs a corresponding aerodynamic velocity command $\Delta\vec{V}_{a}^{\,\mathrm{w,cmd}}$ as difference to the velocity of the current operating point V_A^{OP}. The position controller maintains a constant position in the longitudinal axes. While the velocity controller keeps the average velocity in the longitudinal axes at zero, short-term deviations from the reference velocities can lead to significant discrepancies in the desired position of the flight path. To accurately follow a straight flight path, the position controller commands slight deviations in velocity to compensate for disturbances in position. The lateral position is not actively controlled during the transition. The primary control task in the lateral direction is to achieve the target velocity, while the exact position depends on wind velocity.

The position controller is based on LQR control that incorporates the states of the position and velocity $\vec{x}_{\mathrm{LQR}} = \left[\delta\vec{s}_{\mathrm{b}}^{\,\mathrm{w}}, \delta\vec{V}_{\mathrm{G}}^{\,\mathrm{w}}\right]^{\top}$. For controller design, the model of the closed-loop

system of the velocity controller is included. This model is simplified to a first-order lag element with the Hankel norm approximation [152] to account for the relevant pole that primarily influences the low bandwidth of the position controller. A mean value for the time constant is used for the varying closed-loop systems during the transition. This allows the controller to be designed independently of the specific operating points during the transition. The command for the ground velocity is superposed with the estimated wind velocity to calculate the aerodynamic velocity command for the velocity controller.

Velocity Tracking Controller

The velocity tracking controller generates a suitable time course of the commanded velocity V_A^{OP} of the OP for the velocity controller based on the input of the target velocity V_A^{target}. The controller ensures that the maximum defined acceleration of the system for the corresponding flight phase is reached and maintained and the system remains within the given RoA. The velocity command is therefore a dynamic course based on the limits of the controller and flight system. The controller integrates the closed-loop system of the velocity controller to define a course that is precisely coordinated to the transient behavior of the system. In the presence of disturbances, such as a sudden drop in wind velocity, the controller modifies the OP by appropriately adjusting its acceleration for a stable and rapid transition within the established limits.

The velocity tracking controller is based on model predictive control (MPC). It describes a set of control strategies that utilize an internal model of the system to predict the relevant states and evaluate them by minimizing a cost function. In each sampling step, the MPC calculates an optimal sequence of control signals for the considered prediction horizon. The controller outputs the first value of this control signal sequence to the process, and the calculations are repeated in the next time step with the horizon shifted by one sampling step. It is therefore called receding horizon control. The control strategy allows the implementation of a desired reference trajectory for the system under consideration of limitations of the control signals and state variables. Yet, MPC can be computationally highly expensive, since an optimization problem must be solved at each new sampling step. [153]

MPC presents an effective control strategy for the velocity tracking controller. At this controller cascade, the bandwidth is low and the aerodynamic velocity is the only state variable. The computational effort for an online optimization is therefore reasonable. The controller imposes dynamic limits on the maximum acceleration to account for the different limits of the yaw and roll motions. Besides, the difference between the commanded and current velocity ΔV_A is limited as an indicator for the maximum RoA. In case the maximum

difference is exceeded, the velocity command is reduced such that the distance between operating point and flight state remain within the RoA. As the reference trajectory of the controller is a simple step change to the target velocity, it is explicitly desired to operate close to the constraints of the controller to proceed with the maximum acceleration in each flight phase until target velocity. Since every step is recalculated based on the integrated model of the closed-loop system of the velocity controller, the MPC can accurately respond to deviations and adapts the commanded operating point accordingly. Its implementation and a detailed description and analysis can be found in [154].

Guidance

The guidance is the upper level of the trajectory controller and is responsible for moding. Once the desired height is reached after takeoff, the lateral position control is deactivated and the target velocity is set to $13\,{}^{\mathrm{m}}/_{\mathrm{s}}$ in wing-borne flight. Based on the current flight phase, the guidance passes the associated limits and saturations of each controller cascade and therefore manages the flight operation during the transition.

5. Validation and Discussion

This chapter validates the designed launch trajectory controller. Since the design is based on the linearized consideration of the operating points, simulation and flight test results demonstrate the applicability in the nonlinear environment and under consideration of external disturbances. The simulation presents the complete yaw-roll transition from vertical prop-borne to horizontal wing-borne flight. Special attention is given to the limited flight envelope of the flight system during the yaw motion in prop-borne flight. Since the design assumes flight along the wind vector, adaptation to dynamic changes in wind direction is an essential prerequisite to achieve the desired flight operation within the flight envelope. This prevents an excessive aerodynamic velocity perpendicular to the wing area beyond stability thresholds and enables the transition from low to high wind velocities. Simulation and flight test results demonstrate the operability of the flight system in a strong wind field during prop-borne flight.

The control of the flight system in prop-borne flight in a wind field is identified as a challenging flight procedure in the results. It requires an accurate wind adjustment to minimize the external disturbances. Therefore, a detailed robustness analysis is conducted for prop-borne flight in a wind field. By specifically inserting model uncertainties, the stability of the closed-loop system is demonstrated, identifying critical parameters of oscillations and disturbances. This analysis allows to estimate the maximum wind velocity range for which the flight controller remains stable. The chapter concludes with a critical discussion of the results with respect to the original design objectives.

5.1. Simulation and Flight Test Results

Flight tests are performed with the demonstrator depicted in Fig. 5.1, showing the untethered flight system in vertical, hover flight. The results are divided into the validation of the yaw-roll transition and the wind alignment in prop-borne flight. First, the transition into wing-borne flight is validated in the simulation environment at a low wind velocity. It demonstrates the minimum wind limit of the operations and corresponds to the longest flight path with the maximum difference in aerodynamic velocity that must be achieved during the transition. Yet, gusts and the unstretched tether forces still represent a disturbance

during the transition. Second, the adaptation to a dynamic wind vector during prop-borne flight is analyzed within the simulation and flight test results. Contrary to the results of the transition, it yields at maximum wind velocity, demonstrating operability in the critical flight phase with the systems's limited flight envelope. The flight system must be properly adapted to the wind direction, solely reacting to the rotation of the main wind velocity while compensating for the high-frequency gusts without causing oscillations.



Figure 5.1.: Flight Demonstrator.

5.1.1. Yaw-Roll Transition

The yaw-roll transition is performed within the nonlinear simulation environment to validate the designed flight trajectory controller. External disturbances due to gusts, tether forces, and sensor noise are considered. In addition, the velocity tracking controller commands an appropriate acceleration from zero to the target velocity. This verifies that the stationary operating points are valid within occuring deviations from the selected trim points and that the velocity controller is able to precisely follow the commanded course of the velocity. Besides, the general stability and attitude control performance is verified.

The simulation results are shown in Fig. 5.2. Presented are the time courses of the aerodynamic velocity, the aerodynamic angles, the Euler angles $\underline{\Phi}_{yzx}$, the flight controls, and the position. The simulation is initiated with a flight system having already performed takeoff to a height of 10 m and which is located in a vertical attitude at $\Theta_{yzx} = 90°$, and $\Phi_{yzx} = \Psi_{yzx} = 0°$ with zero aerodynamic velocity. The tether length is set to 100 m to remain unstretched during the transition. The longitudinal position and velocity is maintained constant, while the lateral velocity is increased. Its maximum acceleration is set to $3\,{}^{\mathrm{m}}/_{\mathrm{s}^2}$ during the yaw motion for rapid transition to wing-borne flight. To account for the restrictive region of attraction during the roll motion, the acceleration is reduced to $0.2\,{}^{\mathrm{m}}/_{\mathrm{s}^2}$, compare with Section 4.4. The main task in this flight phase is to complete the rotation to horizontal wing-borne flight, while the aerodynamic velocity has almost reached its target

velocity. The maximum difference between the velocity command and the actual velocity is set to $\Delta V_A = 2\,\mathrm{m/s}$ in order to remain within the region of attraction, even when the wind velocity changes. The acceleration and velocity limits represent values corresponding to flight with sufficient distance to the control and stability limits for robustness and are integrated in the velocity tracking controller.

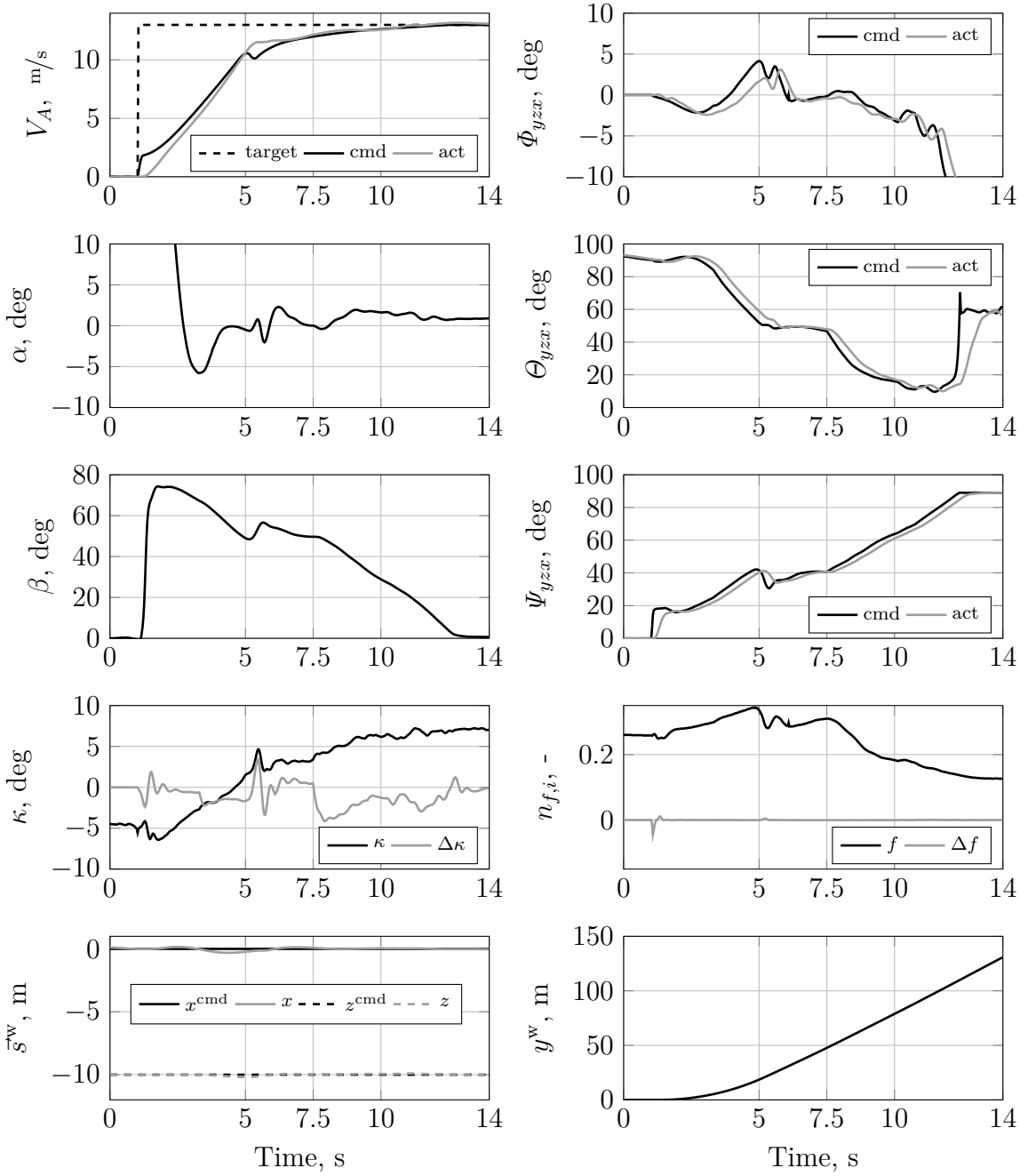


Figure 5.2.: Simulation results for the yaw-roll transition.

At $t = 1\,\mathrm{s}$, the target velocity is set from zero to $13\,\mathrm{m/s}$ in wing-borne flight. As a result,

the velocity tracking controller commands an adaptive course of the velocity command to the velocity controller, based on the limits of the maximum acceleration and difference in velocities. Initially, the command instantly increases to $2\,\mathrm{m/s}$, which is the maximum difference between commanded and actual velocity to initiate a rapid yaw acceleration. When the desired acceleration is nearly reached, the acceleration of the velocity command is slowly decreased and both the commanded and actual velocities continue at the maximum acceleration of $3\,\mathrm{m/s^2}$. At the end of the yaw motion around $t = 6\,\mathrm{s}$, the velocity tracking controller gradually reduces the acceleration of the velocity command to match the desired acceleration for the upcoming roll motion. As the controller incorporates the closed-loop system of the velocity controller as internal model, the velocity command is reduced shortly before to account for system dynamics. This ensures that the delayed actual acceleration is synchronized with the initiation of the roll motion at $t = 7.5\,\mathrm{s}$. In the final phase, the velocities further increase until the target velocity is reached.

Next to the aerodynamic velocity, the estimated aerodynamic angles are shown during the transition. The slip angle decreases steadily, closely following the selected operating points. Due to the reduction of the acceleration of the flight system at around $t = 5\,\mathrm{s}$, the slip angle briefly increases, with a subsequent linear decrease until it reaches zero in horizontal, wing-borne flight. The angle of attack has no significance at low aerodynamic velocities since it is highly sensitive and close to 90°. Therefore, the focus is placed on the range of $\alpha \in [-10°, 10°]$ to display the relevant course at the end of the yaw motion and the beginning of the roll motion. The angle of attack remains within small boundaries of 6° during this part of the transition. During the yaw motion, the velocity controller feedforwards a control command of an angle of attack of zero. However, small deviations due to the external disturbances lead to deviations from this trim path. As a result, the resulting angle of attack fluctuates around zero. The higher the aerodynamic velocity, the lower the sensitivity of the aerodynamic angle due to disturbances, and the more accurate is the tracking of the corresponding angle of attack of the feedforward command, compare with Fig. 4.6. Particularly noticeable is the discontinuity at $t = 6\,\mathrm{s}$, when the flight system reduces its acceleration. Since a reduction in thrust has a direct effect on the airflow over the wing, it affects the aerodynamic forces and thus the pitch moment and angle of attack. However, the effect is within reasonable limits. At the beginning of the roll motion at $t = 7.5\,\mathrm{s}$, the angle of attack has returned to a value close to zero. The following increase of the angle of attack corresponds to the increase of the lift force during the roll motion. The flight trajectory controller carefully increases the angle of attack without reaching the region of stall. Since the flight system is no longer in an upright attitude and the aerodynamic velocity is sufficiently high, disturbances do not cause large deviations from

the reference. Due to the decrease of the slip angle in the last flight phase, the proportion of the aerodynamic velocity u_a^{b} increases. As such, lift increases and the angle of attack can be reduced for a trimmed, horizontal flight.

The commanded attitude angles of the velocity controller show a smooth and stable transition of the flight system from vertical, prop-borne to horizontal wing-borne flight within the region of attraction of the controller. The roll angle is depicted in the relevant region of $\Phi_{yzx} \in [-10°, 10°]$. Due to the singularity of the 'YZX'-sequence at $\Psi_{yzx} = 90°$, the decrease of the roll angle starting at $t = 12\,\mathrm{s}$ does not correspond to a real rotation of the flight system and is therefore omitted to focus on the relevant part of the transition. Initially, the roll angle has low influence on the velocities since the aerodynamic velocity is low and there is no strong wind field to limit roll rotation. The roll angle is utilized to compensate for small deviations in velocity and to correct the direction of the flight path. For increasing aerodynamic velocity, it mainly determines the angle of attack and the direction of the lift force. It is zero at the end of the yaw motion and then decreases to initiate the roll motion. The pitch angle decreases continuously from 90° in vertical prop-borne flight to 0° in horizontal wing-borne flight. However, the singularity leads to a final pitch angle of 60°. When the flight system reduces its acceleration at $t = 5\,\mathrm{s}$, a plateau is reached due to the reduced rotation of the flight system in this flight phase, before the roll motion is initiated. These flight phases of acceleration and deceleration can be recognized in particular by the short rise and fall in the course of the yaw angle. Besides, its course is largely continuous, corresponding to the course of the slip angle.

The attitude and acceleration controllers effectively executes the attitude commands of the velocity controller, without large delays or oscillations. The resulting control commands are within their limits and provide sufficient control reserves for stronger disturbances or higher accelerations. The thrust-to-weight ratio $n_{f,i}$ of each propulsion unit increases initially, before decreasing during the roll motion, as calculated by the trim calculations in Fig. 4.6. Differential thrust is required specifically for the initial acceleration, while it remains close to zero during the transition. The elevon deflection increases during the transition due to the changing lift force and point of pressure. A differential deflection is mainly required to equalize the roll moments at the beginning of the roll motion at $t = 7.5\,\mathrm{s}$. Yet, it requires only a small deflection, since the lever arm of the elevons in y^{b}-direction is large and therefore their effectiveness high. The slight oscillation at $t = 6\,\mathrm{s}$ corresponds to the adjustments of thrust to reduce the acceleration and the associated changes of the aerodynamics and the overflow of the elevons in the slipstream of the propellers.

The longitudinal positions x^{w} and z^{w} are precisely maintained during the transition. The

position y^{w} results from the lateral acceleration and is not directly controlled. It ranges from $0 - 130\,\mathrm{m}$ for the complete transition to horizontal wing-borne flight.

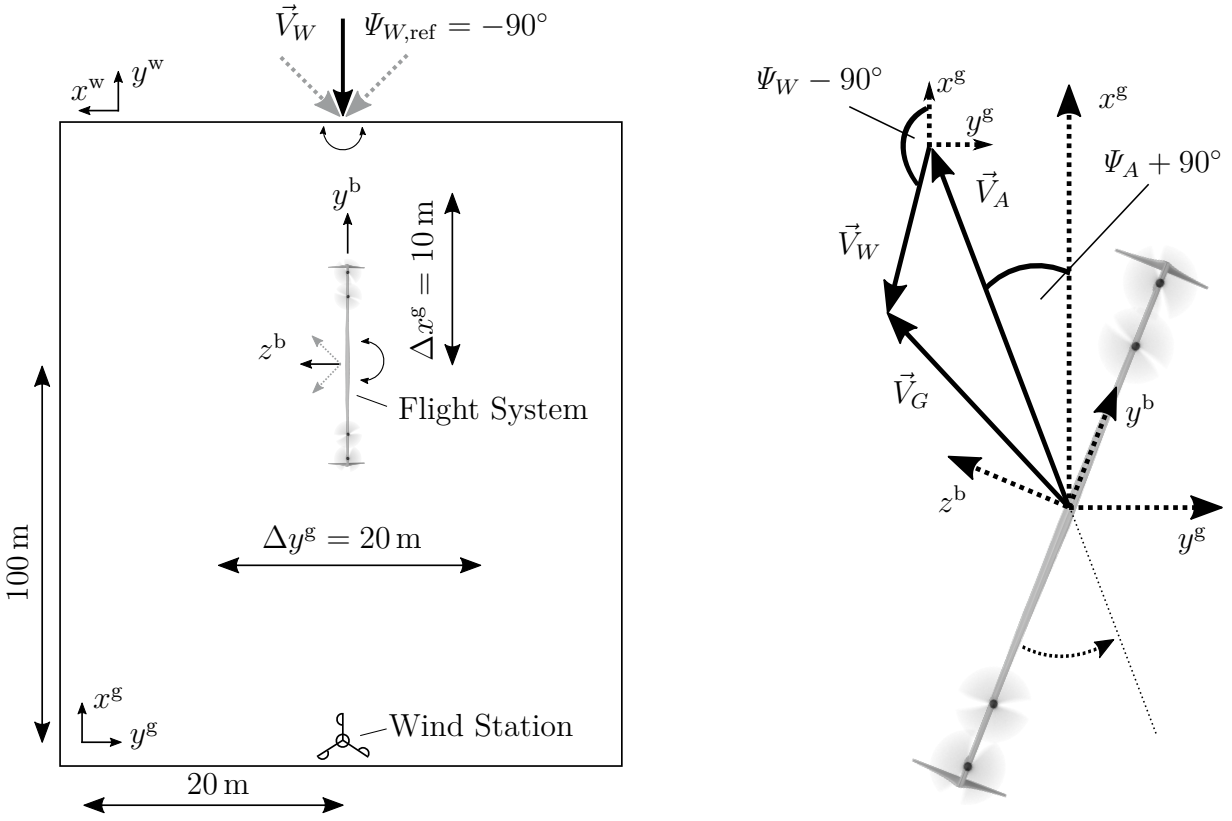
5.1.2. Wind Alignment in Prop-borne Flight

Prop-borne flight in a strong wind field significantly complicates flight control. The most challenging flight operation is vertical hover flight with zero ground velocity and high wind velocities, and therefore a minimal aerodynamic velocity for a given wind velocity. This corresponds to the flight phase where the flight envelope is strictly limited, the attitude instability is high, while the control effectiveness is low and the aerodynamic angles are highly sensitive. At the same time, disturbances due to gusts are strongest, and a rotation of the wind direction causes significant pitch moments. The flight trajectory controller must accurately adapt the flight system to the main wind direction to remain within the range of the flight envelope. Simultaneously, high-frequency gusts must be compensated for without altering the heading. Therefore, the interaction between the controller cascades must be well-coordinated for accurate wind tracking. This is verified in the following using simulation and flight test results.

To verify the controller's performance under wind conditions, the flight system hovers in prop-borne flight, while the heading controller adjusts the orientation along the wind vector. The position controller is active in all three directions to maintain a constant position. In case of a rotation of the wind vector, the velocity controller commands a deviation of the pitch angle $\delta\theta^{\mathrm{cmd}}$ from the reference, feedforward command θ^{ff} to maintain the position. In return, the heading controller commands a modification of $\Psi_{zxy}^{\mathrm{cmd}}$, as explained in detail in Section 4.5. For correct wind alignment, this heading angle must be identical to the main wind direction Ψ_W.

The top view of the basic test setup for the simulation and flight tests is depicted in Fig. 5.3a. First, the simulation results are analyzed and only the relevant aspects of this setup are outlined. The reference wind direction is from the north, corresponding to $\Psi_W = -90°$ due to the definition of the wind coordinate system. Its direction varies during the test between $\Psi_W \in [-135°, -45°]$. The flight system is positioned with its y^{b}-axis in the opposite direction of the wind vector and rotates according to the dynamic wind vector. A positive velocity u_g^{w} of the flight system corresponds to a negative deviation of the position y^{g} when aligned to the reference wind direction. Within the simulation results, the position command remains fixed.

Figure 5.4 presents the time course of the wind velocity, the heading angles, the positions x^{g} and y^{g}, the velocity u_g^{w}, and the commanded pitch angle deviation $\delta\theta^{\mathrm{cmd}}$. The wind velocity



(a) Sketch of the top view with the relevant relations of wind vector, coordinate systems, and positions of the flight system and wind station.

(b) Definition of the aerodynamic heading angle Ψ_A.

Figure 5.3.: Test setup for the simulation and flight tests.

is initiated at an average wind velocity of $\overline{V}_W = 5\,\text{m/s}$. Gust leads to a high-frequency variation of the absolute wind velocity V_W around this average value, following the wind model from Section 2.4. At $t = 20\,\text{s}$, the mean wind velocity is increased to $\overline{V}_W = 7\,\text{m/s}$. Thus, the absolute wind velocity ranges from $3 - 10\,\text{m/s}$ during the complete simulation setup. The flight system is initially orientated with the wing aligned to the wind at $\Psi_{zxy} = -90°$. In analogy to the wind velocity, the wind direction Ψ_W is a superposition of the mean wind direction $\overline{\Psi}_W$ and the gust direction. At time steps of $t = [5, 15, 30, 40]\,\text{s}$, the mean wind direction is modified by 30°, according to a first-order lag element with a time constant of $T = 0.5\,\text{s}$, corresponding to a strong dynamic rotation of the wind field. For each mean wind velocity, there are two steps of the wind direction to verify the wind adjustment in both directions and wind velocities. Note that the average wind velocity and direction do not represent the actual calculated mean values over a specific time period. Instead, they correspond to the desired average which is set as a parameter in the wind model. The wind model then calculates the resulting wind conditions by superimposing

the mean wind with gusts.

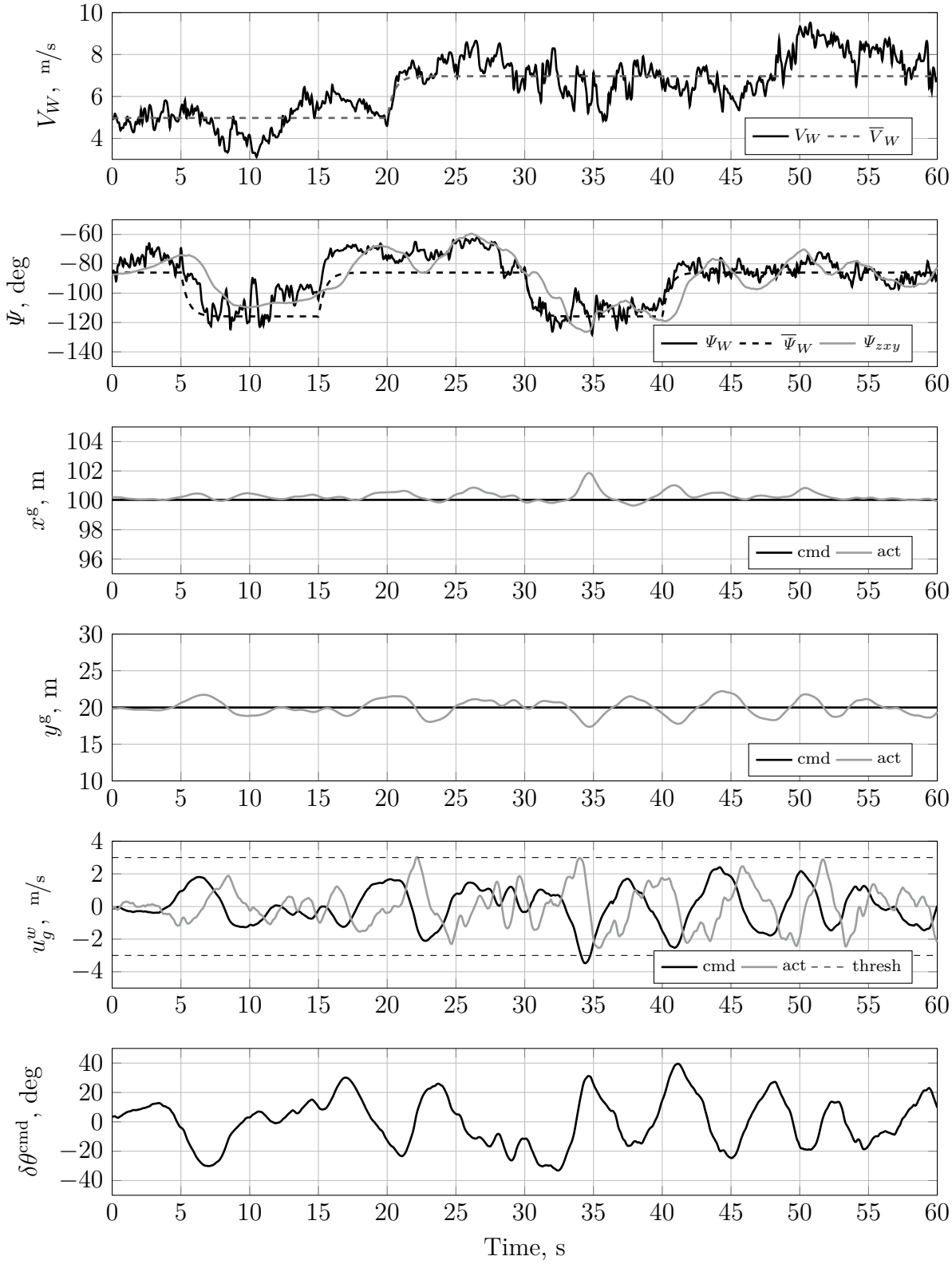


Figure 5.4.: Simulation results of the wind alignment.

The velocity u_g^{w} is a measure of the longitudinal disturbance rejection due to the wind influence. Since there is no direct measurement of the aerodynamic velocity in this direction, the ground velocity serves as an estimate of the aerodynamic velocity at low velocities. The robustness objective requires a maximum aerodynamic velocity of $3\,\mathrm{m/s}$ to remain within the flight envelope and stability region, this threshold (thresh) is depicted with a dashed line. As the position command is fixed, any change in the velocity command results solely to compensate disturbances by gusts and a rotation of the wind vector. As such, there is a phase lag of the command, which follows in this case the actual (act) value in the opposite direction, aiming for zero velocity at the initial commanded position. The resulting command of the pitch angle deviation $\delta\theta^{\mathrm{cmd}}$, generated by the velocity controller, signals the initiation of a modified heading command when it deviates from zero. A positive pitch deviation leads to a corresponding positive rotation and vice versa.

As it can be identified in Fig. 5.4, the heading of the flight system accurately follows the main wind direction. When the first step of the wind direction occurs at $t = 5\,\mathrm{s}$, the negative rotation of the wind leads to an aerodynamic inflow in negative z^{b}-direction. Due to drag, a negative velocity u_g^{w} is induced, leading to a deviation of the position y^{g}. As a result, the position controller commands a positive velocity to counteract the disturbance. The positive deviation of commanded to actual velocity results in a negative pitch command $\delta\theta^{\mathrm{cmd}}$ to compensate for the disturbance velocity. The heading command decreases to follow the changed wind direction. However, the position controller requires a subsequent positive velocity to reach the initial position after the disturbance. Therefore, the general course of the velocity is characterized by two opposite oscillations; the increase in velocity due to the disturbance and the subsequent velocity in the opposite direction to reach the initial position. At $t = 12\,\mathrm{s}$, the disturbance is compensated and the initial position is reached. At $t = 15\,\mathrm{s}$, the wind rotates in the opposite direction and the described effect is reversed.

Increasing the mean wind velocity at $t = 20\,\mathrm{s}$ generally intensifies the disturbing forces and moments. The actual and commanded velocities increase, prompting a corresponding increase in the pitch command, which leads to a faster response of the heading for wind tracking. However, a low-frequency oscillation occurs in heading, position y^{g}, and most prominently in velocity and pitch. Although the oscillation is damped and the slow period is around $7\,\mathrm{s}$, its amplitude is large and can become critical at higher wind velocities.

In general, the time lag to follow the changed wind direction is between $\Delta t = 1 - 2\,\mathrm{s}$. There is no controller response to high frequency gusts. The position can be maintained with differences around $2\,\mathrm{m}$. Despite the flight phase during the occurring oscillations, the

actual velocity consistently remains within the threshold of 3 m/s throughout the entire flight period.

The simulated flight data is further verified in a flight test. Instead of holding a fixed position, steps of the position command are initiated in both directions. The lateral position x^{g} is varied by 10 m and the critical longitudinal position y^{g} by a total of 20 m, see Fig. 5.3a. This allows to verify that the trajectory controller can realize various position commands in a dynamic wind field. More importantly, it introduces an additional aerodynamic velocity and thus enables to specifically set a desired rotation to verify the wind alignment of the flight system. Figure 5.3b illustrates this relation. It shows the top view of the flight system with the vector triangle of the aerodynamic, wind, and ground velocity. When hovering at a fixed position with no ground velocity, the aerodynamic velocity vector is the inverse of the wind velocity and the flight system is closely aligned to this wind vector. However, by commanding a ground velocity $\vec{V}_G$ unequal to zero, the aerodynamic velocity vector rotates in the direction of $\vec{V}_G$. Since the flight system aligns with the aerodynamic vector, it must rotate according to the aerodynamic heading angle Ψ_A. In this way, it is possible to verify the wind alignment of the trajectory controller without depending on a random wind course. Note that the definition of the heading angle refers to the coordinate system perpendicular to the velocity vector, thus requiring a further rotation of 90° of the depicted angles. Both angles are consistently negative throughout the test setup.

For the flight test, a small threshold around the reference attitude is added so that a rotation is only performed when the pitch command exceeds this threshold. This prevents slight rotations in a quasi-static wind field when the wind direction is nearly constant. The wind velocity and direction are measured in a wind station, positioned 100 m from the flight system in downwind direction, see Fig. 5.3a. A delay of 20 s is introduced as an estimate for the wind measurements to account for the distance between the flight system and the wind station. It is based on an average wind velocity of 5 m/s during the flight test.

The flight test results are shown in Fig. 5.5, with the same composition of flight states in the subplots as used in the simulation results. The wind velocity ranges from $3 - 7$ m/s during the flight. The aerodynamic heading is displayed instead of the wind direction, which is initially at $-50°$ and decreases to approximately $-130°$ at $t = 65$ s. A step of the position x^{g} of 10 m is commanded at $t \approx 27$ s. Due to the orientation of the wind direction and the heading of the flight system of approximately $-90°$ during that period, the wind and ground velocities are nearly aligned. This does not result in a modification of the aerodynamic heading and only increases the lateral, aerodynamic velocity. Within

the time range of $t = 0 - 65\,\mathrm{s}$, the aerodynamic and wind directions are therefore nearly identical. However, at the time steps of $t = [65, 80, 95]\,\mathrm{s}$, several steps of the position y^{g} are commanded. This leads to a corresponding command of the velocity u_g^{w} and increases the aerodynamic heading for a positive modification of the position.

The heading of the flight system Ψ_{zxy} follows precisely the measured aerodynamic heading in the flight test. Gusts do not negatively affect the course of the heading. The position and associated velocity commands are effectively realized within a sufficient time range, while the disturbances due to wind do not cause large deviations. The modification of the aerodynamic heading due to the position command in y^{g} is successfully tracked by the flight system.

The velocity u_g^{w} remains within the threshold of $3\,\mathrm{m/s}$, even during the initialization of position commands. However, at $t = 35\,\mathrm{s}$, the threshold is reached for a short time. Between $t = 30 - 40\,\mathrm{s}$, a high-frequency oscillation occurs, primarly affecting pitch and the velocity u_g^{w}. This occurs when the position controller commands a step change in position, causing an increase in aerodynamic velocity. The resulting oscillations lead to temporary deviations from the velocity and position commands until the system restabilizes and the oscillation subsides. Since the integration of the pitch angle to command a turning rate acts as a low-pass filter, the heading remains unaffected by the oscillation. At $t = 52 - 65\,\mathrm{s}$, the wind vector is largely constant, leading to no disturbance and therefore a pitch command below the threshold for a rotation of the flight system.

A comparison of the flight test and simulation results reveals that in both scenarios, the trajectory controller successfully aligns the flight system with the wind and effectively suppress the disturbing velocity u_g^{w}. However, the wind velocity is generally higher in the simulation and steps of the wind direction more distinctive, generating more pronounced pitch moments compared to the flight test. Consequently, the simulation shows greater disturbances in the velocity u_g^{w} and a more significant low-frequency oscillation. Conversely, high-frequency oscillations in pitch are observed only in the flight test results. These oscillations are likely amplified by the low inertia of the flight system around the pitch axis. This makes it susceptible to disturbances that can more easily excite the natural frequencies during flight. Such oscillations are absent in the simulations, likely due to discrepancies between the model and the real-world dynamics.

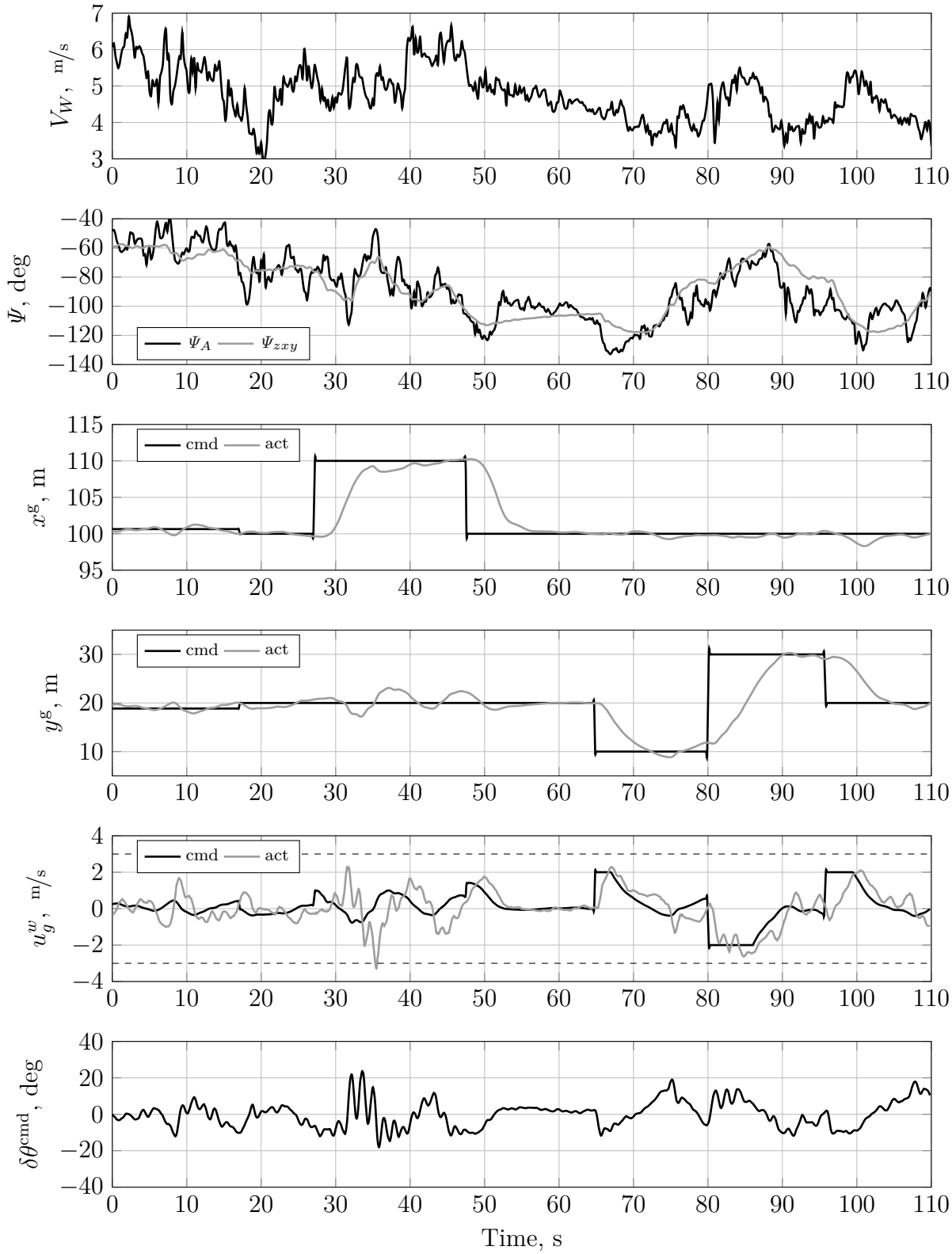


Figure 5.5.: Flight test results of the wind alignment.

5.2. Robustness Analysis of the Wind Alignment

Wind alignment during prop-borne flight in a strong wind field is identified as a highly challenging flight phase. It is crucial to remain within the strictly limited flight envelope of the pitch motion. The time to double of the instability of the flight system's pitch attitude is short and disturbances due to deviations from the correct alignment of wing area and wind vector cause significant downpitch accelerations. Disturbances increase quadratically with wind velocity and penalize delayed tracking of the wind vector, complicating significantly the control task. It requires a well-balanced tuning of the launch trajectory controller to adjust the orientation of the flight system without causing oscillations. The robustness analysis therefore focuses on the interaction between the controller cascades for wind alignment in prop-borne flight. In analogy to the simulation and flight test results, vertical flight with low ground velocity and strong wind influence is considered as the worst-case scenario.

The mode of action of the controlled system for wind alignment can be broken down to the following principle: A rotation of the wind vector causes a pitch acceleration and a deviation of the longitudinal velocity, which in return causes a modification of the command of the pitch angle. This initiates a roll rotation of the flight system to re-align with the wind vector. Accordingly, the pitch and roll motions of the flight control system in a wind field are coupled, and it requires a connected closed-loop system to cover the system dynamics. In contrast, the yaw motion remains largely decoupled, since it is primarily responsible for lateral acceleration and is therefore not considered.

In the following, an analytical model is presented, designed to capture and replicate the observed dynamics. This model simplifies the system of the pitch-roll motion by reducing it to a few key parameters. For each parameter, precise upper and lower bounds can be established, providing well-defined system uncertainties. These uncertainties allow to determine the range of the system dynamics and capture the worst-case gains that lead to a maximum aerodynamic velocity u_a^{w}. A high aerodynamic velocity in this direction must be avoided due to the limited flight envelope and region of attraction of the flight trajectory controller, designed for a velocity of $u_a^{\mathrm{w}} = 0\,\mathrm{m/s}$. The system is verified to prove consistency with the oscillations identified in the simulation and flight test results. Additionally, the system can be linearized for various wind velocities, allowing to analyze the closed-loop behavior and its robustness across a range of wind conditions and model uncertainties. In particular, this approach allows the derivation of limits for the maximum wind velocity at which the designed flight trajectory controller remains operable.

5.2.1. Simplified Model of the Pitch-Roll Motion

To analyze the dynamics of the flight system, an analytical model of the closed-loop system for vertical flight in a wind field is derived. It takes into account the relevant forces and moments that mainly affect the coupled pitch-roll motion. Figure 5.6 depicts the structure of the closed-loop system, showing the coupling of both motions due to the wind field and the relevant control cascades.

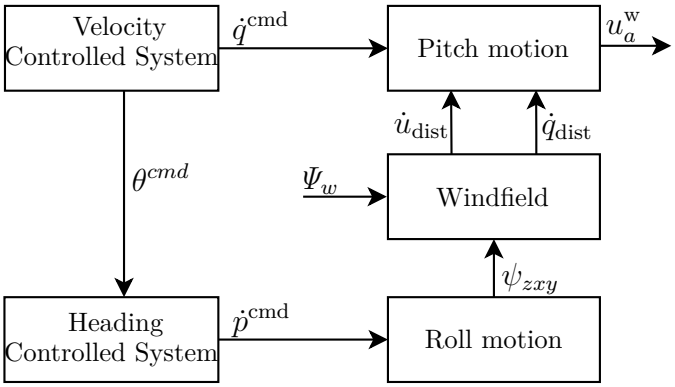


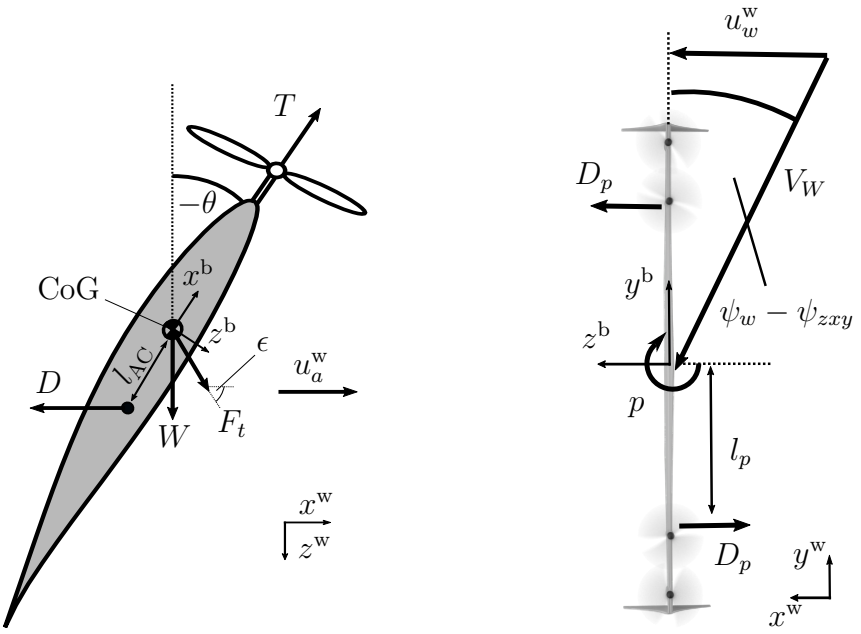
Figure 5.6.: Structure of the closed-loop system of roll and pitch motion during wind alignment for the robustness analysis.

The focus is on the velocity and heading controllers, as the low bandwidth of the position controller has reduced effect on the overall dynamics. Besides, a fixed operating point at $V_A^{\mathrm{OP}} = 0\,\mathrm{m/s}$ is assumed, with no influence from the velocity tracking controller or the yaw motion. Deviations from this operating point due to increased aerodynamic velocity are addressed in the uncertainty estimation. Considering the complete flight trajectory controller, the lowest control cascade is the angular acceleration controller to transform angular acceleration commands into control inputs of the elevons, see Fig. 4.9. Due to its nonlinear behavior, its stability in the presence of external disturbances can be analyzed using Lyapunov methods [155]. However, within the range of this thesis, it is assumed that the angular acceleration commands are realized following the linear transfer function of the actuator dynamics. This is valid for a sufficiently accurate modeling of the control effectiveness, the applicability of the time-scale separation, and within the limits of the control inputs [144]. Pitch and roll accelerations are therefore represented by a first-order lag element of the actuator dynamics, see Eq. 5.1. A dead time is omitted, its phase shift must be considered as part of the stability reserves in the evaluation of the closed-loop system. The angular rate and attitude angles are obtained by integration.

$$G_{\dot{\omega}^{\mathrm{cmd}} \rightarrow \dot{\omega}^{\mathrm{act}}} = \frac{K_{\dot{\omega}}^{\mathrm{DC}}}{1 + T_e s} \tag{5.1}$$

The transfer functions of the closed-loop systems are formulated in a continuous-time representation. The similarity to the discrete-time representation is given when the sampling frequency is higher than 20 times the maximum bandwidth of the controller [156]. With a sampling frequency of 200 Hz, the attitude controller as the lowest cascade at around 2 Hz fulfills this condition (assuming the simplification of the angular acceleration controller).

The state-space representations of the linearized models are analytically determined for the pitch and roll motions, and the dynamics of the wind field. To derive the correlation of the induced accelerations by a modification of pitch and roll motions, the principle of linear and rotational momentum is applied. Figure 5.7 depicts the forces and velocities acting during vertical flight in a wind field. Capturing all relevant effects is crucial to accurately represent the primary influences during this flight phase. The analysis considers a flight state deviating from the reference pitch angle of 90° and an alignment of wing area and wind vector. For the purposes of this analysis, the wind velocity is assumed to be time-invariant.



(a) Pitch motion. (b) Roll motion.

Figure 5.7.: Relevant forces and velocities acting during vertical, prop-borne flight in a wind field.

Regarding the pitch motion, as shown in Fig. 5.7a, the corresponding linear momentum equation in the x^{w}-direction is derived in Eq. 5.2. The relevant aerodynamic force is drag D, acting at the aerodynamic center (AC). In component notation, it includes the density ρ, wing area S, mass m, and drag coefficient C_w, simplified by the constant C_u. It is

proportional to the square of the aerodynamic velocity, which can be expressed as the difference between ground and wind velocities. In vertical hover flight, the lift forces are significantly smaller in comparison and are neglected. Besides, the components of thrust T and the tether force F_t are acting in the x^{w}-direction. Thrust is approximately equal to weight and is therefore simplified to gravity g.

$$\begin{aligned} m \cdot \dot{u}_g^{\mathrm{w}} &= -T \cdot \sin\theta + F_t \cdot \cos(\epsilon) - D \\ \Leftrightarrow \dot{u}_g^{\mathrm{w}} &= -g \cdot \theta + \frac{F_t}{m} - \underbrace{\frac{\rho \cdot S \cdot C_w}{2 \cdot m}}_{C_u} \cdot \left[u_g^{\mathrm{w}2} - u_w^{\mathrm{w}2}\right] \end{aligned} \tag{5.2}$$

Considering the angular acceleration of the pitch motion, the induced pitch moment due to drag is the dominant quantity, see Eq. 5.3. In vertical flight, the angle of attack of the aerodynamic velocity is around $\alpha = 90°$, so the position of the AC is approximately at the centroid of the wing area. Since the tether force and weight act through the CoG, they do not contribute to a pitch moment. A damping effect by a pitch rotation is neglected due to the small lever arm of the chord length. The drag force is again rewritten in component notation and its constants substituted by C_q.

$$\begin{aligned} I_y \cdot \dot{q} &= -D \cdot l_{\mathrm{AC}} \cdot \cos\theta \\ \Leftrightarrow \dot{q} &= -\underbrace{\frac{\rho \cdot l_{\mathrm{AC}} \cdot S \cdot C_w}{2 \cdot I_y}}_{C_q} \cdot \left[u_g^{\mathrm{w}2} - u_w^{\mathrm{w}2}\right] \end{aligned} \tag{5.3}$$

Within the roll motion, the roll damping is the dominant force, see Fig. 5.7b and Eq. 5.4. The roll damping is approximated by the drag D_p, induced by the angular velocity $u_p = p \cdot l_p$. For the angular velocity, the mean value at the length of 2/3 of the half span is assumed. The lever arm has therefore cubic influence on the damping. Compared to the pitch motion, the lever arm of the span width is significantly larger than the chord length. The damping is therefore included in the consideration of the angular acceleration. The roll moment induced by the lift force due to sideslip is neglected, since the propellers and winglets partly shadow the lateral aerodynamic inflow in this vertical flight attitude. This assumption holds in low to intermediate wind velocities but requires to be considered in high wind conditions. The constants are substituted by C_p.

$$I_x \cdot \dot{p} = -2 \cdot D_p \cdot l_p = -\frac{\rho \cdot S \cdot C_w \cdot l_p}{2 \cdot I_x} \cdot u_p^2 \tag{5.4}$$
$$\Leftrightarrow \dot{p} = -\underbrace{\frac{\rho \cdot S \cdot C_w \cdot b^3}{54 \cdot I_x}}_{C_p} \cdot p^2$$

The aerodynamic velocity is the result of the combined ground and wind velocities. The wind velocity u_w^{w} consists of the x^{w}-component of the absolute wind velocity, see Eq. 5.5 and Fig. 5.7b. It can be induced either by a rotation of the wind direction ψ_W or by a rotation of the heading of the flight system ψ_{zxy}. An increase in wind velocity for a slightly deviated alignment of flight system and wind vector also modifies the disturbing accelerations. However, compared to rotational changes, this influence is minimal, especially at higher wind velocities. Therefore, the wind velocity is not considered a linearization variable. The proportion of the accelerations due to the wind velocity are the disturbing accelerations $\dot{u}_{\mathrm{dist}}$ and $\dot{q}_{\mathrm{dist}}$ of the wind field, as depicted in Fig. 5.6.

$$u_w^w = V_W \cdot \sin(\psi_W - \psi_{zxy}) = V_W \cdot (\psi_W - \psi_{zxy}) \tag{5.5}$$

For all equations, the small-angle approximation is utilized for simplification of the trigonometric functions. The equations are linearized for small deviations around the linearization point denoted by the index 0. Its values are summarized in Table 5.1. The vertical pitch attitude is denoted by $\Theta_0 = 0°$ due to the modified definition of the reference, see Fig. 5.7a. The heading angles are deviated to account for the forces induced by the wind velocity, which is not exactly aligned with the wing. A difference of 30° is assumed, corresponding to the steps in wind direction within the simulation results, compare with Fig. 5.4. Accordingly, the roll rotation is set to $p_0 = 10\,°/\mathrm{s}$ to account for a typical roll rate during wind alignment. The ground velocity is set to $u_{g,0} = 1\,\mathrm{m/s}$ to account for drag. The wind velocity of the linearization point is the crucial value for the robustness analysis. Its value is varied in a range of $1 - 12\,\mathrm{m/s}$ to analyze the linear flight behavior with respect to different wind velocities.

States	Θ_0	T_0	$\Psi_{W,0}$	$\Psi_{zxy,0}$	p_0	$u_{G,0}$	$V_{W,0}$
Value	0°	W	30°	0°	$10\,°/\mathrm{s}$	$1\,\mathrm{m/s}$	$[1-12]\,\mathrm{m/s}$

Table 5.1.: Linearization point.

The linearization of the linear and rotational accelerations is performed for each state variable $\vec{x} = [u, \theta, q, \psi_{zxy}, p, \psi_W]^\top$. The tether force is largely constant for the unstretched tether and only changes due to modifications of the flight system's position. It is therefore eliminated in the linearization. The linearization is transformed into a state-space representation, see Eq. 2.7. The flight system's motion is controlled by the attitude, velocity, and heading controllers, the linearization is therefore extended by their states and feedback gains. The resulting state-space representation of the roll and pitch controlled systems including the windfield are given in Appendix D. Both systems are connected via the pitch command and the heading ψ_{zxy}. Since the task of the velocity controller in the longitudinal direction is to provide suitable disturbance rejection instead of accurate command step response, a velocity command as input is not considered in the robustness analysis and the only input is a disturbance of the wind direction ψ_w. The output of interest is the velocity u_a^{w}, as it is the decisive value that requires to meet the robustness limits of $3\,{}^{\mathrm{m}}/_{\mathrm{s}}$ to remain within the flight envelope of trimmed states and the region of attraction of the designed velocity controller.

5.2.2. Uncertainty Estimation

The linearized closed-loop system is extended to account for expected parameter uncertainties. Capturing all relevant deviations is crucial to accurately reproduce the full spectrum of the system's dynamics. However, overly broad uncertainty estimates are counterproductive, as they can significantly increase the solution space, leading to results that deviate substantially from the real dynamics. In the following, a systematic approach for the implementation of uncertainties is presented. Each parameter is analyzed for potential deviations, and an appropriate uncertain model is developed for the closed-loop system. Within the scope of this thesis, uncertainties arising from the sensor system and filters are not considered. These factors typically introduce additional phase shifts and therefore require consideration within the evaluation of the system's overall phase margin.

For the uncertain system, worst-case gains are calculated using the H_∞-norm, which quantifies the maximum singular value of the system's transfer function across all frequencies [157]. The worst-case gains are evaluated with respect to the maximum output of the velocity u_a^{w} due to a wind vector rotation ψ_w, serving as a measure of the largest aerodynamic velocity across frequencies induced by wind disturbances.

Table 5.2 depicts the selected parameters of the simplified model of the pitch-roll motion for which uncertainties are assigned. It can be reduced to six relevant uncertainties. Next to their nominal values, the upper and lower bounds of the uncertainties are denoted, as

well as the worst-case gains. The bounds and worst-case gains define the percentage of the deviation from the nominal value.

Parameter	Nominal	Upper Bound	Lower Bound	Worst-Case Gain
$K_{\dot{\omega}}^{\mathrm{DC}}$	1	+10 %	−70 %	−70 %
T_e	0.01 s	+200 %	−10 %	+200 %
g	9.81 m/s²	+40 %	−10 %	+40 %
C_D	1.6	+25 %	−25 %	+25 %
l_{AC}	0.15 m	+20 %	−20 %	+20 %

Table 5.2.: Parameter uncertainties.

The transfer functions of the angular accelerations are implemented with the largest uncertainties. Due to the nonlinear behavior of the INDI, its time-scale principle, and the high bandwidth of this controller cascade, the linear transfer function is a strong simplification of the real dynamics. It allows a sufficient approximation of the higher order dynamics, but accepts deviations from the actual system. However, within the framework of the flight tests, an estimation of the deviations can be accurately determined, compare with [147]. A detailed description of this process is beyond the scope of this thesis. The uncertainties of the time constant T_e and static gain $K_{\dot{\omega}}^{\mathrm{DC}}$ of the transfer functions of the actuator dynamics are widely similar for pitch and roll motions due to the identical elevon actuator. Therefore, the same parameter uncertainties are implemented for both motions. According to the robustness requirements in the design process of the INDI, the model overestimates the actual flight behavior [147]. Accordingly, the upper bound of the static gain is narrow, while the lower bound has to capture strong deviations from the nominal value. Regarding the time constant, this relation is reversed and the broad, upper bound corresponds to the slowest actuator. Uncertainties due to an actuator with higher order dynamics are not considered.

In Eq. 5.2, gravity g is used as a simplification for thrust. However, thrust does not exactly equal weight. During yaw and pitch motions, the thrust vector is no longer aligned to the weight vector, and thrust must be increased. Additionally, the vertical component of the tether force requires to be equalized by thrust. Consequently, the tendency of thrust is to be higher than weight. The lower bound is therefore set narrow at −10 %. During the yaw motion of the transition, thrust increases by a maximum of 15 %, according to the trim calculations in Fig. 4.6. For a deviation of the pitch angle of approximately 30° to balance disturbances, it must increase by an additional 15 %. The tether force is estimated to be a maximum of 10 % of the weight, compare with Section 2.4.2. By considering a linear combination of these uncertainties, the overall upper bound for thrust is approximately +40 %.

Regarding drag, the drag coefficient C_D is a function of the Reynolds number, the aerodynamic angles, and the geometry. The drag coefficient of a flat plate with a perpendicular aerodynamic inflow is assumed. According to experimental data, its value ranges from 1.2 to 2.0 [158, 159]. Therefore, the nominal value of 1.6 is selected with the corresponding upper and lower bounds. The point of attack is at the aerodynamic center, with distance l_{AC} to the CoG. Its location is in the centroid of the wing. Yet this is an assumption that deviates for example with respect to the angle of attack, according to Fig. 2.8. A reasonable bound of 20 % in both directions is selected as uncertainty.

The remaining parameters of the pitch-roll model are determined by uncertainties less than 10 %. This includes density, wing area, and span. Besides, the mass of the flight system is accurately measured, while the moment of inertia is calculated and validated within a swing test according to [160]. The values can be found in Appendix D. Within the range of this validation, no further additive uncertainties are included for unmodeled forces and moments. In particular, the lift force becomes increasingly important above $V_A = 10\,\mathrm{m/s}$, following the course of the lift factor in Fig. 4.6. As the robustness analysis primarily focuses on wind conditions up to $10\,\mathrm{m/s}$ based on the wind data in the simulation and flight test results, the lift forces are not further considered within this analysis.

For each uncertainty, the worst-case gains that lead to the highest velocity u_a^{w} due to a wind vector rotation are presented in Tab. 5.2. The worst-case gains of the actuator corresponds to an actuator with the worst effectiveness and therefore with the lowest bandwidth and static gain. While this actuator model is robust regarding the INDI design of the angular acceleration cascade, it also results in the worst command response. The relating commands take the most time and largest elevon deflection to be realized. This affects the attitude and velocity control cascades, being designed based on a faster assumption of the command response of the angular accelerations. The worst-case gain regarding thrust is the upper bound. Due to a deviation of the vertical attitude, high thrust leads to high accelerations in the x^{w}-direction. The velocity u_a^{w} is therefore more sensitive to a flight with higher thrust. Concerning drag, the worst-case corresponds to the largest drag coefficient and lever arm. This leads to the largest pitch moments induced by an aerodynamic inflow, which in return increases the acceleration due to thrust.

5.2.3. Model Verification

The uncertain closed-loop system is verified in the following. At first, the range of the deflection of the elevons is estimated to ensure that they remain within their limits in the case of maximum disturbance. This is necessary to compensate for the disturbance and

is one of the conditions for simplifying the closed-loop system of angular accelerations as the transfer function of the actuator dynamics. Subsequently, the poles of the connected closed-loop system of the pitch-roll motion are analyzed. The frequencies of the occurring oscillations are compared with the dominant frequencies of the simulation and flight test results of the wind alignment in prop-borne flight to verify the correct frequency domain of the poles. Within the range of this analysis, the non-oscillating poles are not further verified.

The elevons are required to trim the longitudinal motion and achieve the necessary accelerations for rapid transitions, while also maintaining sufficient reserves to adjust the flight system's heading and stabilize its pitch and roll attitudes during external disturbances. The focus is placed on disturbance rejection in the critical pitch axis. Under static conditions, the flight system reaches the limits of its trim range at $u_a^{\mathrm{w}} = 3\,\mathrm{m/s}$, compare with Fig. 3.2. However, it shall be assessed whether a dynamic disturbance of $3\,\mathrm{m/s}$ during vertical flight can be stabilized by the elevons. Assuming a deflection of 10° for both trim and control of the flight system (compare with Fig. 4.6), along with another 10° for roll motion and stabilization, there is a remaining 10° for disturbance rejection in pitch.

Figure 5.8 depicts the absolute value of the pitch accelerations resulting from a disturbance of $\Delta u_a^{\mathrm{w}} = 3\,\mathrm{m/s}$ and an elevon deflection of 10°. The disturbance induces an initial pitch acceleration according to the linearized value as calculated in Section 4.3.3. Its effect increases, following the time to double amplitude of the unstable pitch pole, as analyzed in Fig. 3.3. The elevon response is delayed and produces an opposing pitch acceleration, according to the time constant of the actuator and the effectiveness of the linearization in the pitch axis. The disturbance generates a pitch rate represented by the area A_1 between the two curves of the pitch acceleration. At the intersection point, the elevon begins to reduce the pitch rate until it is completely equalized when both areas A_1 and A_2 become identical. As the area A_2 exceeds A_1, the elevon can successfully compensate a dynamic disturbance of $\Delta u_a^{\mathrm{w}} = 3\,\mathrm{m/s}$. However, it becomes evident that the limit towards higher disturbances is almost reached. To extend the range, it requires an actuator with reduced delay, a lower time constant, greater effectiveness, or a larger deflection reserve for disturbance rejection. Note that the acceleration due to the disturbance corresponds to a continuous aerodynamic velocity of $u_a^{\mathrm{w}} = 3\,\mathrm{m/s}$. A realignment of the flight system in wind direction by the heading controller reduces the aerodynamic inflow and supports the reduction of the pitch acceleration. Besides, it is based on simulation data and requires additional verification through flight tests. Nonetheless, it highlights the challenge and significance of disturbance rejection in the pitch axis.

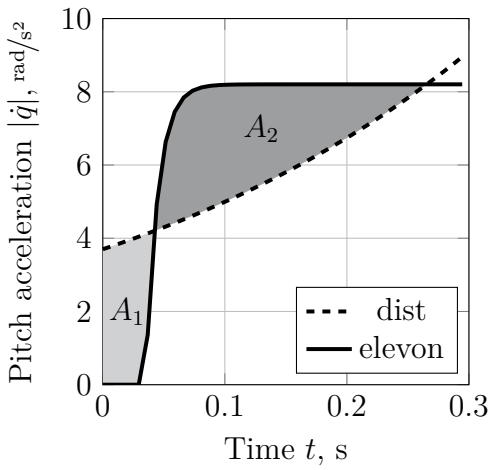


Figure 5.8.: Dynamic stabilization of the maximum disturbance by an elevon deflection.

In the following, the poles of the uncertain closed-loop system are assessed to evaluate the dynamics of the pitch-roll coupling. The introduction of model uncertainties results in a spectrum within which the poles are distributed. To sample all relevant pole locations, several probabilistic, heuristic, or analytical approaches exist [161]. A commonly utilized technique is parameter gridding, in which each uncertain parameter is varied in small, equalized steps within its bounds around the nominal value to sample pole locations for all combinations. This gridding process increases the computational effort exponentially by the number of parameter uncertainties. However, since the uncertain model of Section 5.2.1 defines a limited number of six uncertainties, this approach is suitable for the uncertain closed-loop system of the pitch-roll motion. An uncertainty envelope is generated, representing the outer limits of the real and complex values of the uncertain pole locations, similar to [161, 162]. This approach provides the upper and lower bounds of the possible frequencies and damping constants of the closed-loop poles. The focus is placed on the uncertainty envelope of the poles that are capable of oscillating.

Figure 5.9 depicts the exact pole locations of the closed-loop system relating to the nominal values and corresponding to a linearized wind velocity of $5\,^{\mathrm{m}}/_{\mathrm{s}}$, similar to the wind velocity during the flight test and simulation results, compare with Fig. 5.4 and Fig. 5.5. The range is limited to a frequency of 2 Hz and therefore omits the poles corresponding to the actuator dynamics around 100 Hz, which are not relevant for the following analysis. The uncertainty envelope related to the outer bounds of the pole locations is marked, based on the uncertainties as introduced in Tab. 5.2.

Regarding the nominal poles, there are two different, oscillating pole pairs with a frequency of approximately 1.6 Hz. Due to their proximity, the uncertainty envelopes of the two pole

pairs are nearly coincident, and for simplicity, only the outer border of both envelopes is marked. There are three poles on the real axis, of which the two poles corresponding to the higher corner frequency are capable of oscillating when inserting the uncertainties from the nominal value. Due to their low bandwidth, the uncertainty envelope is significantly smaller and the relevant area is zoomed in for a better visualization. The exact values of the poles, the frequency and damping, and their corresponding eigenvalues are listed in Appendix D. The eigenvalues are utilized to identify the dominant flight states of each pole. Although the poles have dependencies in all flight states due to the coupled closed-loop system, there are dominating states that allow the pole to be assigned to the corresponding flight state and control cascade.

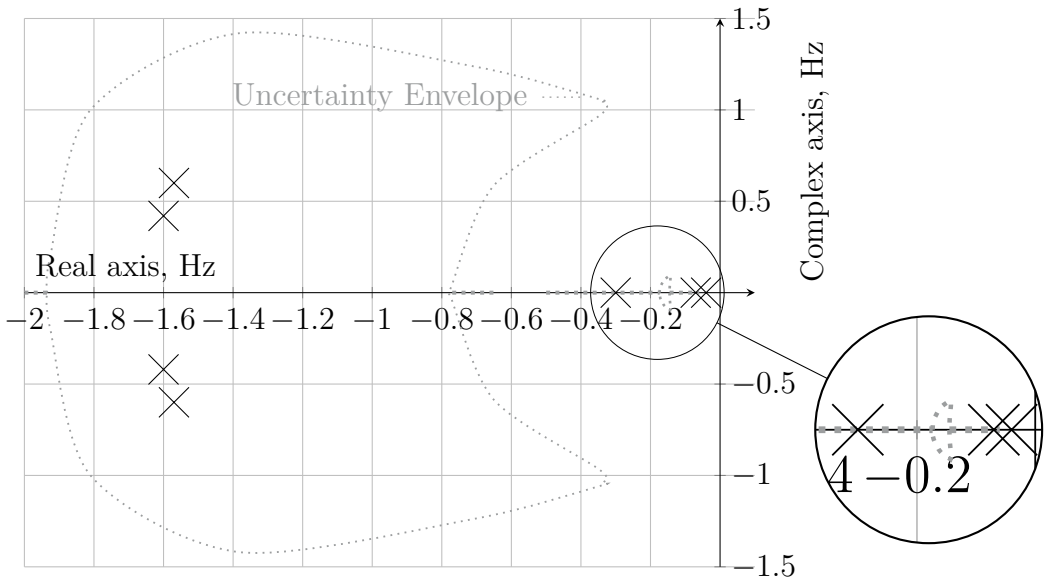


Figure 5.9.: Poles of the closed-loop system with nominal values and the uncertainty envelope of the oscillating poles.

The two oscillating, but well-damped nominal poles correspond to the bandwidth of the attitude controller, having eigenvalues with dominant states in the accelerations and rates of pitch and roll. The design of the attitude controller and the underlying model are similar for roll and pitch, leading to nearly identical poles. Due to the uncertainties, the frequency and damping of both pole pairs vary significantly. While the range of the frequency is between approximately $0.8 - 2\,\mathrm{Hz}$, the damping constant ranges between $0.35 - 1$. A damping of 0.35 is critical and can lead to oscillations, requiring a more robust tuning of the attitude controller in case the associated uncertainty can be confirmed.

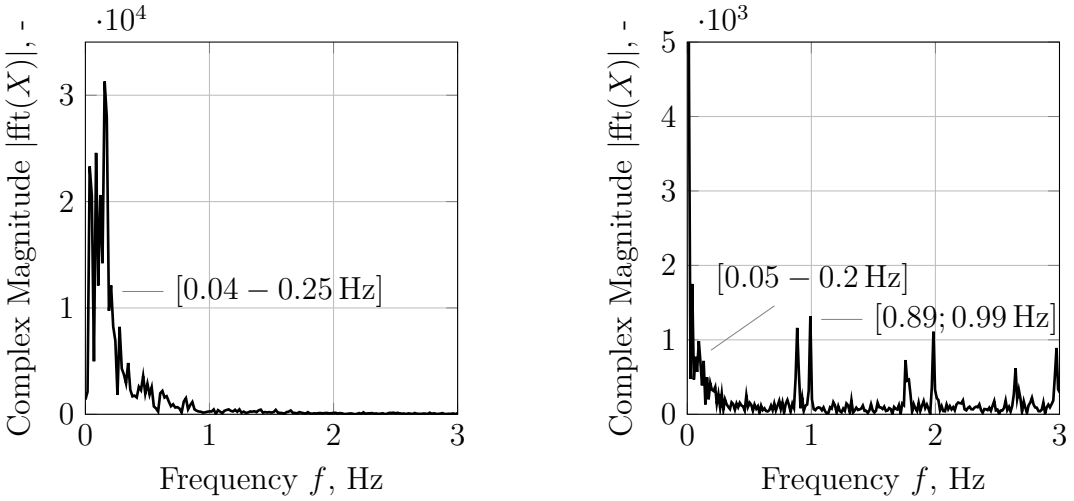
The non-oscillating pole at a frequency of 0.3 Hz has its dominant state in the velocity u_g^{w} and therefore corresponds to the bandwidth of the velocity controller. The pole is closely

related to the pole next to it at a frequency of 0.07 Hz. It belongs to the bandwidth of the heading controller, which integrates the pitch command input to command a change in heading, see Section 4.4. Within the range of the uncertainties, both poles can oscillate, yet with a low frequency around $0.15 - 0.17$ Hz and with a high damping constant between $0.85 - 1$, see the magnified extraction of Fig. 5.9. These poles therefore accurately describe the coupling of pitch and roll motion, since heading, pitch, and velocity are all relevant part of the eigenfrequencies. The non-oscillating pole close to the complex axis belongs to the integrated state of the velocity for stationary accuracy. It is therefore of less interest for the pitch-roll coupling.

The poles of the closed-loop system emphasize the cascaded control structure of the flight trajectory controller. There is a clear separation of the bandwidth of each cascade. The attitude controller performs its commands at the highest frequency, with a successive reduction of the bandwidth of the velocity controller and the heading controller.

In order to verify the oscillating poles of the closed-loop model and assess the valid range of the uncertainties, a Fourier analysis is conducted for the simulation and flight test results of the wind alignment (compare with the time courses in Fig. 5.4 and Fig. 5.5). A Fourier analysis decomposes a signal into a sum of sinusoidal components, revealing the signal's frequency content and amplitude at each frequency [163]. The analysis is conducted for the time course of the pitch angle command in the entire time range of the simulation and flight test data. It outlines the dominant frequencies of occurring oscillations for comparison with the frequency domain of the oscillating poles of the pitch-roll model as recognized in Fig. 5.9. Since the pitch angle has components in all eigenvalues of the relevant poles, it is therefore a suitable representative in which all oscillations are visible.

Figure 5.10a presents the Fourier analysis of the simulation results. While the higher frequency oscillations associated with the attitude controller are not excited, a distinct peak is observed in the frequency range of $0.04 - 0.25$ Hz. At these low frequencies, oscillations are less sharply defined with respect to frequency, since disturbances during flight have a longer time period to interfere with the excited natural frequency. Yet, the oscillation can be attributed to the pitch-roll coupling at approximately 0.16 Hz, as identified in the uncertainty analysis of the closed-loop system. This oscillation corresponds to the behavior observed in particular in the time interval of $t = 35 - 55$ s of Fig. 5.4. The oscillation is evident not only in the pitch command but also in the time course of the velocity u_g^{w}, the associated position y^{g} and the coupled heading Ψ_{zxy}. These low-frequency oscillations exhibit high amplitudes and are only weakly damped, indicating that the damping in the robustness analysis is overestimated. This can be traced back for example to unestimated



(a) Simulation data.

(b) Flight test data.

Figure 5.10.: Fourier analysis of the pitch angle command.

deviations in the modeling of the damping terms, unmodeled forces, or the neglected dead time and delay due to the filter for the measured data. More importantly, the oscillation occurs mainly in the flight phase at increased wind velocity of 7 m/s, where it is amplified due to the deviation from the linearization velocity of 5 m/s.

According to the Fourier analysis in Fig. 5.10b of the pitch angle command of the flight test results, the low-frequency oscillation of the pitch-roll coupling is recognizable in the frequency domain of $0.05 - 0.2\,\text{Hz}$. However, this oscillation is noticeably less pronounced than in the simulation results, since the wind velocity is especially in the flight phase starting from $t = 50\,\text{s}$ widely below 5 m/s, therefore reducing the effect of the coupling terms due to wind. Nevertheless, its presence is visible for example in the time range of $t = 30 - 50\,\text{s}$ in Fig. 5.5. The wind velocity is around 5 m/s, while the step in the position command leads to an additional lateral velocity and therefore increases the overall, aerodynamic velocity. The low-frequency oscillation is particularly evident in u_g^{w} and y^{g}, but it exhibits a well-damped response with an uncritical amplitude.

The Fourier analysis reveals two further distinct oscillations in the flight test data at frequencies of 0.89 Hz and 0.99 Hz. In addition, the second and third harmonics of the multiplicates of the fundamental oscillation are recognizable. The frequency of the oscillations corresponds to the poles of the attitude controller and is within the range of the calculated uncertainty envelope. Since both the roll and pitch commands are realized by the common actuator for the elevon deflection, the oscillations are closely related and both excited during flight. The high-frequency oscillation is evident in particular in the

time range of $t = 30 - 40\,\mathrm{s}$ of the pitch command in the flight test results. Compared to the nominal poles of the robustness analysis, the frequency is lower and less damped, corresponding to pole locations close to the bounds of the uncertainty envelope. This indicates that the actual actuator dynamics are significantly less effective than in the nominal case and close to the worst-case gains. This discrepancy becomes evident during the flight test, where the attitude controller is designed overly aggressive, based on the design of a faster and more effective actuator. While the assumption of an actuator with low effectiveness is robust with respect to the INDI design, it leads to reduced performance of the attitude controller.

Within the range of this verification, no further specification of the bounds of the uncertainties or an adaption of the nominal values of the parameters is conducted on the basis of the verification results. The uncertainties are partly dependent on the current flight state, for example the linearized thrust or the actuator effectiveness, and therefore vary during flight. However, all modeled oscillations were identified within the simulation and flight test results and the uncertain model is assessed to describe the actual dynamics of the controlled flight system in prop-borne flight in a wind field sufficiently accurate.

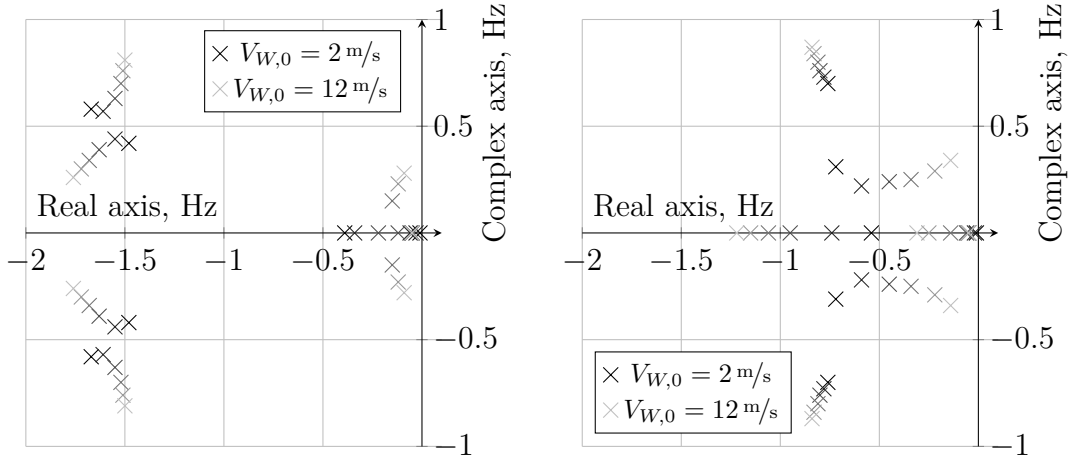
5.2.4. Wind Analysis

The poles of the verified closed-loop system are analyzed with respect to varying wind velocities. Since the effect of the disturbance increases quadratically with wind velocity, the wind has a significant influence on the closed-loop dynamics, especially at higher wind velocities. It can shift the frequency and damping constant of the oscillations, potentially leading to instabilities. This approach therefore allows to estimate the maximum wind velocity for which the designed flight controller remains effective.

The linearization point of the wind velocity of Eq. 5.5 is sampled in increments of $\Delta V_W = 2\,\mathrm{m/s}$ in the range of $2 - 12\,\mathrm{m/s}$. The evaluation of all uncertainties and wind velocities leads to a broad spectrum of the dynamics. As such, the analysis is focused on the closed-loop system of the parameters of the nominal and worst-case gains. This results in two discrete setpoints: the nominal system reflects the dynamics corresponding to the controller's design case, while the worst-case system represents an edge case that provides insights into the system's response with maximum aerodynamic velocity u_a^{w}. Given the limited trim range and controllability, it is essential to minimize susceptibility in this direction.

The pole movement of the nominal system due to the varying wind velocities is depicted in Fig. 5.11a. The poles corresponding to the bandwidth of the attitude controller tend to shift in opposite directions towards higher frequencies and dampings, and vice versa.

Yet, the movement remains reasonable with a damping constant close to one. The pole corresponding to the integral state of the velocity remains in the left half-plane and moves slightly toward higher frequencies. However, the wind velocity has the greatest effect on the poles of the pitch-roll coupling. As the wind velocity increases, the poles start oscillating and move toward the complex axis. At $V_{w,0} = 8\,\mathrm{m/s}$, the oscillation is still well damped with a damping constant of 0.7. By further increasing the wind velocity, the damping constant is reduced significantly and the oscillation of the pitch-roll motion becomes critical. Concerning the poles of the nominal design, the maximum wind velocity for safe operation is therefore about $8\,\mathrm{m/s}$.



(a) Nominal system.

(b) Worst-case gain system.

Figure 5.11.: Pole movement of the pitch-roll motion. The legend marks the minimum and maximum wind velocity.

Figure 5.11b depicts the relating poles of the closed-loop system for varying wind velocities in combination with the worst-case gains. The pole frequencies associated with the attitude controller's bandwidth are significantly reduced compared to the nominal case. Since the worst-case gains involve a slow actuator with low effectiveness, this further decreases the controller's bandwidth. As a result, the attitude controller becomes less responsive and operates more slowly. In the event of a disturbance, the controller's ability to counteract the disturbing velocity is diminished. Simultaneously, the poles related to the velocity and heading controllers shift to higher frequencies, expanding their bandwidth beyond that of the attitude controller. This disrupts the intended cascade control structure of the flight controller and leads to commands with a higher bandwidth than the attitude controller can realize. In combination, the overall performance of the flight controller is significantly reduced. Due to a high drag coefficient and a large distance between the aerodynamic center and the center of gravity of the worst-case gains, the effect of a disturbance is large.

As such, the aerodynamic velocity u_a^{w} reaches its maximum value over frequency.

The controller corresponding to the worst-case gains exhibits reduced coupling effects between the pitch and roll motions. Due to the decreased performance, the system's dynamic response to disturbances is limited. As a consequence, there is no oscillation in the coupling of the pitch-roll motion. However, there is a pole pair associated with the attitude control of the pitch angle that shifts toward the complex axis as the wind velocity increases. Above a wind velocity of $8\,\mathrm{m/s}$, the damping constant is below 0.7 and the oscillation in pitch becomes critical.

The reduced accuracy in wind alignment can lead to flight states where the conditions of the linearized closed-loop model are no longer satisfied. For example, an aerodynamic velocity exceeding the threshold of $3\,\mathrm{m/s}$ can result in reaching the maximum elevon deflection. To assess the dynamic response of the closed-loop system regarding the aerodynamic velocity, the sensitivity function due to a rotation of the wind vector ψ_W is analyzed. The sensitivity function indicates how the disturbance over frequency is influenced by the controller feedback. A lower magnitude indicates a further attenuation of the wind disturbance.

Figure 5.12 depicts the bode plot of the transfer function of the wind heading ψ_W to the aerodynamic velocity u_a^{w} for the system with worst-case gains. It is linearized at $V_{W,0} = 8\,\mathrm{m/s}$, corresponding to the wind velocity for which the analysis of the poles indicates that all oscillations remain well damped. For a wind rotation at low frequencies below $0.1\,\mathrm{Hz}$, the magnitude of the system is small and the phase shift approaches $-90°$. The flight controller is able to successfully track the wind direction and suppress the external disturbance of the wind. High frequencies above $2\,\mathrm{Hz}$ are beyond the bandwidth of the controller, correspondingly, there is no reaction due to a rotation of the wind disturbance. A modification of the wind direction in this frequency domain typically corresponds to gusts, for which the system is intentionally designed not to respond to. The aerodynamic velocity is then directly equal to the linearized wind velocity of $8\,\mathrm{m/s}$ with a maximum phase shift of $-180°$. Note that the bode plot depicts the output of the aerodynamic velocity due to a step of $\psi_W = 1\,\mathrm{rad}$. A step for example of $30°$ as implemented in the simulation results of the wind alignment therefore corresponds to approximately half the aerodynamic velocity.

In the range of approximately $0.2 - 0.5\,\mathrm{Hz}$, the magnitude of the sensitivity function of the external disturbance is reinforced. This corresponds to the critical frequency domain of the closed-loop system. The controller's reaction is delayed in relation to the disturbance and further increases the aerodynamic velocity u_a^{w} by around $20\,\%$. The wind tracking is

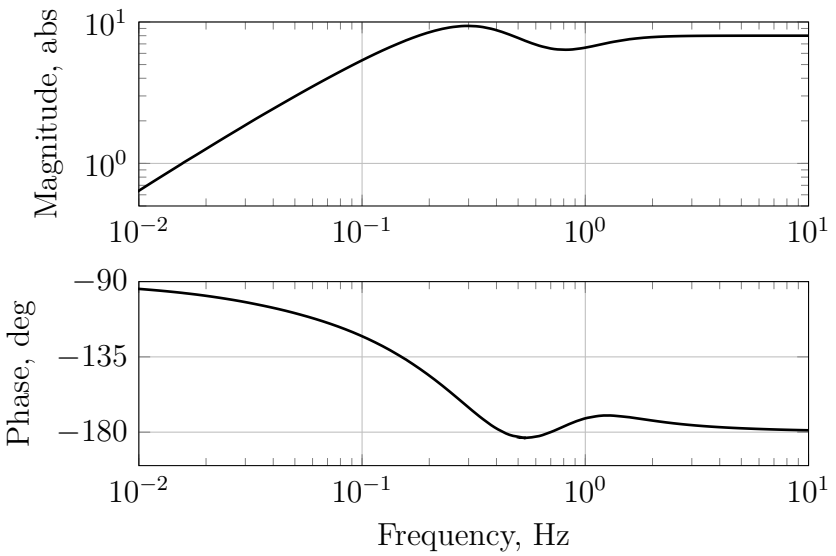


Figure 5.12.: Bode plot of the sensitivity function with worst-case gains.

imprecise, which may lead to the exceedance of the maximum operational aerodynamic velocity. Therefore, the wind velocity of 8 m/s should not be significantly exceeded, as doing so could result in a substantial increase in the aerodynamic velocity u_a^{w}, caused by the dynamic response to changes in wind direction.

5.3. Discussion

The following section critically discusses the simulation and flight results of the designed launch trajectory controller in relation to the design objectives. At first, the focus is on the evaluation of the transition in low wind conditions with respect to the full flight envelope of the yaw-roll motion, the tether connection, and stationary, stabilized flight. In particular, the aspects of power consumption and space requirements are further highlighted. Finally, the robustness of prop-borne flight in high wind conditions is comprehensively discussed.

Transition Analysis

The results demonstrated that the cascaded launch trajectory controller successfully performs the transition across the entire flight envelope. Firstly, the attitude and angular acceleration controllers stabilized all axes of the flight system from vertical to horizontal flight despite the Euler angle singularity. Secondly, the velocity controller effectively maintained the desired velocities, even accounting for model-in-the-loop simulation deviations. Thirdly, the velocity tracking controller provided a suitable trajectory of aerodynamic velocity, guiding the flight system from zero to the target velocity, while the position controller maintained a constant height.

The velocity controller successfully realized the stationary trim path, with flight states and control inputs aligned closely with the intended course. Disturbances arising from the tether forces, unsteady accelerations, sensor noise, and gusts were largely mitigated, ensuring the applicability of the transition for both tethered and untethered systems in steady and unsteady environments. The simulation model however assumed an unstretched tether, which must be ensured by a sufficient tether length.

During the initial yaw motion, the angle of attack exhibited significant fluctuations due to low aerodynamic velocity, but it converged towards the designed value of zero as velocity increased. This led to low pitch moments and small elevon deflections, effectively bypassing the limited flight envelope of the longitudinal motion and allowing for stable, trimmed flight according to the operating points of the trim conditions. The elevon deflection provides sufficient margin to accommodate stronger disturbances, particularly in strong and gusty wind conditions.

The subsequent roll motion initiated a gradual increase in the angle of attack, enabling the transition to wing-borne flight. Given the limited region of attraction of the velocity controller during this critical phase, the velocity tracking controller reduced the acceleration of the commanded operating points. It ensured stable roll initiation, in which the velocity controller managed disturbances effectively based on the associated control allocation. Notably, there was a significant distance to the maximum angle of attack, suggesting that roll motion could potentially be initiated at lower aerodynamic velocities or with increased acceleration. Further analysis is required to validate the roll initialization under stronger wind conditions.

Power Consumption and Space Requirements

The power consumption, represented by thrust demand and transition time, remained low. The transition was performed at low wind speeds, corresponding to the maximum power consumption and space requirements of the designed flight trajectory. During the yaw motion, thrust increases since the angle of attack was maintained low. A high acceleration was therefore applied to keep the yaw motion during prop-borne flight short. Due to the higher prioritization of robustness against wind disturbances, the roll motion to increase lift is initialized only at a high aerodynamic velocity. The maximum thrust is required in the flight phase during the yaw motion with maximum acceleration and shortly before the acceleration is reduced to initialize the roll motion for lift increase. Considering the time of the transition, yaw and roll motions require each around 7 s.

Maximum yaw and roll accelerations, constrained by the flight controls of elevon deflection and thrust, both had margin for faster transition. An evaluation of the maximum acceleration limits to optimize for power consumption has yet to be carried out. Particularly the roll motion in wing-borne flight was realized at low accelerations due to the velocity controller's restricted region of attraction. By accurately analyzing this region of attraction and optimizing an unsteady trim path for power consumption, it becomes possible to approach the maximum acceleration limits closer. Especially the last phase of the roll motion can be conducted with increased acceleration when the angle of attack is less sensitive to exceed its maximum value. Enhancements to the velocity controller could further improve performance, for example by reducing the gap between the commanded operating points and the actual flight state. The velocity controller can incorporate the acceleration-specific operating points to minimize deviations during the unsteady transition. Moreover, linear quadratic tracking techniques with time-dependent formulations could address the deviations caused by the applied gain-scheduling method [139]. Another approach could involve deliberately passing through regions of controller instability during rapid unsteady acceleration, aiming to quickly reach the stable wing-borne flight phase. However, a general trade-off is required between controllability and robustness, as greater controllability often comes at the expense of reduced disturbance tolerance.

The transition occurred within a reasonable spatial area, however, there is potential for improvement. The entire transition was presented up to the point of achieving horizontal, wing-borne flight. In the context of the launching phase of AWE, the transition is followed by curved flight to reach crosswind operation. To optimize the process, the curved flight can be initialized shortly after achieving wing-borne flight during the initial roll motion, corresponding to the time stamp of $t = 10\,\mathrm{s}$ in Fig. 5.2. In this flight phase, the flight system can rotate into the wind direction, since the wind no longer causes the flight system to exceed its flight envelope. As such, the lateral space of 130 m required for transition can be nearly halved.

Robustness under Wind Conditions

Prop-borne flight was further validated under wind conditions. This phase of flight is particularly challenging due to the high susceptibility of the vertical wing area to wind disturbances and the corresponding limited flight envelope in the longitudinal axis. Hovering with zero ground velocity and maximum wind velocity was selected as a worst-case scenario, as any wind rotation during this phase causes the strongest disturbances. In typical AWE operations, the flight system is not intended to hover for extended periods. Following the upward velocity of takeoff, the system transitions immediately without remaining in a

hover position. However, landing requires stable hovering, and disturbance susceptibility even increases, as the reversed airflow reduces the effectiveness of the elevons. The selected yaw-roll transition allows for transition on constant height to enable the landing to occur near the ground and keep the landing sequence short. Nonetheless, achieving robust wind alignment is particularly crucial during the initial transition and the landing phases.

Both simulation and flight test results have demonstrated the adaptability of the flight trajectory controller in dynamic, rotating wind fields with mean wind velocities around $5 - 7\,\mathrm{m/s}$. While high-frequency gusts were effectively suppressed, the system accurately adjusted its heading to match the shifting wind direction. Even in these challenging wind conditions, the flight tests showed that position commands were executed effectively, which is essential for precise takeoff and landing maneuvers. The heading adjustments were related in this case to the aerodynamic heading, and the stationary flight envelope limit of $u_a^{\mathrm{w}} = 3\,\mathrm{m/s}$ was maintained, even under dynamic wind conditions.

The validation indicated that the upper robustness limits of the designed controller are nearly reached and emphasize the challenges of wind alignment in strong wind fields. Slight low- and high-frequency oscillations were observed, which affected the performance of the wind alignment. During the flight tests, the damping of these oscillations was still sufficient, but further increases in wind velocity quadratically increase the disturbing forces, potentially leading to oscillations that exceed the stability range. Given that wind velocities in the tests were $5 - 7\,\mathrm{m/s}$, there is still a considerable gap to the maximum operating wind velocities around $15 - 25\,\mathrm{m/s}$ expected in AWE systems [131, 164].

Several challenges arise regarding the designed launch trajectory controller for the wind alignment of the flight system. First, the effectiveness of the elevon deflection to counteract dynamic disturbances is limited at approximately $\Delta u_a^{\mathrm{w}} = 3\,\mathrm{m/s}$. This is a restrictive limitation, making precise tracking of the wind direction crucial. Second, the instability and non-minimum phase behavior in the longitudinal axis significantly complicate the wind alignment. When a disturbing aerodynamic inflow occurs due to wind rotation, a destabilizing down-pitch moment is generated, creating a thrust component in the horizontal direction that amplifies the disturbance. The velocity and attitude controllers counteract the pitch moment with the inherent delay of the elevon actuator. However, due to the non-minimum phase behavior in pitch response, this further amplifies the inflow, before the actual increase of the pitch angle reduces the disturbance. Therefore, the heading controller must quickly adjust the flight system's orientation to support the reduction of the disturbance. Third, maintaining position induces increased aerodynamic velocity after a disturbance, as the system attempts to return to its initial position. Since

any additional aerodynamic velocity should be avoided, it can be advantageous to relax the demand for exact position control in this axis and only setting an upper limit on positional deviations. Within this boundary, position control would remain inactive, only becoming active if the limit is exceeded.

In the robustness analysis, the oscillations of the closed-loop system were precisely determined, enabling accurate tuning of the flight trajectory controller for wind alignment. The closed-loop model of the pitch-roll coupling incorporated simplifications, particularly in the approximation of the INDI and the model of the forces and moments. However, the applied simplifications provided sufficient accuracy and reduced the problem to a few key parameters for which the range of uncertainties was identified. Regarding actuator dynamics, the frequency analysis of the attitude controller's oscillations indicated that the actual actuator behavior closely approaches worst-case gain conditions. While a worst-case assumption of the actuator model is robust regarding the INDI design, the model deviations led to oscillations in attitude. Therefore, the design of the attitude and velocity controllers require to better account for actuator dynamics with less effectiveness and reduce the controller's aggressiveness for improved precision. Furthermore, the pitch-roll coupling necessitates synchronized tuning of the velocity and heading controllers. More aggressive tuning can achieve rapid wind alignment but eventually induce low-frequency oscillations with large pitch amplitudes in stronger wind conditions. As the disturbing effect of wind increases quadratically with wind velocity, accurate tuning becomes particularly important at higher wind velocities. Implementing gain scheduling based on wind velocity can provide more precise tuning for varying wind conditions, with the robustness analysis serving as suitable foundation for this approach.

This analysis offers insights for potential advanced controller design focused on disturbance rejection. The robustness analysis identified a critical frequency range in which changes in the wind vector cause maximum disturbance to aerodynamic velocity u_a^{w} for the model with worst-case gains. Using μ-synthesis allows for the integration of uncertainties into the controller design, optimizing performance across all identified uncertainties [165]. Additionally, H_∞ controllers can target the critical frequency range, minimizing disturbances within that bandwidth [157]. Finally, incorporating gust load alleviation systems that detect gusts in advance is a viable option to further enhance disturbance rejection.

For the designed launch trajectory controller, the robustness analysis approximated a maximum wind velocity limit of $8\,\mathrm{m/s}$. Within this range, the controller effectively rejects disturbances and stabilizes the system, ensuring proper performance during the yaw-roll transition, which relies on accurate alignment with the wind vector.

6. Conclusion and Outlook

In this thesis, a comprehensive methodology for designing a launch trajectory controller has been developed for controlling the aerodynamic velocity during the transition of a flying wing from vertical hover to horizontal forward flight within the application of an airborne wind energy system. The designed controller finds a compromise between the requirements of airborne wind energy and the specific flight characteristics of the flying wing. Beyond ensuring attitude stabilization across all axes, particularly during the critical phase of vertical hover flight, the controller ensures flight within the reduced flight envelope in the longitudinal pitch axis. Additionally, the airborne wind energy system requires operation across a broad range of wind velocities from low to high, while considering power efficiency and the constraints of the tether connection. A lateral yaw-roll transition strategy was proposed for the launching phase, and a carefully selected trim path of operating points was identified to meet the specified requirements. This optimized trim path served as a basis for the design of the flight trajectory controller, which precisely controls the velocity throughout the transition along the predetermined flight path.

Following a detailed explanation of the instabilities of the flying wing along all attitude axes in prop-borne flight, an individual nonlinear flight model was developed for the specific flight system and transition maneuver. A focus was placed on the aerodynamic and tether models as the most distinctive model components of the AWE system. For aerodynamics, a component-based approach was employed to capture the flight mechanics across the entire flight envelope, ranging from low aerodynamic velocities during vertical prop-borne flight to high aerodynamic velocities in horizontal wing-borne flight.

In the aerodynamic model, special emphasis was given to the effect of high aerodynamic angles, which can both vary within their full range during the operation. Concerning the angle of attack, the airfoil polar was extrapolated using a flat-plate polar at high angles. Due to the shift in the point of pressure towards the centroid of the wing area, the pitch moment coefficient increases significantly, which highlighted the challenge to trim the pitch axis during vertical flight when high angles of attack can occur. To account for high slip angle effects, the orientation of the wing elements of the component-based model are dynamically adjusted to be aligned with the aerodynamic inflow, and the element

definitions and aerodynamic polars are modified accordingly. The slip angle influences the coefficients of both longitudinal and lateral motions. For a simplified flight system, these coefficients were validated using *xflr5* simulation data, showing alignment with the coefficients for longitudinal motion and the roll moment coefficient. Discrepancies in the lateral forces and yaw moments at high aerodynamic angles were attributed to a non-accounted rotation of the angle of attack in the *xflr5* simulations. As such, the courses of the coefficients of the lateral motion were further verified by comparing with wind tunnel data from existing literature, confirming general consistency.

Due to the tether connection, a modeling of the tether forces was required. A hybrid tether model was implemented, combining the effects of gravity and aerodynamic forces acting on the unstretched tether with the tensile forces that dominate once the tether is stretched. In the stretched state, tensile forces significantly increase, which outlined the critical importance of maintaining the tether unstretched during the transition. This minimizes external disturbances caused by the tether and reduces thrust demand.

The limited literature on the launching phase of airborne wind energy systems was extended to capture existing state-of-the-art trajectory concepts for transition of tailsitter flight systems. It highlighted the various approaches, characteristics, and challenges of similar flight system designs and presented the transition via longitudinal pitch motion as the common flight trajectory. However, the analyzed flight envelope for the airborne wind energy system in pitch is highly constrained. The system's large wing area amplifies pitch moments, while the control authority in pitch is inherently limited in prop-borne flight. The analysis outlined the difficulties of controlling the flight system during a longitudinal pitch transition, suggesting the need to explore alternative trajectory strategies better suited for airborne wind energy applications.

Based on the design criteria, a suitable launching phase for the airborne wind energy system was selected. The design criteria require in particular a robust operation with respect to the limited flight envelope and the wind, while a power efficient operation is declared as a secondary design goal. The proposed transition involves a lateral yaw-roll maneuver, starting with a yaw-dominant motion for rapid acceleration, followed by a roll-dominant phase to generate increased lift. This lateral yaw-roll transition is a complex maneuver requiring coordinated variations in all three attitude angles, yet it allows for a controlled, stationary transition at a constant height within the system's highly constrained flight envelope. Moreover, the maneuver can be performed across the entire range from zero to high wind velocities. By aligning the flight path along the wind vector, the angle of attack remains within controllable limits independent of the wind velocity. In upwind conditions,

the wind velocity contributes to the aerodynamic velocity, minimizing ground impact and keeping power consumption low.

For the desired transition, the selection of operating points allowed the integration of the design objectives regarding sufficient control reserves. A detailed analysis of the flight envelope was conducted to identify the flight control limits. A comprehensive scanning method was employed, sampling all relevant attitude angles within a fine grid to map the complete solution space of trimmed flight states. Operating points were defined for each velocity set based on the commands for the attitude angles and thrust. As this set of variables is underdetermined, the remaining degree of freedom was leveraged to select the trim path with respect to thrust demand and elevon deflection.

An optimized trim path was manually selected out of the entire flight envelope, which covers the range from hover to wing-borne flight and finds a compromise between the diverse design objectives. During the yaw motion, the flight envelope is strictly limited, so the primary focus was on minimizing elevon deflection to ensure sufficient robustness against wind disturbances. By maintaining a zero angle of attack, aerodynamic velocity perpendicular to the wing surface is avoided to reduce undesired pitch moments. A higher thrust demand was accepted to prioritize increased wind robustness. Once sufficient aerodynamic velocity is achieved, the system is less sensitive to disturbances, allowing the initiation of the roll motion to increase the angle of attack and lift. Adequate margin was maintained from the maximum angle of attack to ensure robustness to stall. The operating points were selected such that a constant increase in velocity corresponded to a constant turning rate, enabling a direct mapping of angular acceleration limits to limits of the linear acceleration in the higher control cascade. The selected trim path was linearized to derive control effectiveness of all Euler angles and thrust for the velocity controller. An analysis of the validity range of the linearization enabled the identification of preferred control actions along each flight axis, which established a foundation for robust controller design.

The launch trajectory controller is designed in a cascaded control structure to accurately perform the transition of the flight system. The attitude and angular acceleration controllers stabilize the aircraft's attitude across all axes, efficiently allocating the flight controls throughout the entire flight envelope during the transition. The velocity controller presents the core controller, which integrates the selected operating points defined by the aerodynamic velocity. An LQR controller is implemented based on a gain-scheduling method to allow for the multi-axial transition along the trim path with respect to the control effectiveness of the linearization model. By selectively penalizing control outputs

along each velocity component, the controller ensures a well-balanced design that maintains performance and stability throughout the transition. At the uppermost control level, the velocity tracking controller commands a dynamic time course of the operating points based on the desired acceleration limits. The height is maintained by the position controller, while the heading controller ensures proper alignment of the flight system with the wind direction, minimizing wind-induced disturbances.

The performance of the launch trajectory controller was validated through simulation, demonstrating its effectiveness within a nonlinear environment that included gusts, sensor noise, and tether forces. The transition was performed with zero mean wind velocity, confirming the system's ability to operate at the lower wind velocity limit, which corresponds to the maximum flight range. The controller stabilized all axes and accurately followed the selected operating points along the flight path. Maintaining an angle of attack of zero during yaw motion proved challenging, since the angle of attack is highly sensitive to disturbances at low aerodynamic velocities. However, as velocity increased, the angle of attack approached the target value of zero, and the elevon deflection remained low, enhancing the system's ability to reject disturbances at higher wind velocities. A high acceleration was applied during yaw motion to minimize flight time and reduce power consumption in this flight phase of high thrust demand. The roll motion was initiated with a reduced acceleration to account for the limited region of attraction in this flight phase. The angle of attack was slightly increased to transition smoothly into horizontal wing-borne flight at a slip angle of zero. Stall effects were effectively avoided by the controller. Due to the high aerodynamic velocity during the roll motion, the flight range in the lateral direction increased significantly until horizontal, wing-borne flight was reached. However, for airborne wind energy applications, the curved flight can be followed immediately after the roll initialization to reduce the required flight range.

Specifically the flight phase in prop-borne flight in strong wind conditions and low ground velocities was identified as a highly challenging phase of operation. To minimize disturbing pitch moments and maintain trimmed flight within the flight envelope, the wing area must be aligned with the main wind direction. Within simulation and flight test results, the disturbance rejection through accurate wind adjustment was verified. Both simulation and flight tests demonstrated precise tracking of the rotation of the wind vector. The system avoided reacting to gusts, while the heading remained aligned with the main wind direction. A strong aerodynamic inflow perpendicular to the wing area was prevented, allowing the flight system to remain within its flight envelope. However, low- and high-frequency oscillations occurred, indicating the limits of the designed flight trajectory controller.

A comprehensive robustness analysis of the operation in prop-borne flight in a wind field was conducted to demonstrate the stability of the closed-loop system. Due to wind influence and the design of the control structure, a coupling between roll and pitch motions occurs. A simplified model of this coupled closed-loop system was derived, focusing on the primary forces and moments acting within the wind field. This simplification reduced the system to a few key aerodynamic and geometric parameters, allowing for the systematic introduction of model uncertainties for each parameter. By linearizing the system at different wind velocities, the poles of the closed-loop system were analyzed. The oscillations observed in the simulation and flight test results were accurately replicated by the complex poles of the closed-loop system, confirming the accuracy of the simplified model. Worst-case gains were determined, representing the most unfavorable scenario of maximum aerodynamic velocity perpendicular to the wing area due to wind vector rotation. For both nominal and worst-case gains, the poles of the closed-loop system were analyzed for increasing wind velocity. Higher wind velocities amplified the disturbing effects of wind rotation, leading to reduced damping of oscillations. A critical frequency domain was identified, where wind rotation further intensified aerodynamic velocity. For the designed launch trajectory controller, a maximum wind velocity of $8\,{}^{\mathrm{m}}/_{\mathrm{s}}$ was derived, beyond which the resulting oscillations become critical. The robustness analysis provides an effective tool for fine-tuning the controller to optimize wind alignment, ensuring stable flight performance even in challenging wind conditions.

Overall, this thesis demonstrated the feasibility of the designed launch trajectory controller for the transition of a flying wing in an airborne wind energy application. Upcoming work will need to validate the entire transition through flight tests, particularly to confirm the feasibility of roll motion for achieving wing-borne flight. Additionally, an analysis of flight limits with respect to the maximum acceleration during transition can support for optimizing power consumption. Although the stationary design of the operating points allows transitions in both directions, further validation is necessary for the transition from wing-borne to prop-borne flight. Regarding prop-borne flight, the current maximum limits of the wind velocity requires to be addressed to enhance operability at higher wind velocities. Moreover, the flight control system must be expanded to cover the complete launching phase, including the subsequent curved flight to reach the power generation phase. Given that maximizing power output in crosswind flight is a key design objective of the flying wing in AWE, proving its power generation capabilities will be essential in future studies.

Bibliography

[1] J. Kim, S. Kim, C. Ju, and H. I. Son, "Unmanned aerial vehicles in agriculture: A review of perspective of platform, control, and applications," *IEEE Access*, vol. 7, pp. 105 100–105 115, 2019. DOI: 10.1109/ACCESS.2019.2932119.

[2] M. Hartmann, N. Voget, S. Seitz, and D. Moormann, "Trajectory planning for efficient BVLOS drone flights over agricultural points of interest," in *Proceedings of the 2024 CEAS EuroGNC conference*, 2024.

[3] A. Rejeb, K. Rejeb, S. J. Simske, and H. Treiblmaier, "Drones for supply chain management and logistics: A review and research agenda," *International Journal of Logistics Research and Applications*, vol. 26, no. 6, pp. 708–731, 2023, ISSN: 1367-5567. DOI: 10.1080/13675567.2021.1981273.

[4] J. Fan and M.A. Saadeghvaziri, "Applications of drones in infrastructures: Challenges and opportunities," *International Journal of Mechanical and Mechatronics Engineering*, vol. 13, no. 10, 2019. DOI: 10.5281/zenodo.3566281.

[5] A. Merei, H. Mcheick, and A. Ghaddar, "Survey on path planning for UAVs in healthcare missions," *Journal of medical systems*, vol. 47, no. 1, p. 79, 2023. DOI: 10.1007/s10916-023-01972-x.

[6] R. Ashour, S. Aldhaheri, and Y. Abu-Kheil, "Applications of UAVs in search and rescue," in *Unmanned Aerial Vehicles Applications: Challenges and Trends*, Cham: Springer International Publishing, 2023, pp. 169–200, ISBN: 978-3-031-32036-1. DOI: 10.1007/978-3-031-32037-8.

[7] Mordor Intelligence Research & Advisory, *UAV market size & share analysis - growth trends & forecasts (2024-2029)*, Ed. Mordor Intelligence, 2023.

[8] Q. Quan, *Introduction to Multicopter Design and Control*. Singapore: Springer Singapore, 2017. DOI: 10.1007/978-981-10-3382-7.

[9] K. Sibilski, J. Pietrucha, and M. Zlocka, "Comparative evaluation of power requirements for fixed, rotary, and flapping wings micro air vehicles," in *AIAA Atmospheric Flight Mechanics Conference and Exhibit*, Reston, Virigina: American Institute of Aeronautics and Astronautics, 2007, ISBN: 978-1-62410-131-1. DOI: 10.2514/6.2007-6498.

[10] U. Ozdemir, Y. O. Aktas, A. Vuruskan, Y. Dereli, *et al.*, "Design of a commercial hybrid VTOL UAV system," *Journal of Intelligent & Robotic Systems*, vol. 74, no. 1-2, pp. 371–393, 2014, ISSN: 0921-0296. DOI: 10.1007/s10846-013-9900-0.

[11] F. A. Sambodo, W. Wahyanto, M. Wijaya, G. H. Mustofa, *et al.*, "Preliminary design of dual-system hybrid VTOL UAV for medical delivery purpose," in *The 8th International Seminar on Aerospace Science and Technology - ISAST*, AIP Publishing, 2021, p. 030 007. DOI: 10.1063/5.0060064.

[12] A. Marta and A. Muis, "Flight dynamics modeling of dual thrust system hybrid UAV," in *International Conference on Artificial Intelligence and Mechatronics Systems (AIMS)*, IEEE, 2021, pp. 1–5, ISBN: 978-1-6654-2482-0. DOI: 10.1109/AIMS52415.2021.9466038.

[13] M. Mousaei, J. Geng, A. Keipour, D. Bai, *et al.*, "Design, modeling and control for a tilt-rotor VTOL UAV in the presence of actuator failure," in *International Conference on Intelligent Robots and Systems (IROS)*, IEEE, 2022, pp. 4310–4317, ISBN: 978-1-6654-7927-1. DOI: 10.1109/IROS47612.2022.9981806.

[14] Z. Chen and H. Jia, "Design of flight control system for a novel tilt-rotor UAV," *Complexity*, vol. 2020, pp. 1–14, 2020, ISSN: 1076-2787. DOI: 10.1155/2020/4757381.

[15] Z.-Y. Lv, Y. Wu, Q. Zhao, and X.-M. Sun, "Design and control of a novel coaxial tilt-rotor uav," *IEEE Transactions on Industrial Electronics*, vol. 69, no. 4, pp. 3810–3821, 2022, ISSN: 0278-0046. DOI: 10.1109/TIE.2021.3075886.

[16] P. Osterloh, J. Krimphove, E. König, T. Islam, *et al.*, "Advanced flight control architecture for safe BVLOS drone operations," in *Proceedings of the 2024 CEAS EuroGNC conference*, 2024.

[17] L. M. Sanchez-Rivera, R. Lozano, and A. Arias-Montano, "Development, modeling and control of a dual tilt-wing UAV in vertical flight," *Drones*, vol. 4, no. 4, p. 71, 2020. DOI: 10.3390/drones4040071.

[18] M. Schütt, T. Islam, P. Hartmann, and D. Moormann, "Scalable design approach to analyze flight mechanical performance for tiltwing UAVs," in *31st Congress of the International Council of the Aeronautical Sciences 2018*.

[19] E. Small, E. Fresk, G. Andrikopoulos, and G. Nikolakopoulos, "Modelling and control of a tilt-wing unmanned aerial vehicle," in *2016 24th Mediterranean Conference on Control and Automation (MED)*, IEEE, 2016, pp. 1254–1259, ISBN: 978-1-4673-8345-5. DOI: 10.1109/MED.2016.7536050.

[20] A. S. Saeed, A. B. Younes, C. Cai, and G. Cai, "A survey of hybrid unmanned aerial vehicles," *Progress in Aerospace Sciences*, vol. 98, pp. 91–105, 2018, ISSN: 03760421. DOI: 10.1016/j.paerosci.2018.03.007.

[21] M. L. Loyd, "Crosswind kite power (for large-scale wind power production)," *Journal of Energy*, vol. 4, no. 3, pp. 106–111, 1980, ISSN: 0146-0412. DOI: 10.2514/3.48021.

[22] A. Cherubini, A. Papini, R. Vertechy, and M. Fontana, "Airborne wind energy systems: A review of the technologies," *Renewable and Sustainable Energy Reviews*, vol. 51, pp. 1461–1476, 2015, ISSN: 13640321. DOI: 10.1016/j.rser.2015.07.053.

[23] J. Weber, M. Marquis, A. Cooperman, C. Draxl, *et al.*, *Airborne wind energy*, 2021. DOI: 10.2172/1813974.

[24] R. Schmehl, Ed., *Airborne Wind Energy* (Green Energy and Technology). Singapore: Springer Singapore, 2018, ISBN: 978-981-10-1946-3. DOI: 10.1007/978-981-10-1947-0.

[25] International Energy Agency, *Renewable energy market update: Outlook for 2023 and 2024*, Ed. IEA, Paris, France, 2023. [Online]. Available: https://www.iea.org/reports/renewable-energy-market-update-june-2023 (accessed on 02/11/2024).

[26] H. Ritchie, P. Rosado, and M. Roser, *Share of electricity generated by wind power*, Ed. Ember, Energy Institute, 2023. [Online]. Available: https://ourworldindata.org/grapher/share-electricity-wind (accessed on 02/08/2024).

[27] A. Lucas, *Wind, Water, Work: Ancient and Medieval Milling Technology* (Technology and Change in History Ser). Boston: BRILL, 2006, ISBN: 978-90-47-41722-4.

[28] U.S. Department of Energy, *Offshore wind market report: 2023 edition*, Ed. U.S. Department of Energy, 2023.

[29] A. Betz, *Wind-Energie und ihre Ausnutzung durch Windmühlen [Wind-Energy and its utilization by windmills]*, unaltered reprint of original [Göttingen, Vandenhoeck, Ruprecht], 1926. Grebenstein: Öko-Buchverl., 1982, ISBN: 978-3-922964-11-7.

[30] M. Mahmoud, T. Salameh, A. A. Makky, M. A. Abdelkareem, *et al.*, "Case studies and analysis of wind energy systems," in *Renewable Energy - Volume 1 : Solar, Wind, and Hydropower*, Elsevier, 2023, pp. 363–387, ISBN: 9780323995689. DOI: 10.1016/B978-0-323-99568-9.00019-4.

[31] T. Stehly, P. Beiter, and P. Duffy, *2019 cost of wind energy review*, Ed. National Renewable Energy Lab., Golden, Colorado, 2020. DOI: 10.2172/1756710.

[32] U. Ahrens, M. Diehl, and R. Schmehl, Eds., *Airborne Wind Energy* (SpringerLink Books). Berlin, Heidelberg: Springer, 2013, ISBN: 978-3-642-39964-0. DOI: 10.1007/978-3-642-39965-7.

[33] L. B. C. Pecanha, N. de Souza Barbosa Oliveira, and W. V. Bretas, "Generation of wind energy with kites: A review of the airborne wind energy technology," in *2020 IEEE PES Transmission & Distribution Conference and Exhibition - Latin America (T&D LA)*, IEEE, 2020, pp. 1–6, ISBN: 978-1-7281-4155-8. DOI: 10.1109/TDLA47668.2020.9326104.

[34] C. Vermillion, M. Cobb, L. Fagiano, R. Leuthold, *et al.*, "Electricity in the air: Insights from two decades of advanced control research and experimental flight testing of airborne wind energy systems," *Annual Reviews in Control*, vol. 52, pp. 330–357, 2021, ISSN: 13675788. DOI: 10.1016/j.arcontrol.2021.03.002.

[35] M. de Lellis, R. Reginatto, R. Saraiva, and A. Trofino, "The betz limit applied to airborne wind energy," *Renewable Energy*, vol. 127, pp. 32–40, 2018, ISSN: 09601481. DOI: 10.1016/j.renene.2018.04.034.

[36] F. Trevisi, M. McWilliam, and M. Gaunaa, "Configuration optimization and global sensitivity analysis of ground-gen and fly-gen airborne wind energy systems," *Renewable Energy*, vol. 178, pp. 385–402, 2021, ISSN: 09601481. DOI: 10.1016/j.renene.2021.06.011.

[37] H. Siegmann, *Smoothed coordinates HS 3.4/12.0B*, Stuttgart, 2001. [Online]. Available: https://www.aerodesign.de/profile/data/hs3412b.txt (accessed on 03/01/2024).

[38] H. Fuest, D. F. Duda, T. Islam, and D. Moormann, "Starting procedure of a flying wing for an airborne wind energy system," *CEAS Aeronautical Journal*, vol. 16, no. 1, pp. 307–321, 2025, ISSN: 1869-5582. DOI: 10.1007/s13272-024-00791-1.

[39] H. Fuest, D. F. Duda, T. Islam, T. Ostermann, *et al.*, "Stabilization of the vertical take-off of a rigid flying wing for an airborne wind energy system," *CEAS Aeronautical Journal*, vol. 12, no. 4, pp. 895–906, 2021, ISSN: 1869-5582. DOI: 10.1007/s13272-021-00545-3.

[40] S. Rapp, "Robust automatic pumping cycle operation of airborne wind energy systems," Dissertation, Delft University of Technology, 2021. DOI: 10.4233/uuid:ab2adf33-ef5d-413c-b403-2cfb4f9b6bae.

[41] J. S. Cheema, *The Mass Growth Factor – Snowball Effects in Aircraft Design*. Hamburg : Aircraft Design and Systems Group (AERO), Department of Automotive and Aeronautical Engineering, Hamburg University of Applied Sciences, 2020. DOI: 10.15488/11530.

[42] E. Nguyen Van, L. Fagiano, and S. Schnez, "On the autonomous take-off and landing of tethered wings for airborne wind energy," in *2016 American Control Conference (ACC)*, IEEE, 2016, pp. 4077–4082, ISBN: 978-1-4673-8682-1. DOI: 10.1109/ACC.2016.7525562.

[43] K. van Hussen, E. Dietrich, J. Smeltink, K. Berentsen, *et al.*, *Study on challenges in the commercialisation of airborne wind energy systems*. Luxembourg: Publications Office of the European Union, 2018, ISBN: 978-92-79-80282-9.

[44] M. Erhard and H. Strauch, "Automatic control of pumping cycles for the skysails prototype in airborne wind energy," in *Airborne Wind Energy*, ser. Green Energy and Technology, Ed. R. Schmehl, Singapore: Springer Singapore, 2018, pp. 189–213, ISBN: 978-981-10-1946-3. DOI: 10.1007/978-981-10-1947-0.

[45] R. van der Vlugt, J. Peschel, and R. Schmehl, "Design and experimental characterization of a pumping kite power system," in *Airborne Wind Energy*, ser. SpringerLink Books, Eds. U. Ahrens, M. Diehl, and R. Schmehl, Berlin, Heidelberg: Springer, 2013, pp. 403–425, ISBN: 978-3-642-39964-0. DOI: 10.1007/978-3-642-39965-7.

[46] A. Bormann, M. Ranneberg, P. Kövesdi, C. Gebhardt, *et al.*, "Development of a three-line ground-actuated airborne wind energy converter," in *Airborne Wind Energy*, ser. SpringerLink Books, Eds. U. Ahrens, M. Diehl, and R. Schmehl, Berlin, Heidelberg: Springer, 2013, pp. 427–436, ISBN: 978-3-642-39964-0.

[47] L. Fagiano and S. Schnez, "On the take-off of airborne wind energy systems based on rigid wings," *Renewable Energy*, vol. 107, pp. 473–488, 2017, ISSN: 09601481. DOI: 10.1016/j.renene.2017.02.023.

[48] M. Kruijff and R. Ruiterkamp, "A roadmap towards airborne wind energy in the utility sector," in *Airborne Wind Energy*, ser. Green Energy and Technology, Ed. R. Schmehl, Singapore: Springer Singapore, 2018, pp. 643–662, ISBN: 978-981-10-1946-3. DOI: 10.1007/978-981-10-1947-0.

[49] L. Fagiano, E. Nguyen-Van, F. Rager, S. Schnez, *et al.*, "Automatic take-off of a tethered aircraft for airborne wind energy: Control design and experimental results," *IFAC-PapersOnLine*, vol. 50, no. 1, pp. 11 932–11 937, 2017, ISSN: 24058963. DOI: 10.1016/j.ifacol.2017.08.1456.

[50] SkySails Power, Wrage, S., "Making AWE a reality," in *Airborne Wind Energy Conference (AWEC 2021): Delft University of Technology*, Ed. Delft University of Technology, 2022, pp. 70–77.

[51] EnerKite GmbH, *Green energy from high altitudes*, 2016. [Online]. Available: `https://enerkite.de/en/` (accessed on 03/01/2024).

[52] Ampyx Power, Drenth, S., "Limiting wave conditions for landing airborne wind energy aircraft on a floating platform," in *7th International Airborne Wind Energy Conference: Book of Abstracts*, Eds. M. Diehl, R. Leuthold, and R. Schmehl, 2017, pp. 172–173.

[53] Makani Technologies LLC, D. Mycleod, "Lessons learned from testing makani's energy kite offshore," in *8th International Airborne Wind Energy Conference: Book of Abstracts*, Eds. R. Schmehl and O. Tulloch, 2019, pp. 20–33.

[54] Kitemill, *Taking windpower to new heights*, 2024. [Online]. Available: `https://www.kitemill.com/` (accessed on 03/01/2024).

[55] R. H. Luchsinger, Damian Aregger, Florian Bezard, Dino Costa, *et al.*, "Closing the gap: Pumping cycle kite power with twings," in *6th International Airborne Wind Energy Conference: Book of Abstracts*, Ed. R. Schmehl, 2015, pp. 26–28.

[56] D. Vander Lind, "Analysis and flight test validation of high performance airbornewind turbines," in *Airborne Wind Energy*, ser. SpringerLink Books, Eds. U. Ahrens, M. Diehl, and R. Schmehl, Berlin, Heidelberg: Springer, 2013, pp. 473–490, ISBN: 978-3-642-39964-0. DOI: `10.1007/978-3-642-39965-7`.

[57] P. Echeverri, T. Fricke, G. Homsy, and N. Tucker, *The energy kite: Part i*, Ed. Makani Technologies LLC, 2020. [Online]. Available: `https://x.company/blog/posts/sharing-makani-with-the-world-the-energy-kite-collection/` (accessed on 03/01/2024).

[58] F. Bauer and H. Börngen, "Power electronic topologies of drag power kites," in *8th International Airborne Wind Energy Conference: Book of Abstracts*, Eds. R. Schmehl and O. Tulloch, 2019, pp. 148–151. DOI: `10.4233/uuid:57fd203c-e069-11e9-9fcb-441ea15f7c9c`.

[59] L. Fagiano, M. Quack, F. Bauer, L. Carnel, *et al.*, "Autonomous airborne wind energy systems: Accomplishments and challenges," *Annual Review of Control, Robotics, and Autonomous Systems*, vol. 5, no. 1, pp. 603–631, 2022, ISSN: 2573-5144. DOI: `10.1146/annurev-control-042820-124658`.

[60] K. Nickel and M. Wohlfahrt, *Tailless aircraft in theory and practice* (AIAA education series). Washington, DC: American Institute of Aeronautics and Astronautics, 1994, ISBN: 978-1563470943.

[61] A. R. Weyl, "Stability of tailless aeroplanes," *Aircraft Engineering and Aerospace Technology*, vol. 17, no. 3, pp. 73–81, 1945, ISSN: 0002-2667. DOI: 10.1108/eb031228.

[62] J. K. Northrop, "The development of all–wing aircraft," *The Aeronautical Journal*, vol. 51, no. 438, pp. 481–510, 1947, ISSN: 2398-4600. DOI: 10.1017/S0368393100123624.

[63] P. H. Zipfel, *Modeling and simulation of aerospace vehicle dynamics* (AIAA education series), 3. ed. Reston, Va.: American Institute of Aeronautics and Astronautics Inc, 2014, ISBN: 978-1-62410-250-9.

[64] R. Brockhaus, W. Alles, and R. Luckner, *Flugregelung [Flight control]*, 3. edition. Berlin and Heidelberg: Springer, 2011, ISBN: 978-3-642-01443-7.

[65] E. G. Hemingway and O. M. O'Reilly, "Perspectives on euler angle singularities, gimbal lock, and the orthogonality of applied forces and applied moments," *Multibody System Dynamics*, vol. 44, no. 1, pp. 31–56, 2018, ISSN: 1384-5640. DOI: 10.1007/s11044-018-9620-0.

[66] J. Voight, *Quaternion algebras* (Graduate texts in mathematics). Cham, Switzerland: Springer, 2021, vol. 288, ISBN: 978-3-030-56694-4. DOI: 10.1007/978-3-030-56694-4. [Online]. Available: https://www.zbmath.org/?q=an%3A7261776.

[67] R. Goldman, "Understanding quaternions," *Graphical Models*, vol. 73, no. 2, pp. 21–49, 2011, ISSN: 15240703. DOI: 10.1016/j.gmod.2010.10.004.

[68] Wm. R. Hamilton, "Theory of quaternions," in *The Royal Irish Academy*, vol. 3, 1844, pp. 1–16.

[69] M. E. Mortenson, *Mortenson, Michael E. Mathematics for computer graphics applications*. Industrial Press Inc., 1999.

[70] J. C. Hart, G. K. Francis, and L. H. Kauffman, "Visualizing quaternion rotation," *ACM Transactions on Graphics*, vol. 13, no. 3, pp. 256–276, 1994, ISSN: 0730-0301. DOI: 10.1145/195784.197480.

[71] K. Großekatthöfer and Z. Yoon, *Introduction into quaternions for spacecraft attitude representation*, Ed. TU Berlin, Department of Astronautics and Aeronautics, 2012.

[72] A. Bani Younes and D. Mortari, "Derivation of all attitude error governing equations for attitude filtering and control," *Sensors (Basel, Switzerland)*, vol. 19, no. 21, 2019. DOI: 10.3390/s19214682.

[73] E. Fresk and G. Nikolakopoulos, "Full quaternion based attitude control for a quadrotor," in *2013 European Control Conference (ECC)*, IEEE, 2013, pp. 3864–3869, ISBN: 978-3-033-03962-9. DOI: 10.23919/ECC.2013.6669617.

[74] K. Shoemake, "Animating rotation with quaternion curves," in *Proceedings of the 12th Annual Conference on Computer Graphics and Interactive Techniques*, ser. SIGGRAPH '85, New York, NY, USA: ACM Press, 1985, pp. 245–254. DOI: 10.1145/325334.325242.

[75] J. Krimphove, M. Schütt, P. Osterloh, and D. Moormann, "Trimmed flight states of an over-actuated tilt-wing aircraft for linear controller synthesis," in *2023 IEEE Conference on Control Technology and Applications (CCTA)*, IEEE, 2023, pp. 360–366, ISBN: 979-8-3503-3544-6. DOI: 10.1109/CCTA54093.2023.10252262.

[76] M. Schütt, "State controller for flight performance oriented tilt-wing aircraft," Dissertation, RWTH Aachen University, 2019. DOI: 10.18154/RWTH-2019-06783. [Online]. Available: https://publications.rwth-aachen.de/record/764354.

[77] R. Vepa, *Flight Dynamics, Simulation, and Control: For Rigid and Flexible Aircraft*, 2nd ed. Milton: Taylor & Francis Group, 2023, ISBN: 9781000848021. [Online]. Available: https://ebookcentral.proquest.com/lib/kxp/detail.action?docID=7211479.

[78] R. C. Nelson, *Flight stability and automatic control*, 2. ed, internat. ed. Boston, Mass. u.a.: McGraw Hill, 1998, ISBN: 0-07-115838-3. [Online]. Available: https://permalink.obvsg.at/AC11460424.

[79] D. Hinrichsen and A. J. Pritchard, "Stability theory," in *Mathematical Systems Theory I*, ser. Texts in Applied Mathematics, Eds. J. E. Marsden, L. Sirovich, S. S. Antman, D. Hinrichsen, *et al.*, vol. 48, Berlin, Heidelberg: Springer Berlin Heidelberg, 2005, pp. 193–368, ISBN: 978-3-540-44125-0. DOI: 10.1007/3-540-26410-8.

[80] US Air Force Department, *Military standard - flying qualities of piloted aircraft: Mil-std-1797a*, 2004.

[81] R. F. Stengel, *Flight dynamics*. Princeton, NJ: Princeton University Press, 2004, ISBN: 978-0-691-11407-1.

[82] R. H. Liebeck and P. P. Camacho, "Airfoil design at low reynolds number with constrained pitching moment," in *Proceedings of the Conference on Low Reynolds Number Airfoil Aerodynamics*, 1985, pp. 27–35.

[83] P. Marqués, "Flight stability and control of tailless lambda unmanned aircraft," *International Journal of Unmanned Systems*, vol. 1, no. 2, pp. 1–4, 2013.

[84] B. Montgomerie, *Methods for root effects, tip effects and extending the angle of attack range to +- 180 deg., with application to aerodynamics for blades on wind turbines and propellers*, Ed. Swedish Defence Research Agency, Sweden, 2004.

[85] J. D. Anderson, *Fundamentals of aerodynamics* (McGraw-Hill series in aeronautical and aerospace engineering), 5. ed. in SI Units. New York, NY: McGraw-Hill, 2011, ISBN: 978-1-259-01028-6.

[86] E. J. J. Smeur, M. Bronz, and G. C. H. E. de Croon, "Incremental control and guidance of hybrid aircraft applied to a tailsitter unmanned air vehicle," *Journal of Guidance, Control, and Dynamics*, vol. 43, no. 2, pp. 274–287, 2020, ISSN: 0731-5090. DOI: 10.2514/1.G004520.

[87] M. H. Sadraey, "Lateral-directional stability," in *Flight Stability and Control*, ser. Synthesis Lectures on Mechanical Engineering, Ed. M. H. Sadraey, Cham: Springer International Publishing, 2022, pp. 109–157, ISBN: 978-3-031-18764-3. DOI: 10.1007/978-3-031-18765-0.

[88] T. Van Milligan, "Theory and practice of using flying wings," *Apogee Components*, pp. 1–7, 2000.

[89] P. Hartmann, "Predictive flight path control for tilt-wing aircraft," Dissertation, RWTH Aachen University, 2017. DOI: 10.18154/RWTH-2017-10495.

[90] IHS ESDU, *ESDU 85020: Characteristics of atmospheric turbulence near the ground*. London: ESDU International plc, 2008, ISBN: 9780856795268.

[91] D. F. Duda, "Control of a flight system including tether model for an airborne wind power plant," Master Thesis, RWTH Aachen University, 2019.

[92] R. Hooke, *De potentia restitutiva, or of spring. explaining the power of springing bodies*, London, 1678.

[93] W. J. Lewis, *Tension structures: Form and behaviour*. London: Thomas Telford, 2003, ISBN: 0 7277 3236 6.

[94] N. Bigi, A. Nême, K. Roncin, J.-B. Leroux, *et al.*, "Analytical tether model for static kite flight," in *Airborne Wind Energy*, ser. Green Energy and Technology, Ed. R. Schmehl, Singapore: Springer Singapore, 2018, pp. 57–78, ISBN: 978-981-10-1946-3.

[95] D. F. Duda, H. Fuest, T. Islam, T. Ostermann, *et al.*, "Hybrid modeling approach for the tether of an airborne wind energy system," *CEAS Aeronautical Journal*, vol. 13, no. 3, pp. 627–637, 2022, ISSN: 1869-5582. DOI: 10.1007/s13272-022-00581-7.

[96] M. Drela, "Xfoil: An analysis and design system for low reynolds number airfoils," in *Low Reynolds Number Aerodynamics*, ser. Lecture Notes in Engineering, Eds. C. A. Brebbia, S. A. Orszag, J. H. Seinfeld, P. Spanos, *et al.*, vol. 54, Berlin, Heidelberg: Springer Berlin Heidelberg, 1989, pp. 1–12, ISBN: 978-3-540-51884-6. DOI: 10.1007/978-3-642-84010-4.

[97] X. Chen, "Modeling of the influence of sideslip on the aerodynamics of a flying wing," Bachelor Thesis, RWTH Aachen University, 2024.

[98] International Organization for Standardization, *ISO 1151-1: Flight dynamics; concepts, quantities and symbols*, 1988.

[99] A. Deperrois, *Results vs prediction: About xflr5 calculations and experimental measurements*, 2009. [Online]. Available: www.xflr5.tech/docs/Results_vs_Prediction.pdf (accessed on 06/01/2024).

[100] A. Deperrois, *Analysis of foils and wings operating at low reynolds numbers*, 2013. [Online]. Available: www.xflr5.tech/xflr5.htm (accessed on 06/01/2024).

[101] A. Deperrois, *Part i: Theoretical overview: Overview of the theoretical background in xflr5*, 2019. [Online]. Available: http://www.xflr5.tech/docs/Part%20I:%20Theoretical%20overview.pdf (accessed on 06/01/2024).

[102] T. Loeser, D. Vicroy, and A. Schuette, "Saccon static wind tunnel tests at dnw-nwb and 14x22 nasa larc," in *28th AIAA Applied Aerodynamics Conference*, Reston, Virigina: American Institute of Aeronautics and Astronautics, 2010, ISBN: 978-1-62410-141-0. DOI: 10.2514/6.2010-4393.

[103] Y. Jung, D. Shim, and N. Ananthkrishnan, "Transition control of near-hover to cruise transition of a tail sitter UAV," in *AIAA Atmospheric Flight Mechanics Conference*, Reston, Virigina: American Institute of Aeronautics and Astronautics, 2010, ISBN: 978-1-62410-151-9. DOI: 10.2514/6.2010-7508.

[104] S. Verling, B. Weibel, M. Boosfeld, K. Alexis, *et al.*, "Full attitude control of a VTOL tailsitter UAV," in *2016 IEEE International Conference on Robotics and Automation (ICRA)*, IEEE, 2016, pp. 3006–3012, ISBN: 978-1-4673-8026-3. DOI: 10.1109/ICRA.2016.7487466.

[105] B. Li, W. Zhou, J. Sun, C.-Y. Wen, *et al.*, "Development of model predictive controller for a tail-sitter VTOL UAV in hover flight," *Sensors (Basel, Switzerland)*, vol. 18, no. 9, 2018. DOI: 10.3390/s18092859.

[106] Z. Omar, B. Cees, and R. Hill, "The development of a new VTOL UAV configuration for law enforcement," in *International Conference on Mechanical & Manufacturing Engineering*, 2008, ISBN: 97-98-2963-59-2.

[107] Aerovel Corporation, *Aerovel flexrotor sets vtol endurance mark*, 2017. [Online]. Available: `https://aerovel.com/flexrotor-vtol-endurance/` (accessed on 01/03/2024).

[108] R. H. Stone, "The t-wing tail-sitter research uav," in *2002 Biennial International Powered Lift Conference and Exhibit*, Reston, Virigina: American Institute of Aeronautics and Astronautics, 2002, ISBN: 978-1-62410-109-0. DOI: `10.2514/6.2002-5970`.

[109] Y. Jung and D. H. Shim, "Development and application of controller for transition flight of tail-sitter UAV," *Journal of Intelligent & Robotic Systems*, vol. 65, no. 1-4, pp. 137–152, 2012, ISSN: 0921-0296. DOI: `10.1007/s10846-011-9585-1`.

[110] A. Maqsood and T. Go, "Study on aerodynamic-assisted transition control technique for versatile UAV," in *47th AIAA Aerospace Sciences Meeting including The New Horizons Forum and Aerospace Exposition*, Reston, Virigina: American Institute of Aeronautics and Astronautics, 2009, ISBN: 978-1-60086-973-0. DOI: `10.2514/6.2009-60`.

[111] N. Raj, R. Banavar, Abhishek, and M. Kothari, "Attitude control of novel tail sitter: Swiveling biplane–quadrotor," *Journal of Guidance, Control, and Dynamics*, vol. 43, no. 3, pp. 599–607, 2020, ISSN: 0731-5090. DOI: `10.2514/1.G004697`.

[112] Y. Ke, K. Wang, and B. M. Chen, "Design and implementation of a hybrid UAV with model-based flight capabilities," *IEEE/ASME Transactions on Mechatronics*, vol. 23, no. 3, pp. 1114–1125, 2018, ISSN: 1083-4435. DOI: `10.1109/TMECH.2018.2820222`.

[113] P. Casau, D. Cabecinhas, and C. Silvestre, "Autonomous transition flight for a vertical take-off and landing aircraft," in *IEEE Conference on Decision and Control and European Control Conference*, IEEE, 2011, pp. 3974–3979, ISBN: 978-1-61284-801-3. DOI: `10.1109/CDC.2011.6160819`.

[114] R. H. Stone and G. Clarke, *The T-Wing: A VTOL UAV for defense and civilian applications*, Ed. University of Sydney, 2001.

[115] S. Fuhrer, S. Verling, T. Stastny, and R. Siegwart, "Fault-tolerant flight control of a VTOL tailsitter UAV," in *2019 International Conference on Robotics and Automation (ICRA)*, IEEE, 2019, pp. 4134–4140, ISBN: 978-1-5386-6027-0. DOI: `10.1109/ICRA.2019.8793467`.

[116] J. Liang, Q. Fei, B. Wang, and Q. Geng, "Tailsitter VTOL flying wing aircraft attitude control," in *2016 31st Youth Academic Annual Conference of Chinese Association of Automation (YAC)*, IEEE, 2016, pp. 439–443, ISBN: 978-1-5090-4423-8. DOI: `10.1109/YAC.2016.7804934`.

[117] R. Ritz and R. D'Andrea, "A global strategy for tailsitter hover control," in *Robotics Research*, ser. Springer Proceedings in Advanced Robotics, Eds. A. Bicchi and W. Burgard, vol. 2, Cham: Springer International Publishing, 2018, pp. 21–37, ISBN: 978-3-319-51531-1. DOI: 10.1007/978-3-319-51532-8.

[118] S. Verling, "Towards robust operation of VTOL tailsitters," Dissertation, ETH Zurich, 2020. DOI: 10.3929/ethz-b-000475904.

[119] R. Ritz, "Enhancing the capabilities of flying machines: Cooperative payload carrying onboard learning and tailsitter control," Dissertation, ETH Zurich, 2017.

[120] R. H. Stone, P. Anderson, C. Hutchison, A. Tsai, *et al.*, "Flight testing of the t-wing tail-sitter unmanned air vehicle," *Journal of Aircraft*, vol. 45, no. 2, pp. 673–685, 2008, ISSN: 0021-8669. DOI: 10.2514/1.32750.

[121] R. H. Stone, "Control architecture for a tail-sitter unmanned air vehicle," in *5th Asian Control Conference*, Piscataway, NJ: IEEE, 2004, pp. 736–744, ISBN: 0-7803-8873-9.

[122] W. Wang, J. Zhu, M. Kuang, X. Yuan, *et al.*, "Design and hovering control of a twin rotor tail-sitter UAV," *Science China Information Sciences*, vol. 62, no. 9, 2019, ISSN: 1674-733X. DOI: 10.1007/s11432-018-9733-8.

[123] D. Kubo and S. Suzuki, "Transitional flight control of tail-sitter vertical takeoff and landing mini unmanned aerial vehicle," in *AIAA Infotech@Aerospace 2007 Conference and Exhibit*, Reston, Virigina: American Institute of Aeronautics and Astronautics, 2007, ISBN: 978-1-62410-017-8. DOI: 10.2514/6.2007-2752.

[124] D. Kubo and S. Suzuki, "Tail-sitter vertical takeoff and landing unmanned aerial vehicle: Transitional flight analysis," *Journal of Aircraft*, vol. 45, no. 1, pp. 292–297, 2008, ISSN: 0021-8669. DOI: 10.2514/1.30122.

[125] Y. Yang, J. Zhu, and J. Yang, "INDI-based transitional flight control and stability analysis of a tail-sitter UAV," in *2020 IEEE International Conference on Systems, Man, and Cybernetics (SMC)*, IEEE, 2020, pp. 1420–1426, ISBN: 978-1-7281-8526-2. DOI: 10.1109/SMC42975.2020.9283378.

[126] E. Tal and S. Karaman, "Global incremental flight control for agile maneuvering of a tailsitter flying wing," *Journal of Guidance, Control, and Dynamics*, vol. 45, no. 12, pp. 2332–2349, 2022, ISSN: 0731-5090. DOI: 10.2514/1.G006645.

[127] A. Oosedo, S. Abiko, A. Konno, T. Koizumi, *et al.*, "Development of a quad rotor tail-sitter VTOL UAV without control surfaces and experimental verification," in *2013 IEEE International Conference on Robotics and Automation*, IEEE, 2013, pp. 317–322, ISBN: 978-1-4673-5643-5. DOI: 10.1109/ICRA.2013.6630594.

[128] M. Hochstenbach, C. Notteboom, B. Theys, and J. de Schutter, "Design and control of an unmanned aerial vehicle for autonomous parcel delivery with transition from vertical take-off to forward flight – VertiKUL, a quadcopter tailsitter," *International Journal of Micro Air Vehicles*, vol. 7, no. 4, pp. 395–405, 2015, ISSN: 1756-8293. DOI: 10.1260/1756-8293.7.4.395.

[129] X. Lyu, H. Gu, Y. Wang, Z. Li, *et al.*, "Design and implementation of a quadrotor tail-sitter VTOL UAV," in *2017 IEEE International Conference on Robotics and Automation (ICRA)*, IEEE, 2017, pp. 3924–3930, ISBN: 978-1-5090-4633-1. DOI: 10.1109/ICRA.2017.7989452.

[130] A. Oosedo, S. Abiko, A. Konno, and M. Uchiyama, "Optimal transition from hovering to level-flight of a quadrotor tail-sitter UAV," *Autonomous Robots*, vol. 41, no. 5, pp. 1143–1159, 2017, ISSN: 0929-5593. DOI: 10.1007/s10514-016-9599-4.

[131] Y. Gupta, J. Dumon, and A. Hably, "Power curve analysis of on-ground airborne wind energy systems," in *2019 IEEE International Conference on Industrial Technology*, IEEE, 2019, pp. 175–180, ISBN: 978-1-5386-6376-9. DOI: 10.1109/ICIT.2019.8755195.

[132] D. F. Duda, H. Fuest, T. Islam, and D. Moormann, "Flight guidance concept for the launching and landing phase of a flying wing used in an airborne wind energy system," in *Wind Energy Science Discussions*, 2024, pp. 1–25. DOI: 10.5194/wes-2024-90.

[133] H. G. Bader, "Flugeigenschaften (flight characteristics)," in *Flugzeugbaukunde (Aircraft Construction)*, Ed. H. G. Bader, Berlin, Heidelberg: Springer Berlin Heidelberg, 1924, pp. 117–121, ISBN: 978-3-642-47106-3. DOI: 10.1007/978-3-642-47354-8.

[134] L. Keviczky, R. Bars, J. Hetthéssy, and C. Bányász, *Control engineering* (Advanced textbooks in control and signal processing). Singapore: Springer, 2019, ISBN: 978-981-10-8296-2.

[135] D. T. McRuer, I. Ashkenas, and D. Graham, *Aircraft dynamics and automatic control*. Princeton, NJ: Princeton University Press, 1973, ISBN: 0-691-08083-6. [Online]. Available: http://www.loc.gov/catdir/description/prin051/73134250.html.

[136] F. Amato, C. Cosentino, and A. Merola, "On the region of attraction of nonlinear quadratic systems," *Automatica*, vol. 43, no. 12, pp. 2119–2123, 2007, ISSN: 00051098. DOI: 10.1016/j.automatica.2007.03.022.

[137] A. P. White, G. Zhu, and J. Choi, *Linear parameter-varying control for engineering applications* (SpringerBriefs in electrical and computer engineering Control, automation and robotics). London: Springer, 2013, ISBN: 1447150392.

[138] E. Ahbe, "Region of attraction analysis of uncertain equilibrium points and limit cycles - with application to airborne wind energy systems," Dissertation, ETH Zurich, 2020. DOI: 10.3929/ethz-b-000461553.

[139] J. L. Moore, "Robust post-stall perching with a fixed-wing UAV," Dissertation, Massachusetts Institute of Technology, 2014.

[140] Y. Yang, "Analytic LQR design for spacecraft control system based on quaternion model," *Journal of Aerospace Engineering*, vol. 25, no. 3, pp. 448–453, 2012, ISSN: 0893-1321. DOI: 10.1061/(ASCE)AS.1943-5525.0000142.

[141] B. D. O. Anderson, B. D. Anderson, and J. B. Moore, *Optimal control: Linear quadratic methods* (Dover books on engineering), Dover ed., augmented republ. of the ed. 1990. Mineola, NY: Dover Publications, 2007, ISBN: 9780486457666.

[142] T. Miquel, *Introduction to optimal control*, Ed. Ecole nationale de l'aviation civile, 2022.

[143] D. F. Duda, H. Fuest, J. Müller, T. Islam, *et al.*, "Incremental nonlinear dynamic inversion controller for a flying wing operated in an airborne wind energy system," in *ICAS*, Ed. International Council of the Aeronautical Sciences, Florence, Italy, 2024.

[144] E. J. J. Smeur, Q. Chu, and G. C. de Croon, "Adaptive incremental nonlinear dynamic inversion for attitude control of micro air vehicles," in *Journal of Guidance, Control, and Dynamics*, 2016, pp. 450–461. DOI: 10.2514/1.G001490.

[145] S. Sieberling, Chu, Qiping, P., and J. A. Mulder, "Robust flight control using incremental nonlinear dynamic inversion and angular acceleration prediction," in *Journal of Guidance, Control, and Dynamics*, 2010, pp. 1732–1742. DOI: 10.2514/1.49978.

[146] R. C. van't Veld, E. van Kampen, and Q. P. Chu, "Stability and robustness analysis and improvements for incremental nonlinear dynamic inversion control," in *AIAA Guidance, Navigation, and Control Conference 2018*, Red Hook, NY: Curran Associates Inc, 2018, ISBN: 978-1-62410-526-5. DOI: 10.2514/6.2018-1127.

[147] F. Binz, "Robust, fault-tolerant control of aircraft with hovering capability," Dissertation, RWTH Aachen University, 2020.

[148] Y. Huang, Y. Zhang, D. M. Pool, O. Stroosma, *et al.*, "Time-delay margin and robustness of incremental nonlinear dynamic inversion control," in *Journal of Guidance, Control, and Dynamics*, 2022, pp. 394–404.

[149] E. Bulka and M. Nahon, "Autonomous control of agile fixed-wing UAVs performing aerobatic maneuvers," in *2017 International Conference on Unmanned Aircraft Systems (ICUAS)*, IEEE, 2017, pp. 104–113, ISBN: 978-1-5090-4495-5. DOI: 10.1109/ICUAS.2017.7991437.

[150] N. B. Knoebel and T. W. McLain, "Adaptive quaternion control of a miniature tailsitter UAV," in *American Control Conference*, IEEE, 2008, pp. 2340–2345, ISBN: 978-1-4244-2078-0. DOI: 10.1109/ACC.2008.4586841.

[151] T. Matsumoto, K. Kita, R. Suzuki, A. Oosedo, *et al.*, "A hovering control strategy for a tail-sitter VTOL UAV that increases stability against large disturbance," in *2010 IEEE International Conference on Robotics and Automation*, IEEE, 2010, pp. 54–59, ISBN: 978-1-4244-5038-1. DOI: 10.1109/ROBOT.2010.5509183.

[152] K. Glover, "A tutorial on hankel-norm approximation," in *From Data to Model*, Ed. J. C. Willems, Berlin, Heidelberg: Springer Berlin Heidelberg, 1989, pp. 26–48, ISBN: 978-3-642-75009-0. DOI: 10.1007/978-3-642-75007-6.

[153] M. J. Grimble, M. A. Johnson, E. F. Camacho, and C. Bordons, *Model Predictive control*. London: Springer London, 2007, ISBN: 978-1-85233-694-3. DOI: 10.1007/978-0-85729-398-5.

[154] M. Armbruster, "Modellprädiktive regelung zur trajektorienplanung der transition eines senkrechtstartfähigen nurflüglers [model predictive control for trajectory planning of the transition of a flying wing with vertical takeoff capability]," Master Thesis, RWTH Aachen University, 2024.

[155] X. Wang, E.-J. van Kampen, Q. Chu, and P. Lu, "Stability analysis for incremental nonlinear dynamic inversion control," *Journal of Guidance, Control, and Dynamics*, vol. 42, no. 5, pp. 1116–1129, 2019, ISSN: 0731-5090. DOI: 10.2514/1.G003791.

[156] J. Lunze, *Regelungstechnik 2 [Control Technology 2]*. Berlin, Heidelberg: Springer Berlin Heidelberg, 2020, ISBN: 978-3-662-60759-6. DOI: 10.1007/978-3-662-60760-2.

[157] K. Glover, "H-infinity control," in *Encyclopedia of Systems and Control*, Eds. J. Baillieul and T. Samad, London: Springer London, 2013, pp. 1–9, ISBN: 978-1-4471-5102-9. DOI: 10.1007/978-1-4471-5102-9.

[158] T. Benson, *Shape effects on drag*, Ed. N. Glenn Research Center, 2010.

[159] S. F. Hoerner, *Fluid-dynamic drag: Practical information on aerodynamic drag and hydrodynamic resistance*, Washington, DC, 1965.

[160] M. Koken, *The experimental determination of the moment of inertia of a model airplane*, Ed. Honors Research Projects, 2017.

[161] W.-H. Chen, "Calculation of frequency response envelope for dynamic systems with uncertain parameters," *Journal of Dynamic Systems, Measurement, and Control*, vol. 133, no. 6, 2011, ISSN: 0022-0434. DOI: 10.1115/1.4004068.

[162] N. Tan, "Magnitude and phase envelopes of systems with affine linear uncertainty," in *UKACC International Conference on Control*, IEE, 1998, pp. 1039–1044, ISBN: 0 85296 708 X. DOI: 10.1049/cp:19980372.

[163] R. L. Herman, *An Introduction to Fourier Analysis*. Chapman and Hall/CRC, 2016, ISBN: 9781315367064. DOI: 10.1201/9781315367064.

[164] M. Ranneberg, D. Wölfle, A. Bormann, P. Rohde, *et al.*, "Fast power curve and yield estimation of pumping airborne wind energy systems," in *Airborne Wind Energy*, ser. Green Energy and Technology, Ed. R. Schmehl, Singapore: Springer Singapore, 2018, pp. 623–641, ISBN: 978-981-10-1946-3. DOI: 10.1007/978-981-10-1947-0.

[165] D.-W. Gu, P. H. Petkov, and M. M. Konstantinov, "Mu-synthesis," in *Robust Control Design with MATLAB*, ser. Advanced textbooks in control and signal processing, London: Springer London, 2013, pp. 203–219, ISBN: 978-1-4471-4681-0. DOI: 10.1007/978-1-4471-4682-7.

[166] U. Fechner, R. van der Vlugt, E. Schreuder, and R. Schmehl, "Dynamic model of a pumping kite power system," *Renewable Energy*, vol. 83, pp. 705–716, 2015, ISSN: 09601481. DOI: 10.1016/j.renene.2015.04.028.

Appendix

A. Quaternion Calculations

The following represents an extract of relevant calculations of quaternions, based on [71].

Quaternion Conjugate

$$\underline{q}^* = \cos\left(\frac{\Theta_q}{2}\right) - \vec{u}_q \cdot \sin\left(\frac{\Theta_q}{2}\right) \in \mathbb{H} \tag{A}$$

Quaternion Norm

$$||\underline{q}|| = \sqrt{q_\mathrm{s}^2 + q_i^2 + q_j^2 + q_k^2} \in \mathbb{R} \tag{B}$$

with:

$$\begin{aligned} q_\mathrm{s} &= \cos\left(\frac{\Theta_q}{2}\right) \\ q_i &= u_i \cdot \sin\left(\frac{\Theta_q}{2}\right) \\ q_j &= u_j \cdot \sin\left(\frac{\Theta_q}{2}\right) \\ q_k &= u_k \cdot \sin\left(\frac{\Theta_q}{2}\right) \end{aligned}$$

Quaternion Inverse

$$\underline{q}^{-1} = \frac{\underline{q}^*}{||\underline{q}||^2} \in \mathbb{H} \tag{C}$$

Kronecker Product between two Quaternions A and B

$$\underline{q}_\mathrm{A} \otimes \underline{q}_\mathrm{B} = \begin{bmatrix} q_{\mathrm{s,A}} \cdot q_{\mathrm{s,B}} - \vec{q}_{\mathrm{v,A}} \cdot \vec{q}_{\mathrm{v,B}} \\ q_{\mathrm{s,A}} \cdot \vec{q}_{\mathrm{v,B}} + q_{\mathrm{s,B}} \cdot \vec{q}_{\mathrm{v,A}} + \vec{q}_{\mathrm{v,A}} \times \vec{q}_{\mathrm{v,B}} \end{bmatrix} \in \mathbb{H} \tag{D}$$

with:

$$\vec{q}_{\mathrm{v}} = \begin{bmatrix} q_i \\ q_j \\ q_k \end{bmatrix} \tag{E}$$

Transformation of a Vector from Coordinate System A to System B

$$\begin{bmatrix} 0 \\ \vec{v}_{\mathrm{B}} \end{bmatrix} = \underline{q}_{\mathrm{BA}} \otimes \begin{bmatrix} 0 \\ \vec{v}_{\mathrm{A}} \end{bmatrix} \otimes \underline{q}_{\mathrm{BA}}^{-1} \tag{F}$$

Rotation Angle between two Quaternions A and B

$$\cos(\Omega_q) = \underline{q}_{\mathrm{A}} \otimes \underline{q}_{\mathrm{B}} \tag{G}$$

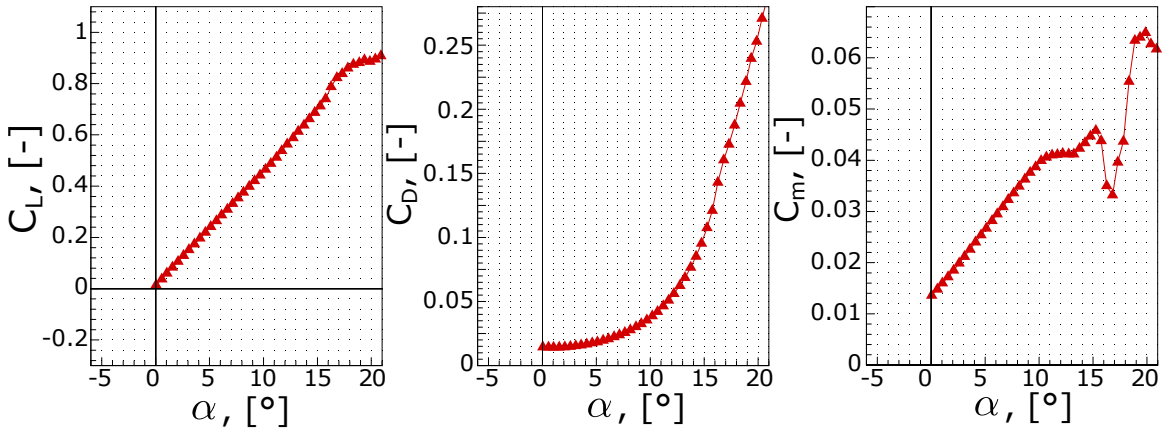
B. AWE System Data and Verification

Tether parameters

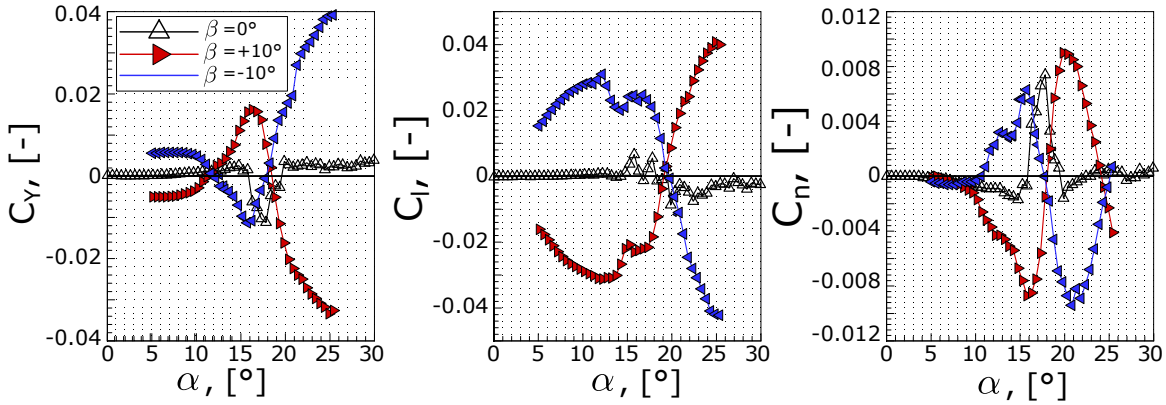
Parameter	Stiffness M_t	Diameter d_t	Density ρ_t	Drag $C_{D,t}$
Value	610 $^{kN}/_{m}$	4 mm	970 $^{kg}/_{m^3}$	0.97

Table A.: Relevant tether parameters following [166].

Slip Angle Verification



(a) Coefficients of the longitudinal motion at $\beta = 0°$.



(b) Coefficients of the lateral motion.

Figure A.: Results of wind tunnel experiments of a blended wing body with sideslip, showing the reversed trends of the lateral coefficients when stall effects occur. [102]

C. Flight Mechanics

Lateral Yaw-Roll Motion

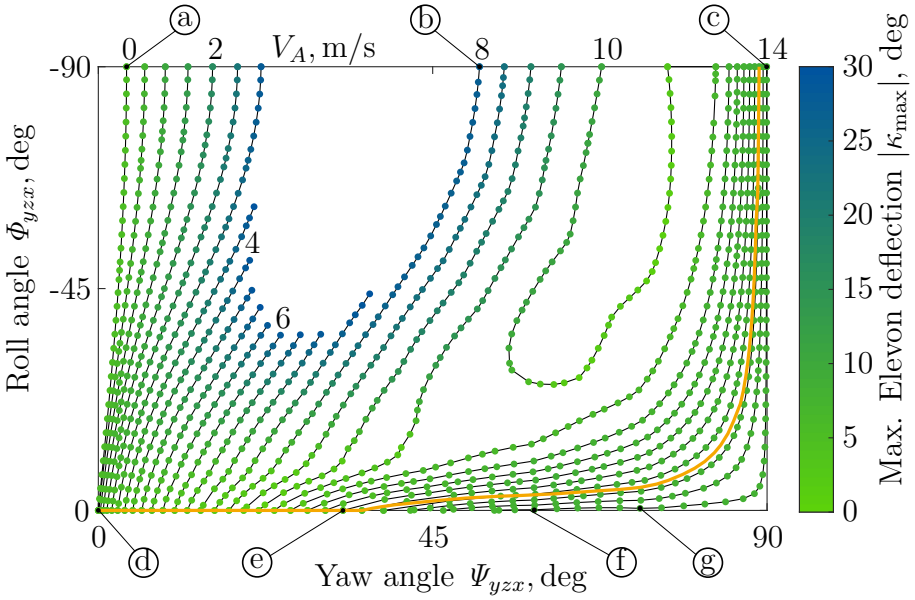


Figure B.: Trim diagram for the lateral motion as a function of the Euler angles.

Control effectiveness

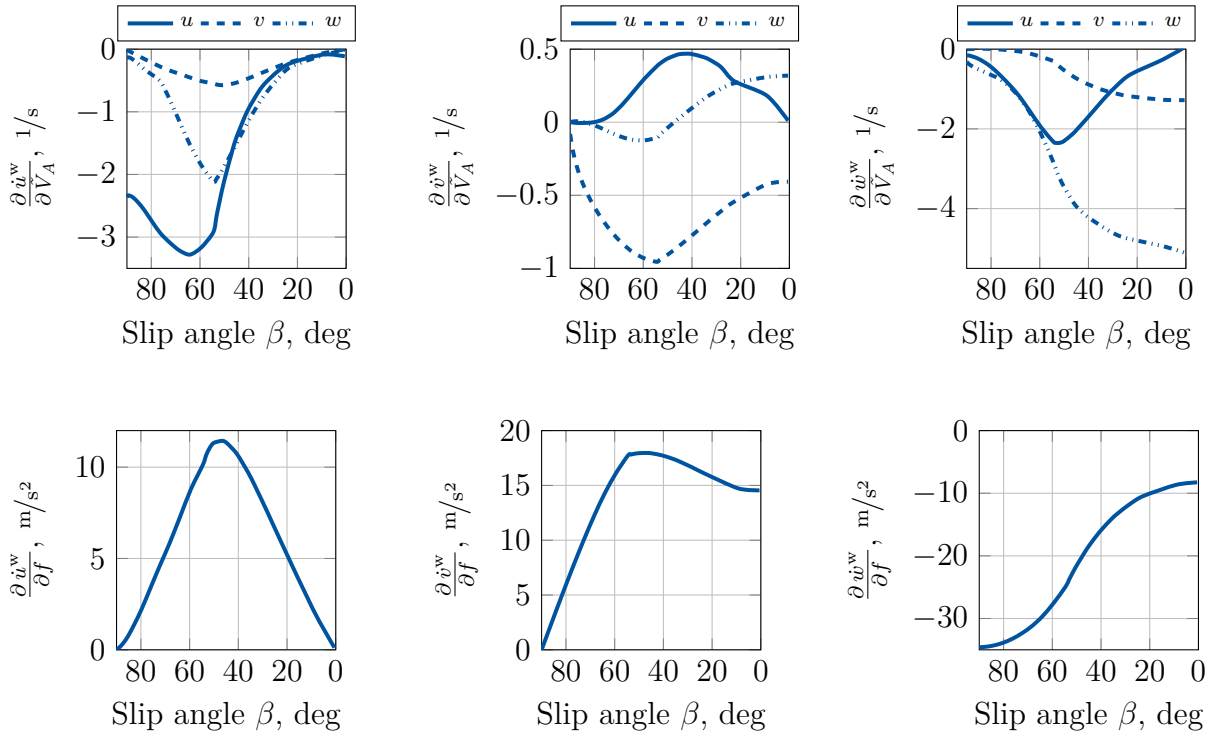


Figure C.: Control effectiveness of throttle, and damping effects during the transition.

D. LQR and Robustness Design

Solution of the optimal feedback gain

The optimal feedback gain can be calculated by Eq. H. The matrix P is found by solving the Riccati equation I.

$$K_{\mathrm{LQR}} = R^{-1}(PB + N)^{\mathrm{T}} \tag{H}$$

Riccati equation:
$$0 = PA_m + A_m^{\mathrm{T}}P - PBR^{-1}B^{\mathrm{T}}P + Q_m \tag{I}$$

with
$$A_m = A - BR^{-1}N^{\mathrm{T}} \tag{J}$$

with
$$Q_m = Q - NR^{-1}N^{\mathrm{T}} \tag{K}$$

Weighting matrices of the cost function

V_A, m/s	$Q_{1,1}$	$Q_{2,2}$	$Q_{3,3}$	$Q_{4,4}$	$Q_{5,5}$	$Q_{6,6}$	$Q_{7,7}$	$Q_{8,8}$	$Q_{9,9}$
$[0-12]$	10	10	10	10	10	10	1	1	1
$[12-12.7]$	10	10	10	10	10	10	1	1	1
$[12.7-13]$	10	10	10	10	10	10	1	1	1

Table B.: Entries of the weighting matrix of $\vec{Q} \in \mathbb{N}^{17x17}$. All remaining entries are zero.

V_A, m/s	$R_{1,1}$	$R_{2,2}$	$R_{3,3}$	$R_{4,4}$
$[0-12]$	1000	100	1000	1000
$[12-12.7]$	1000	1000	1000	1000
$[12.7-13]$	1000	1000	1000	1000

Table C.: Entries of the weighting matrix of $\vec{R} \in \mathbb{N}^{4x4}$. All remaining entries are zero.

V_A, m/s	$N_{4,1}$	$N_{5,1}$
$[0-12]$	0	0
$[12-12.7]$	100	100
$[12.7-13]$	0	0

Table D.: Entries of the weighting matrix of $\vec{N} \in \mathbb{N}^{17x4}$. All remaining entries are zero.

Closed-Loop Systems for Robustness Analysis

The closed-loop system of the pitch controlled system is given in Eq. L, including the influence of the wind field. The state vector is given by $\vec{x} = \left[\int \Delta u_g^{\mathrm{w}}, \delta u_g^{\mathrm{w}}, \delta\theta, \delta q, \delta\dot{q}\right]^\top$. The input is defined by $\vec{u} = [\delta\psi_W, \delta\psi_{zxy}]^\top$. The output y is the aerodynamic velocity u_a^{w}.

$$\dot{\vec{x}} = \begin{pmatrix} 0 & -1 & 0 & 0 & 0 \\ 0 & -2{\cdot}C_u{\cdot}u_{G,0} & -g & 0 & 0 \\ 0 & 0 & 0 & 1 & 0 \\ 0 & -2{\cdot}C_q{\cdot}u_{G,0} & 0 & 0 & 1 \\ K_x^{\mathrm{closed}} & K_u^{\mathrm{closed}} & K_\theta^{\mathrm{closed}} & K_q^{\mathrm{closed}} & K_{\dot{q}}^{\mathrm{closed}} \end{pmatrix} \vec{x} + \begin{pmatrix} 0 & 0 \\ 2{\cdot}C_u{\cdot}V_{W,0}^2{\cdot}\Psi_{W,0} & -2{\cdot}C_u{\cdot}V_{W,0}^2{\cdot}\Psi_{W,0} \\ 0 & 0 \\ -2{\cdot}C_q{\cdot}V_{W,0}^2{\cdot}\Psi_{W,0} & 2{\cdot}C_q{\cdot}V_{W,0}^2{\cdot}\Psi_{W,0} \\ 0 & 0 \end{pmatrix} \vec{u} \qquad \text{(L)}$$

$$y = \begin{pmatrix} 0 & 1 & 0 & 0 & 0 \end{pmatrix} \vec{x} + \begin{pmatrix} -V_{W,0} & V_{W,0} \end{pmatrix} \vec{u}$$

$$K_x^{\mathrm{closed}} = -\frac{K_{\dot{q}}^{\mathrm{DC}} \cdot K_\theta^{\mathrm{att}} \cdot K_x^{\mathrm{vel}}}{T_e} \qquad K_u^{\mathrm{closed}} = -\frac{K_{\dot{q}}^{\mathrm{DC}} \cdot K_\theta^{\mathrm{att}} \cdot K_u^{\mathrm{vel}}}{T_e}$$

$$K_\theta^{\mathrm{closed}} = -\frac{K_{\dot{q}}^{\mathrm{DC}} \cdot K_\theta^{\mathrm{att}} \cdot (1 + K_\theta^{\mathrm{vel}})}{T_e} \qquad K_q^{\mathrm{closed}} = -\frac{K_{\dot{q}}^{\mathrm{DC}} \cdot (K_q^{\mathrm{att}} + K_\theta^{\mathrm{att}} \cdot K_q^{\mathrm{vel}})}{T_e}$$

$$K_{\dot{q}}^{\mathrm{closed}} = -\frac{1 + K_{\dot{q}}^{\mathrm{DC}} \cdot (K_{\dot{q}}^{\mathrm{att}} + K_\theta^{\mathrm{att}} \cdot K_{\dot{q}}^{\mathrm{vel}})}{T_e} \qquad \text{(M)}$$

The closed-loop system of the roll controlled system is given in Eq. N. The state vector is given by $\vec{x} = \left[\delta\psi, \delta p, \delta\dot{p}, \delta\psi^{\mathrm{cmd}}\right]^\top$. The input is defined by $\vec{u} = \delta\theta^{\mathrm{cmd}}$.

$$\dot{\vec{x}} = \begin{pmatrix} 0 & 1 & 0 & 0 \\ 0 & -2 \cdot C_p \cdot p_0 & 1 & 0 \\ -\frac{K_\psi^{\mathrm{att}} + K_p^{\mathrm{att}} \cdot K_p^{\mathrm{head}}}{T_e} & -\frac{K_p^{\mathrm{att}}}{T_e} & -\frac{1 + K_{\dot{p}}^{\mathrm{att}}}{T_e} & -\frac{K_p^{\mathrm{att}} \cdot K_p^{\mathrm{head}}}{T_e} \\ 0 & 0 & 0 & 0 \end{pmatrix} \vec{x} + \begin{pmatrix} 0 \\ 0 \\ 0 \\ K_\theta^{\mathrm{head}} \end{pmatrix} \vec{u} \qquad \text{(N)}$$

The constants with uncertainties below 10 % are given in Tab. E.

Parameter	ρ	m	S	b	I_x	I_y
Value	$1.225\,{}^{\mathrm{kg}}/_{\mathrm{m}^3}$	$14.5\,\mathrm{kg}$	$1.7\,\mathrm{m}^2$	$4.4\,\mathrm{m}$	$0.74\,\mathrm{kg}\cdot\mathrm{m}^2$	$21.5\,\mathrm{kg}\cdot\mathrm{m}^2$

Table E.: Parameters of the uncertainy analysis.

Eigenvalues and Eigenvector of the Closed-Loop System

The eigenvalues λ and eigenvectors $\vec{v}$ are calculated by solving for $A \cdot \vec{v} = \vec{v} \cdot \lambda$. The corresponding flight states of each line of the eigenvectors are added for a better understanding.

$$\vec{v} = \begin{pmatrix} 0 & 0 & 0 & 0 & 0 & 0 & -0.34 & 0.85 & 0.88 \\ 0 & 0 & 0 & 0 & 0 & 0 & -0.64 & 0.38 & 0.23 \\ 0 & 0 & 0.02 & 0.02 & 0.01 & 0.01 & -0.14 & 0.03 & -0.01 \\ 0 & 0 & -0.07-0.02i & -0.07+0.02i & -0.02+0.06i & -0.02-0.06i & 0.26 & -0.01 & 0 \\ 1 & 0.04 & 0.85 & 0.85 & -0.02-0.68i & -0.02+0.68i & 0.02 & -0.3 & 0.41 \\ 0 & 0 & 0 & 0 & -0.01-0.01i & -0.01+0.01i & 0.11 & -0.06 & 0.03 \\ 0 & 0 & -0.08 & -0.08 & 0.11+0.05i & 0.11-0.05i & -0.2 & 0.03 & 0 \\ 0 & 1 & 0.42-0.29 & 0.42+0.29 & -0.72 & -0.72 & -0.54 & 0.12 & 0 \\ 0 & 0 & 0 & 0 & 0 & 0 & 0.22 & -0.19 & 0.09 \end{pmatrix} \begin{matrix} \int u \\ u \\ \theta \\ q \\ \dot{q} \\ \psi \\ p \\ \dot{p} \\ \psi^{\mathrm{cmd}} \end{matrix} \tag{O}$$

$$\lambda = \begin{pmatrix} -99 & 0 & 0 & 0 & 0 & 0 & 0 & 0 & 0 \\ 0 & -99.3 & 0 & 0 & 0 & 0 & 0 & 0 & 0 \\ 0 & 0 & -9.88+3.75i & 0 & 0 & 0 & 0 & 0 & 0 \\ 0 & 0 & 0 & -9.88-3.75i & 0 & 0 & 0 & 0 & 0 \\ 0 & 0 & 0 & 0 & -10.06+2.65i & 0 & 0 & 0 & 0 \\ 0 & 0 & 0 & 0 & 0 & -10.06-2.65i & 0 & 0 & 0 \\ 0 & 0 & 0 & 0 & 0 & 0 & -1.86 & 0 & 0 \\ 0 & 0 & 0 & 0 & 0 & 0 & 0 & -0.44 & 0 \\ 0 & 0 & 0 & 0 & 0 & 0 & 0 & 0 & -0.268 \end{pmatrix} \tag{P}$$

The frequency f_0 and damping constant d are given in Tab. F

λ, $^{\mathrm{rad}}/_{\mathrm{s}}$	-99	-99.3	$-9.81 \pm 3.75i$	$-10.06 \pm 2.65i$	-1.86	-0.44	-0.268
λ, Hz	-16	-16	$-1.56 \pm 0.6i$	$-1.6 \pm 0.42i$	-0.3	-0.07	-0.04
f_0, Hz	16	16	1.67	1.65	0.3	0.07	0.04
d, Hz	1	1	0.93	0.97	1	1	1

Table F.: Eigenvalues, frequency and damping of the poles.